Aus dem Institut für Neuropathologie
der Medizinischen Fakultät Charité – Universitätsmedizin Berlin

DISSERTATION

Characterization and manipulation of myeloid cells in the healthy and diseased Central Nervous System

zur Erlangung des akademischen Grades
Doctor of Philosophy (PhD)

vorgelegt der Medizinischen Fakultät
Charité – Universitätsmedizin Berlin

von

Natalia Drost
aus Tarnowskie Gory, Polen

Datum der Promotion: 05.06.2016

Table of contents

1 Abstract

Microglia are yolk sac-derived resident immune cells of the brain. They are important for brain development and tissue homeostasis, as well as for the response to tissue injury and diseases. Activation of microglia around amyloid-beta (Aβ) deposits is a major hallmark of Alzheimer's disease (AD), but microglia are believed to be ineffective in clearing these deposits to combat disease. While the microglial population is maintained by local self-renewal, newly recruited myeloid cells are believed to be more effective in reducing Aβ burden. To study the functional differences between endogenous microglia and newly recruited myeloid cells, we followed up on the observation that conditional ablation of microglia in the CD11b-HSVTK (TK) mouse model provokes a massive influx of peripherally-derived myeloid cells to the central nervous system (CNS). To determine whether these newly recruited cells are able to phenotypically and functionally replace microglia *in vivo*, we first characterized the exchange of these cells intravitally by two-photon microscopy. Morphologically, newly recruited myeloid cells have shorter, less branched cytoplasmic processes and smaller cell-to-cell distances compared to endogenous microglia. Furthermore, these cells show faster cell body movement and are more reactive towards a laser-induced tissue lesion than resident microglia, indicating enhanced functional capabilities.

To test if these newly recruited cells are more effective in the disease context than microglia, we crossed APPPS1 mice, resembling features of AD, to TK mice and studied the impact of the exchange of resident microglia with peripheral myeloid cells on AD-like pathology. Surprisingly, almost complete exchange of microglia with peripheral myeloid cells had no impact on overall Aβ-pathology. While soma and process morphology of newly recruited cells remained unaffected in the presence of Aβ-pathology, process movements were slower in vicinity of Aβ-plaques. Furthermore these cells did not cluster around Aβ-plaques, suggesting that an additional stimulus may be required to induce reduction of amyloid deposits.

Finally, as an alternative approach to stimulate the innate immune system in AD, we aimed at modulating the phenotype of microglia towards increased Aβ-clearing capabilities in a mouse model of AD, by inhibiting the NALP3 inflammasome with the inhibitory drug Ebselen. While intraperitoneal Ebselen treatment was able to drastically improve amyloid pathology, toxic side-effects of the drug make research into alternative

application routes and drug formulations necessary to make it a viable treatment option for AD patients.

Altogether, even if modulation of microglia and their inflammatory responses in AD remains a valuable target, effective therapeutic strategies require further research to dissect the exact roles of the immune system in neuroinflammatory diseases.

2 Zusammenfassung

Mikroglia, die aus dem Dottersack stammenden residenten Immunzellen im Gehirn, spielen eine wichtige Rolle in der Gehirnentwicklung, Gewebs-Homöostase, sowie in der Immunantwort des Zentralen Nervensystems (ZNS) nach Gewebsschädigung und Infektionen. Amyloid-beta (Aβ) Ablagerungen, ein wesentliches Charakteristikum der Alzheimer Erkrankung (AE), sind umgeben von aktivierten Mikrogliazellen, welche jedoch nicht fähig zu sein scheinen, Aβ effektiv zu reduzieren und somit die Krankheit einzudämmen. Während die residente Mikroglia-Population des Gehirns sich vorrangig selbst erneuert, sind, gemäß der Fachliteratur, neu rekrutierte myeloide Zellen aus der Peripherie scheinbar effektiver in der Reduzierung der amyloiden Last des Gehirns. Um die funktionalen Unterschiede von endogenen Mikroglia und neu rekrutierter myeloider Zellen zu studieren, verwendeten wir das CD11b-HSVTK (TK) Mausmodell, in welchem die konditionelle Depletion von Mikroglia ein massives Einströmen von peripheren myeloiden Zellen ins ZNS auslöst. Um zu untersuchen, ob die einströmenden Zellen residente Mikroglia *in vivo* phänotypisch und funktional ersetzen können, charakterisierten wir den Zellaustausch intravital mittels Zwei-Photonen Mikroskopie.

Die aus der Peripherie stammenden myeloiden Zellen unterscheiden sich von residenten Mikroglia durch kürzere, weniger verzweigte Zellfortsätze und reduzierte Zellabstände. Zudem zeigten die myeloiden Zellen eine schnellere Zellkörper Bewegung, sowie eine schnellere Reaktion auf eine Laser-induzierte Gewebsläsion, was auf eine gesteigerte Aktivität dieser Zellen schließen lässt.

Um zu testen, ob die rekrutierten Zellen auch im Krankheitskontext effektiver sind als Mikroglia, kreuzten wir APPPS1 Mäuse – ein bekanntes AE Mausmodell - mit TK Mäusen und studierten den Effekt des Zellaustausches von residenten Mikroglia gegen periphere myeloide Zellen hinsichtlich der Effekte auf die Pathologie. Überraschenderweise hatte der fast vollständige Austausch von Mikrogliazellen keinen

Einfluss auf die Aβ Pathologie. Während die Zellkörper- und Zellfortsatz-Morphologie der infiltrierenden myeloiden Zellen nicht durch Aβ beeinflusst wurden, war die Aktivität dieser Zellen, gemessen an der reduzierten Zellkörper- sowie Zellfortsatz-Bewegung, in der Umgebung von Aβ Plaques herabgesetzt. Zudem besiedelten die myeloiden Zellen nicht die Aβ Plaques, was darauf hindeutet, dass, als Grundvoraussetzung für die Reduktion von Aβ, ein zusätzlicher Stimulus benötigt wird um diese Zellen zu den Plaques zu rekrutieren.

Als alternativen Ansatz zur Stimulierung des angeborenen Immunsystems in der AE, beabsichtigten wir den Phänotyp von Mikrogliazellen durch die Hemmung des NALP3 Inflammasoms durch den NALP3-Inhibitor Ebselen zu beeinflussen, letztlich mit dem Ziel, die Kapazität der Mikroglia Aβ zu beseitigen, zu erhöhen. Während die intraperitoneale Ebselen Applikation zu einer deutlichen Verbesserung der Amyloid-Pathologie führte, sind weitere Studien zu alternativen Applikationsrouten und Wirkstoffformulierungen aufgrund der toxische Nebenwirkungen des Pharmakons vonnöten, um Ebselen in der Klinik anwenden zu können.

Zusammenfassend ist die Modulierung von Mikroglia bzw. der inflammatorischen Prozesse in der AE ein wertvolles und sinnhaftes Angriffsziel. Für effektive therapeutische Strategien sind jedoch weitere Studien vonnöten um die exakte Rolle des Immunsystems in der AE zu verifizieren, bzw. zu validieren.

3 Introduction

3.1 Microglia

3.1.1 Physiology and function of microglia

Microglia constitute the resident immune cells in the brain and spinal cord [1]. They make up 5% to 20% of the glial cell population in mammalian brains with heterogeneity in their density among different central nervous system (CNS) regions [2]. Assembled as a tight network of cells with highly ramified processes that cover most of the parenchyma, microglia appear to monitor the brain for damage and infection [3, 4]. These highly adaptive cells are currently not only considered as inflammatory cells reacting to CNS injury, but also as critical for normal brain function. Recent studies using *in vivo* two-photon microscopy indicate that resting microglia in the healthy brain are not dormant and non-motile as thought before, but can rather be characterized as dynamic cells which continually extend, retract and remodel their processes [4, 5]. In this line of research, it was shown that microglia monitor and control the activity of neurons, as they contact synapses as well as extra synaptic regions, and are able to actively respond and influence neuronal activity [6, 7]. Furthermore microglia seem to be important in shaping the neuronal brain network in development: These cells control neuronal precursors and neuronal numbers as active killers through various molecular mechanisms and are not only waste collectors for apoptotic cells [8-12]. As microglial density in development coincides with the peak of synaptogenesis [13], there is increasing evidence that the activity of these cells drives synaptic pruning, elimination as well as the maturation of synapses. In adulthood, microglia seem to maintain some of these features and are thus critical regulators of synaptic plasticity, adult neurogenesis as well as learning and memory (reviewed in [14]).

In the damaged CNS microglia constitute the main line of immune defense by rapid migration to the affected location, where activation and morphological transformation take place. Microglial activation is accompanied by increased secretion of chemokines, cytokines and numerous cell surface markers that serve to propagate the immune response [15]. To date, distinction of activated microglia from their resting counterparts by means of a defined, unique marker is lacking. Combined morphological, immunophenotypical and molecular characterization is the primary method used for their identification and classification [16].

Thus, microglia are today considered as the mobile effector cells of the brain's intrinsic immune system as first line of defense against invading pathogens or tissue injury [15] with important functions in shaping the neuronal circuit of the healthy CNS.

3.1.2 Origin of microglia

CNS-resident microglia share pivotal characteristics with tissue macrophages. Unequivocally, they are of myeloid nature, being dependent on the transcription factor PU.1 in development [17, 18] and express the macrophagic markers CD11b and F4/80 in the murine brain [19]. However, unlike macrophages, they are not derived from hematopoietic stem cells in a Myb and CSF1 (colony-stimulating factor 1) dependently fashion from the fetal liver and later bone marrow (BM), but are independent from these transcription factors and originate in the yolk sac at E8.5-E9.0 [20, 21]. Thereafter, they colonize the developing brain in a bloodstream-dependent fashion and establish lineage-specific gene expression [20]. Until now, the discrimination of microglia from peripheral monocytes is not straight forward. Iba1 and the fractalkine receptor (CX_3CR1) are most commonly used to identify microglia in the brain, but these markers are likewise expressed by myeloid cells in the periphery.

Microglia are a long-lived cell population maintained by self-renewal [22-24] and are prone to age-related morphological changes [25], senescence and dysfunction [26]. Interestingly, there have been reports that under inflammatory conditions peripherally-derived myeloid cells can enter the brain in the diseased CNS [24, 27]. This infiltration or even recruitment seems to happen in a CCR2/CCL2 chemokine signalling dependent fashion [28, 29]. One of these inflammatory conditions where CNS infiltration and even disease contribution of peripherally-derived myeloid cells was reported is Alzheimer's disease [30].

3.2 Alzheimer's disease

The most common deterioration of memory accounting for 80% of dementia cases, with more than 35 million people affected worldwide, is Alzheimer's disease (AD). This form of dementia causes death within three to nine years after diagnosis and the principal risk factor is age. It is expected that in 2050 one new AD case will be diagnosed every 33 seconds, creating tremendous impact upon health care systems [31]. Termed a sporadic disease of the elderly which is connected to many molecular lesions, it was first presented in 1906 by Alois Alzheimer in Tuebingen and named after him by Emil

Kraepelin subsequently [32, 33]. Until now, no curative therapy is available for this detrimental disease.

3.2.1 Pathophysiology and clinical symptoms

Alzheimer's disease is mostly connected to reduced synaptic contacts [35, 36] as well as extracellular amyloid-beta (Aβ) plaques and intracellular tau aggregates (tangles), where these normally soluble proteins assemble [34]. Tau protein is an abundant soluble protein in axons, where it promotes assembly and stability of microtubules and vesicle transport. Upon hyper-phosphorylation by different enzymes, tau becomes insoluble and self-associates into paired helical filament structures. These aggregates thereby destabilize microtubules and hamper axonal transport, leading to the compromise of synapse and neuronal function (reviewed in [34, 37]). Nevertheless, the accumulation of neurofibrillary tangles (NFTs) is thought to be a secondary event to Aβ cytotoxicity.

The Aβ protein is a secreted product present in the brain and cerebrospinal fluid (CSF) of healthy humans throughout life, suggesting a physiological function, which has not been entirely elucidated yet [38-40]. Aβ is generated by the processing of the amyloid precursor protein (APP), a transmembrane protein of unknown function with a single membrane spanning domain [41, 42], as part of the amyloidogenic pathway, depicted and described in more detail in Figure 1.

The major species of Aβ are 40 and 42 amino acids long with $A\beta_{42}$ having two additional hydrophobic amino acids resulting in a more aggregation-prone protein form [43, 44]. The increase in levels of this amyloid species forms the foundation of the amyloid cascade hypothesis, which has been the central hypothesis describing the development of AD [45, 46]. Physiological concentrations of $A\beta_{40}$ are tenfold higher than those of $A\beta_{42}$ and account for the majority of secreted Aβ [47]. The amyloid cascade hypothesis states that a shift of this ratio towards $A\beta_{42}$ triggers of misfolding and accumulation of different Aβ species, resulting in plaque formation [45]. It is known that Aβ can spontaneously self-aggregate into multiple coexisting forms, oligomers of two up to six peptides being the most common, which coalesce into intermediate assemblies [48]. These protein clusters can also grow into insoluble fibrils arranging into β-pleated sheets [49, 50]. Currently, it is thought that soluble oligomers and intermediate amyloids

are the most neurotoxic forms of Aβ, rather than the insoluble extracellular amyloid plaques (reviewed in [51]).

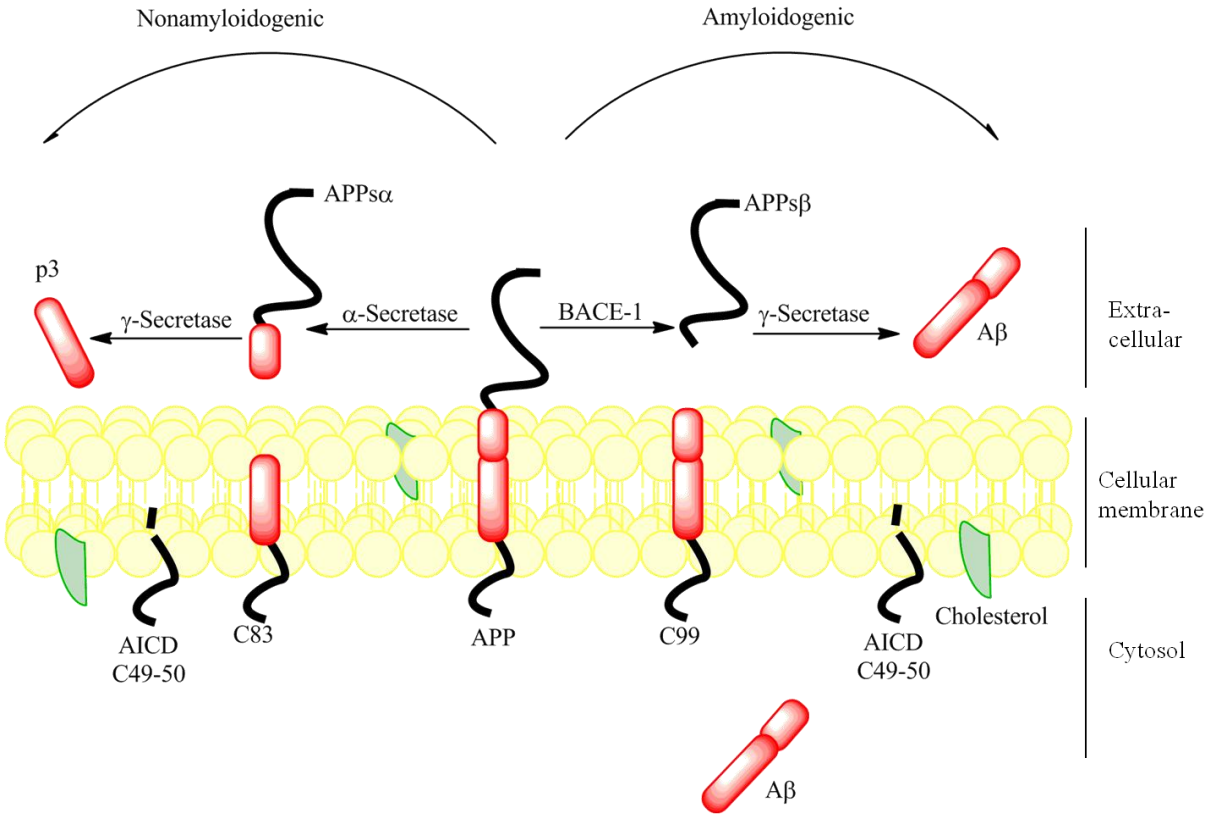

Figure 1: Processing of amyloid precursor protein. In the amyloidogenic pathway the membrane anchored APP protein is cleaved by the aspartic protease β-secretase identified as BACE1 (β-Site APP cleaving enzyme) which is abundantly expressed in the brain. This leads to shedding of the large ectodomain APPsβ into the luminal and extracellular fluid [52, 53]. The membrane bound C-terminal stub of 99 amino acid residues (C99; $APP_{\beta CTF}$) is subsequently processed by γ-secretase with its catalytic core presenilin resulting in the intracellular fragment AICD and Aβ to be released intra- or extracellularly [54]. This aspartic-protease can cleave at different positions producing extracellular Aβ forms of 38 to 43 residues in size with $Aβ_{40}$ being the most abundant form (reviewed in [55]). The non-amyloidogenic processing pathway does not generate Aβ as APP is cut within the Aβ sequence by α-secretase belonging to the ADAM (a disintegrin and metalloproteinase) family, generating the extracellular secreted APPsα fragment and the C83 C-terminal ($APP_{\alpha CTF}$). C83 is subsequently cleaved by γ-secretase in AICD and the p3 residue (Figure modified from [31]).

Plaque aggregation seems to be the origin of neurofibrillary tangle formation as well as the disruption of synaptic connections. Over the long term, amyloid plaques are connected to a multitude of inflammatory and molecular mechanisms, like oxidative stress and chronic neuroinflammation, leading to neuronal cell loss and cognitive impairment (Figure 2).

Importantly, pathological changes can occur 20 or more years before the manifestation of the first clinical symptoms. The most common initial symptom is the gradual worsening of the ability to remember new information, termed mild cognitive impairment

(MCI). MCI precedes other symptoms, as synapses and neurons of the hippocampal formation, important for learning and memory, are particularly vulnerable to early AD-related stressors [56]. This degeneration correlates with the duration and severity of the disease, involving early atrophy of the entorhinal cortex, followed by mesial temporal atrophy and global atrophy at late stages of the disease. Clinically, this is connected to the decline of cognitive and functional abilities of patients, causing inability to perform activities of daily living in advanced stages of the disease. Finally, patients lose their ability to communicate, are bedbound, and rely on around-the-clock care. [57]

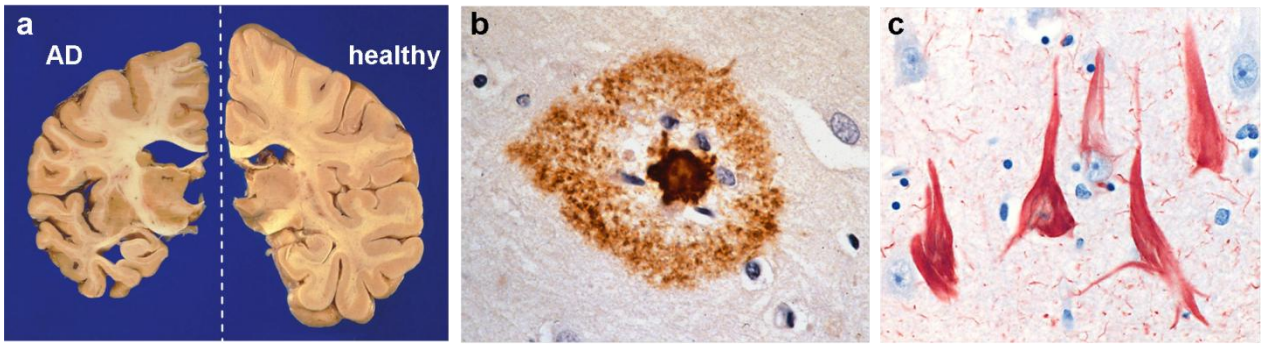

Figure 2: Neuropathological alterations in the human Alzheimer diseased brain. (a) Cross sections of an AD brain showing atrophy of the hippocampus and cortex at late stages of the disease (left) in comparison to a healthy brain (right). Pathological hallmarks of AD are the deposition of Aβ in senile plaques (b) and hyperphosphorylated tau protein in neurofibrillary tangles (NFTs, c). Source: Courtesy of Department of Neuropathology, Charité – Universitätsmedizin Berlin.

3.2.2 Late and early onset of Alzheimer's disease and risk factors

The most prevalent form of the disease with an age of onset of 65 years or older affects 99% of cases and is caused by a multitude of factors. Aβ plaques as well as NFTs are connected to many environmental [58] and genetic risk factors [59] as well as age (reviewed in [60]) which modulate different molecular mechanisms leading to late-onset AD. This complex network is still not understood in detail, resulting in the fact that still no effective treatment for Alzheimer's disease exists.

Less than 1% of cases develop the disease under 65 years of age. These patients are affected by the more severe early-onset familial AD, which is caused by autosomal dominant genetic mutations [61] in genes encoding either the secretase processing sites of human APP on chromosome 21 (reviewed in [62]), or the catalytic cores of γ-secretase, i.e. presenilin 1 [63] or presenilin 2 [64].

3.2.3 Mouse models of Alzheimer's disease

The genetic mutations identified in familial AD cases are used to mimic the disease in animal models. Most commonly, human APP with different sets of mutations is introduced into the mouse genome. The resulting transgenic animals develop amyloid plaques and memory loss and show signs of hyper-phosphorylated tau. Unfortunately, they cannot replicate all aspects of the full blown disease, as they do not develop NFTs and seldom show neuronal loss [65]. However, there are transgenic mice harboring additional mutations in tau, resulting in NFTs next to amyloid plaques [66]. Nevertheless, APP transgenic animals are very useful tools to study the underlying biological processes of amyloid deposition and resulting neurodegeneration *in vivo*.

3.2.4 Diagnosis and therapy of Alzheimer's disease

The diagnosis of Alzheimer's disease is still not straight forward today. Even though the current diagnostic criteria can identify the majority of disease cases, an unequivocal diagnosis is only possible *postmortem* through neuropathological autopsy. Commonly, following diagnostic criteria of the Alzheimer's Association and the National Institute of Neurological Disorders and Stroke from 1984 [67], the first care physician is evaluating a suspicion for AD after revising medical and family history to screen for risk factors. To assess the mental status, cognitive tests as well as physical and neurological examinations are performed. These include testing the level of alertness, attention, orientation, short-term and remote memory, language, visuospatial functioning, calculation, and executive functioning or judgment [68]. Neuropsychometric tests often include the CERAD neuropsychological test battery, the Mini-Mental State Exam [69] and the Clock Drawing test [70]. In order to exclude reasons and diseases other than classical neurodegenerative disorders responsible for the clinical diagnosis of dementia, computed tomography or magnetic resonance imaging is performed [57]. In 2011 revised criteria and guidelines for diagnosing AD were published, updating the guidelines from 1984 [71] so that currently the diagnosis of AD distinguishes two stages of the disease (MCI and dementia) and incorporates biomarkers (summarized in Figure 3).

Thus far no treatment for AD is available that slows or stops neurodegeneration or upstream initiators of the disease. All therapeutics available enhance the availability of neurotransmitters in the brain to temporarily improve the disease symptoms. Only five

drugs exclusively tackling the symptoms of AD are currently approved by the US Food and Drug Administration, to which at least half of the patients do not respond. This sows the tremendous need for further research to efficiently prevent or halt the disease [57]. Currently, active investigation is mainly conducted into immunologic and amyloid-based therapy approaches, Aβ vaccination being the most promising one (reviewed in [72]).

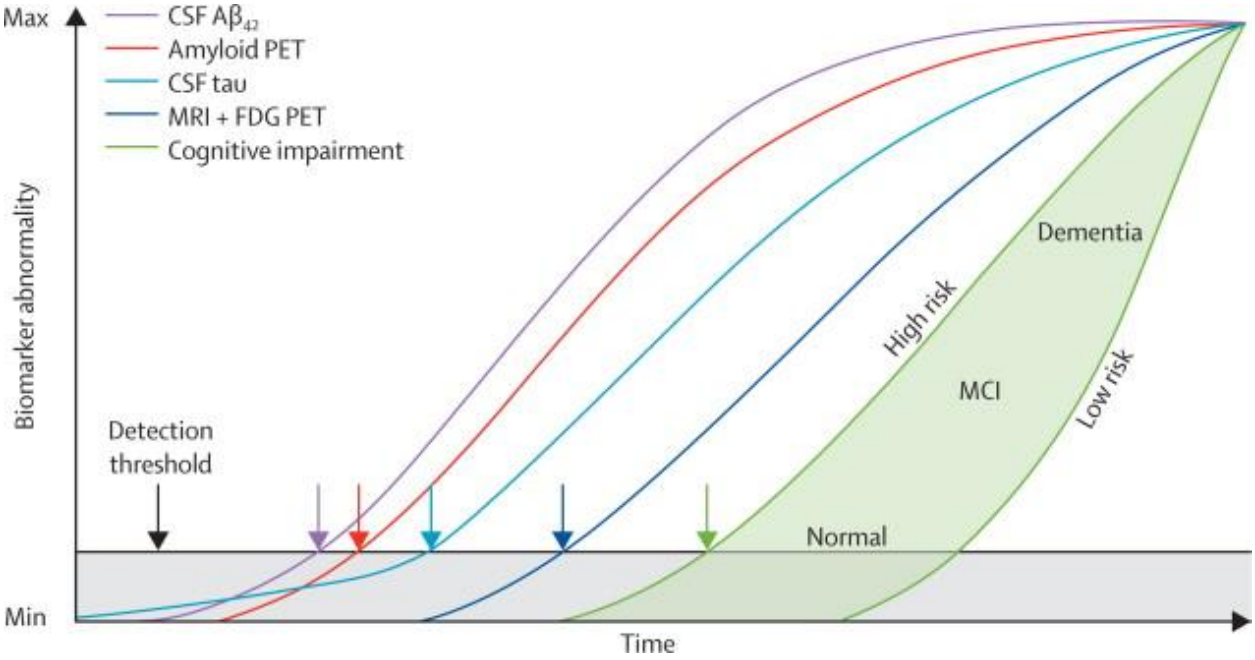

Figure 3: Biomarkers for diagnosis of Alzheimer's disease. "The threshold for biomarker detection of pathophysiological changes is denoted by the black horizontal line. The grey area denotes the zone in which abnormal pathophysiological changes lie below the biomarker detection threshold. In this figure, tau pathology precedes Aβ deposition in time, but only early on at a sub threshold biomarker detection level. Aβ deposition then occurs independently and rises above the biomarker detection threshold (purple and red arrows). This induces acceleration of tauopathy and CSF tau then rises above the detection threshold (light blue arrow). Later still, FDG PET and MRI (dark blue arrow) rise above the detection threshold. Finally, cognitive impairment becomes evident (green arrow), with a range of cognitive responses that depend on the individual's risk profile (light green-filled area). Aβ = amyloid β, FDG = fluorodeoxyglucose, MCI = mild cognitive impairment"; figure and text from [73].

3.3 Microglia in Alzheimer's disease

Inflammation is a central part of the pathophysiology of AD. Neuroinflammation accompanying senile plaques and NFT's is not only a consequence of these protein deposits, but actively contributes to AD pathology [74]. Recently, genes encoding for the immune receptors TREM2 and CD33 were identified as genetic risk factors for late onset AD. Both play a role in phagocytosis: TREM2 mediates phagocytic clearance of neuronal debris and is highly expressed by microglia [75-78] whilst a mutation in the microglial surface receptor CD33 was connected to reduced Aβ phagocytosis *ex vivo*

[79, 80]. Microglia interact closely with Aβ fibrils through their processes [81-83], cluster around Aβ deposits and get primed for activation ([84], Figure 4A). Microglia were shown to induce an inflammatory reaction in response to plaques by secreting immune molecules such as interleukin (IL)-1, IL-6, IL-12, IL-23, GMCSF, TNFα and complement proteins *in vivo* as well as many more cytokines, chemokines and growth factors *in vitro* [85-89]. Furthermore, these cells are able to bind soluble Aβ via various cell-surface receptors, as SCARA1, CD36, CD14, α6β1 integrin, CD47 and Toll-like receptors (TLR2, 4, 6, 9), resulting in phagocytosis and degradation via the endolysosomal pathway [90-93]. The major extracellular proteases of microglia able to degrade soluble Aβ are neprilysin (NEP) and insulin-degrading enzyme (IDE).

Yet of course, microglial actions do not suffice to inhibit AD pathology [94]. As a matter of fact, the chronic exposure to Aβ as well as inflammatory mediators seem to even cause a chronic, non-resolving inflammation in late stage AD, accompanied by the release of reactive oxygen and nitrogen species (ROS, NOS; [95, 96]). This oxidative stress is presumed to damage the local microenvironment and to aggravate disease pathogenesis [97]. Microglial immune actions in CNS pathology are summarized in Figure 4B.

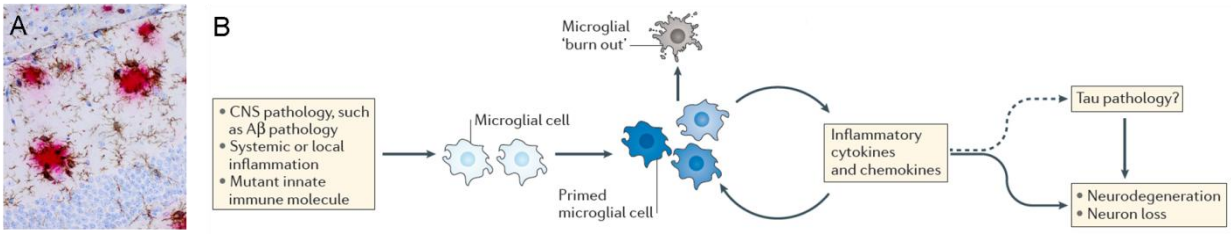

Figure 4: Microglia in Alzheimer's disease. (A) Microglia are activated and cluster around Aβ plaques [98]. (B) Schematic depiction of various steps of microglia actions in AD (text and figure from [99]): "The presence of Aβ (as well as other pathological protein deposits or alterations in the CNS, systemic or local inflammation, or mutations in genes encoding innate immune molecules) can 'prime' microglial cells, that is, make them susceptible to a secondary stimulus and/or promote their activation. Priming results in various functional microglia phenotypes (indicated by different colors), presumably accompanied with no or only minor morphological alterations and/or even no (major) cell-surface marker differences. In AD, Aβ will sustain chronic activation of primed microglia (due to the accumulation of Aβ) that results in constant production of inflammatory cytokines and chemokines by microglia, which in turn will maintain activation of these primed cells. This process results in a vicious circle, which ultimately causes an (yet reversible) impairment of microglia; moreover, it also affects surrounding CNS resident cells such as astro- and oligodendrocytes as well as neurons, possibly aggravating tau pathology (denoted by the dashed line and a question mark), and finally causing neurodegeneration and neuron loss. If these processes perpetuate over a prolonged period, it forces microglia into a senescent, 'burn-out'-like (dystrophic) phenotype, which is thought to be irreversible. "

Recent literature gives first indications as to why microglia are not able to circumvent AD pathology. First, these long-lived cells are prone to ageing [25], and aged microglia

are not as good at phagocytosing Aβ as their younger counterparts [100]. They were also shown to have a compromised responsiveness to injury as well as to a laser-induced tissue lesion in the vicinity of amyloid deposits [101, 102]. Thus, microglia seem to become dysfunctional in the vicinity of amyloid plaques and reach a state of cellular senescence [103]. Temporary ablation of these cells for 30 days in an AD transgenic mouse model showed no alterations in amyloid burden, underlining the missing contribution of these malfunctional cells in late stages of AD [104].

3.3.1 Manipulation of microglia in Alzheimer's disease

To tackle amyloid burden and thus improve AD outcome, the inefficient clearance of Aβ needs to be improved. Thus, many studies focus on the exchange of microglia with cells harboring an improved capability to phagocytose amyloid or on an experimental stimulation or modulation to reverse the impaired microglial phenotype.

3.3.1.1 Cell therapy

Several studies proved that progenitor cells transplanted into the diseased CNS were able to ameliorate pathogenesis of AD and may thus be seen as a valuable cell therapeutic tool. Progenitor cells are capable of either creating a new pool of microglia by direct differentiation, modulating the microenvironment of resident microglia or increasing their metabolic activity [105]. For example, systemic administration of human umbilical cord blood cells increased the phagocytic capacity of microglial cells and lead to a reduction in parenchymal and vascular Aβ [106]. Likewise, the transplantation of adipose- or bone marrow (BM)-derived mesenchymal stem cells was shown to slow down AD pathogenesis [107, 108].

Other previous studies showed that hematopoietic cells seem to be recruited to the AD brain and cluster around a subpopulation of amyloid deposits [30]. Thus, the main line of research is concentrating on cell based therapies involving peripherally-derived myeloid cells. For example, BM-derived monocytes were shown to be more efficacious in Aβ phagocytosis [109], especially when derived from healthy individuals and non-AD patients [110]. Furthermore, a very recent study by Hohsfield *et al.* showed that intravenous transplantation of young monocytes enhanced amyloid clearance in an AD mouse model [111]. In addition, reduction of the migratory potential of monocytes to the brain by CCR2-deficiency in transgenic AD mice resulted in accelerated/aggravated Aβ

accumulation, pointing to critical and beneficial involvement of peripherally-derived cells in AD [27, 112, 113].

3.3.1.2 Cell stimulation and immunomodulation

Changing the proinflammatory signature of chronically activated microglia into more alternatively activated cells that promote tissue repair by immunomodulation was shown to be effective for Aβ degradation. Likewise, stimulation of microglia could enhance their phagocytic ability and result in better amyloid clearance. For instance, systemic as well as intra-hippocampal administration of the TLR4 ligand lipopolysaccharide (LPS) or its derivate monophosphoryl lipid A reduced cerebral amyloid deposits by activating microglia [114, 115]. In addition, reduction of Beclin 1 expression *in vitro* and *in vivo* inhibited phagocytosis by decreasing the recycling of the immune receptors CD36 and TREM2, making it a valuable target to tackle amyloid burden upon upregulation [118]. Another successful approach has been the inhibition of the IL-12/23 signaling pathway, which resulted in ameliorated AD pathology, including improved cognitive function [87].

On the other hand, anti-inflammatory agents have also been used to modulate microglial activity. For example, application of anti-inflammatory agonists of nuclear retinoid X receptors (RXR) were shown to induce CD36 signaling, thus stimulating phagocytosis and increasing Aβ uptake [122, 123]. In addition, the treatment with the anti-inflammatory small molecule HPB242 also resulted in amelioration of AD pathology [124]. Another recent, very promising approach targeted the NALP3 inflammasome [127]. Inflammasomes are multimolecular protein complexes in myeloid cells, such as monocytes and microglia, that sense infectious agents, as well as host-derived danger signals as part of the innate immunity (Figure 5, [128]). The inflammasome subtype NALP3 was recently shown to be activated by Aβ [129]. Genetic deletion of NALP3 in an AD mouse model resulted in increased microglial phagocytosis and increased expression of IDE leading to a marked reduction in cerebral amyloid deposits as well as improved cognitive function [127]. Therapeutic targeting of NALP3 therefore is a very promising approach to decelerate AD pathology.

There are additional studies for immune targets that may manipulate AD pathology. As some of those generate conflicting results, they are not described in detail here but can be reviewed in [99].

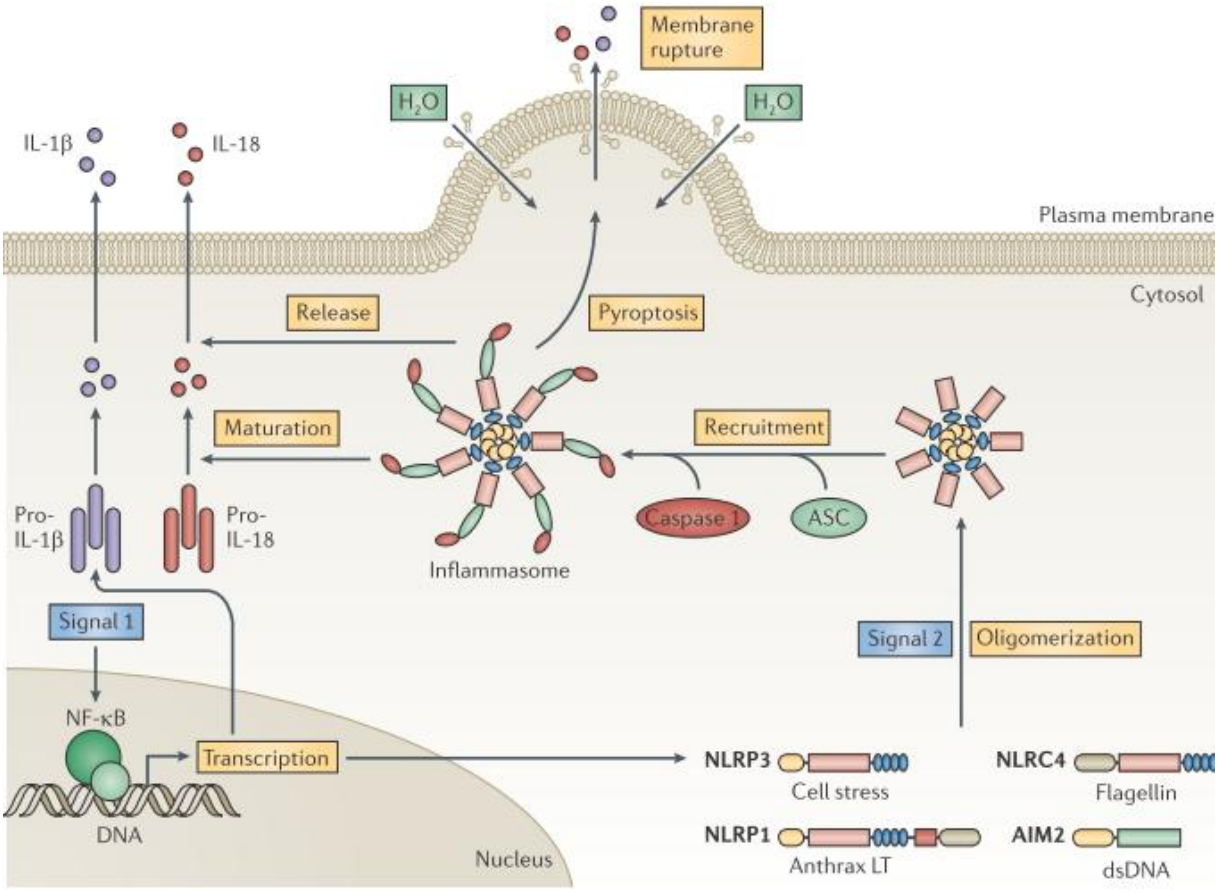

Figure 5: Inflammasomes as innate immune sensors in microglia. Multiprotein complexes, termed inflammasomes, can sense individual pathogens or host-derived insults. The NLRP3/NALP3 inflammasome is the best studied subtype so far and is activated upon sterile stimuli, such as urine crystals, Aβ or cell stress related ion fluxes. A priming stimulus (signal 1), acting through Toll-like receptors and the nuclear factor-κB (NF-κB) signaling pathway, often precedes assembly of the inflammasome complex in order to upregulate the expression of pro-IL-1β and NLRP3. Upon ligand sensing or enzymatic activation within the cytosol through a sterile stimulus (signal 2), the cytosolic sensors oligomerize and recruit the adaptor protein ASC (apoptosis-associated speck-like protein containing a CARD (Caspase activation and recruitment domain)) to form an activation platform for Caspase 1. This protease is subsequently cleaved into its active form and further regulates the maturation and release of IL-1β and IL-18, but also triggers pyroptotic cell death. dsDNA = double-stranded DNA, LT = lethal toxin; modified text and figure from [128].

3.4 Previous work

In collaboration with the group of Mathias Jucker (University of Tuebingen), the group of Frank Heppner recently established an *in vivo* system utilizing CD11b-HSVTK mice to substantially ablate microglia at any given time point, which subsequently allows us to functionally study microglial properties *in vivo* [104]. The transgenic CD11b-HSVTK model developed by Heppner *et al.* (2005) [130] harbors the thymidine kinase (TK) of the herpes-simplex virus (HSV) under the control of the myeloid cell-specific CD11b promoter and is able to transform the antiviral nucleotide analogue prodrug ganciclovir (GCV), into toxic triphosphates [130, 131]. Thus, this system allows controlled depletion of myeloid cells, such as macrophages and microglia, upon GCV administration [132]. Depletion of nearly all brain resident microglia (>90%) is achieved by intracerebroventricular (icv) administration of GCV for 10 days [104]. Interestingly, recent data from our group demonstrate a rapid repopulation of the microglia-depleted CNS with Iba1- and CD11b-positive (Iba1+; CD11b+) cells (Figure 6), as determined by immunohistochemistry. The repopulating cells (tdRFP in Figure 6) were more numerous than resident microglia (GFP in Figure 6) in non-microglia-depleted TK-negative control mice and distributed evenly throughout the brain.

Data from our group suggests that the infiltrating cells are inflammatory monocytes from the periphery, as they are highly positive for the hematopoietic marker Ly6C and CD45 which are upregulated under inflammatory conditions. These cells colonize the entire CNS and remain in the brain, where they give rise to microglia-like cells 60 days after entry into the brain. This transformation is characterized by downregulation of Ly6C and CD45 expression differential to CNS-resident microglia, that express $CD45^{int}$ CD11b+ [133].

Since recent findings propose peripherally-derived myeloid cells as good candidates to combat amyloid deposition (see introduction 3.3.1.1), the CD11b-HSVTK system can be used to test this hypothesis when crossed to an AD mouse model. Thus, by crossing CD11b-HSVTK mice to APPPS1 mice (termed APP+;TK+ or -), which mimic amyloidosis and are commonly used as mouse model for AD (see method section), our group tested the capability of peripherally-derived myeloid cells to reduce Aβ plaques. To deplete resident microglia and establish a full repopulation of the brain with peripherally-derived cells, APP+;TK+ mice were treated with GCV for ten days and analyzed for plaque burden 14 days after cessation of treatment. Here, no reduction of

amyloid burden in APP+;TK+ mice could be seen compared to treated APP+;TK- controls.

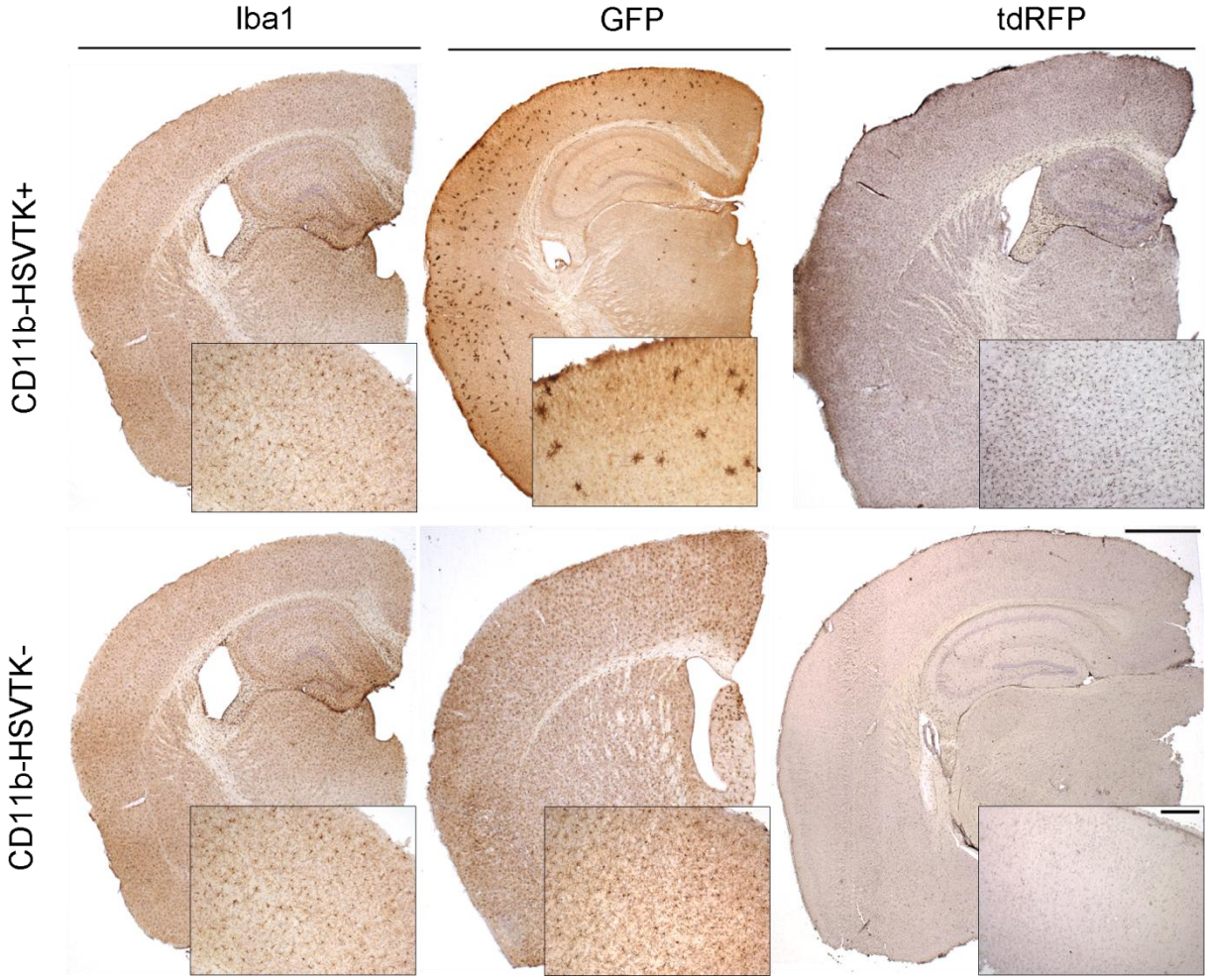

Figure 6: Histological staining of endogenous microglia and repopulating peripherally-derived myeloid cells. The pictures shown are acquired from 178 day old CD11b-HSVTK mice crossed to mice harboring one allele of the green-fluorescent protein (GFP) knocked into the fractalkine receptor locus, that underwent irradiation and reconstitution with bone marrow from red fluorescent reporter mice (tdRFP; see method section). Thus, in these mice, endogenous microglia are GFP-labeled, while peripheral immune cells are positive for tdRFP. Immunhistological staining for Iba1, GFP and tdRFP was performed after 10 days of GCV treatment, to deplete endogenous microglia, and cessation of treatment for 14 days to allow for repopulation to occur. In CD11b-HSVTK+ animals, endogenous GFP+ microglia are depleted substantially and show a morphology indicating activation. In these animals the brain is fully repopulated by tdRFP peripherally-derived cells, accounting for the majority of Iba1+ cells. On the other hand, nearly no tdRFP peripherally-derived cells are detectable in CD11b-HSVTK- animals. Scale bar: 1mm, inlay 100µm; own data.

However, treatment of these mice with GCV for a prolonged time-span of 38 days followed directly by amyloid burden analysis after cessation of treatment at a mouse age of 200 days showed a slight reduction in Aβ, assessed by immunohistochemistry using 4G8 antibodies (Figure 7). Thus, the experimental setup of prolonged GCV

treatment seems to prime peripherally-derived myeloid cells to efficiently tackle AD pathogenesis.

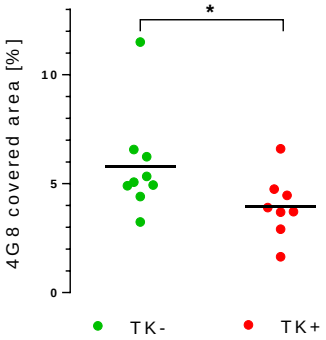

Figure 7: Peripherally-derived myeloid cells recruited to the brain are able to reduce amyloid burden. APP+;TK+ or – (TK+ or TK-) mice were treated for 38 days with GCV and sacrificed for Aβ analysis after cessation of treatment at the age of 200 days. Only mice where the brain was repopulated by peripherally-derived myeloid cells after microglial depletion (red) showed a slightly reduced plaque burden in comparison to mice with endogenous brain microglia (green). Source: Courtesy S Prokop and K Miller from the Department of Neuropathology, Charité – Universitätsmedizin Berlin.

3.5 Aim of the study

Microglia, the resident immune cells of the brain, constantly scan the brain for pathogens and have important functions in brain development and tissue homeostasis. These cells are derived from the yolk sac very early in development and have a long life span. The microglial pool is maintained mainly by self-renewal, the recruitment of myeloid cells from the periphery to the CNS being a rare event, mainly occurring in special situations, like disease.

As described in our previous work (chapter 3.4), the CD11b-HSVTK system creates a niche in the brain and attracts peripherally-derived myeloid cells after microglial depletion [5]. Histological stainings point to the fact that these peripherally-derived cells can mimic microglial morphology in the brain. However, it is still unclear whether these invading cells are able to replace microglia phenotypically and functionally *in vivo,* which comprises the first part of this thesis.

The second part of the thesis focuses on the role of microglia in the AD context. Microglia are able to phagocytose and clear Aβ, a main pathological hallmark of the disease, *in vitro* [91, 134, 135]. On the other hand, *in vivo* studies point towards a disability of these cells to tackle Alzheimer's pathology [104]. To attempt to reduce amyloid burden and thus improve AD outcome, this thesis followed two approaches: First, to exchange malfunctional endogenous microglia with myeloid cells from the periphery, using the CD11b-HSVTK mouse model. Second, to manipulate endogenous microglia aimed at modulating its amyloid clearing capacities.

3.5.1 Project Aim 1: *In vivo* characterization of myeloid cell dynamics in the healthy brain

Under normal biological conditions the invasion of peripheral monocytes into the CNS is a very rare event. The biological processes underlying the infiltration of the brain are unknown, and thus our knowledge about this cell population in the brain is limited. The first part of the thesis aims to characterize the newly entered myeloid cells in the brain and the repopulation process itself. For this, the microglial depletion process followed by repopulation was monitored *in vivo* by two-photon microscopy in the healthy CNS using a long-term imaging setup. Brain infiltrating cells were characterized and quantified for their morphological characteristics, such as soma and process parameters, and compared to brain resident microglia. Furthermore, the dynamics of soma and process movements of the various myeloid cell types were measured.

3.5.2 Characterization and manipulation of myeloid cells in Alzheimer's disease

In vivo, microglia seem unable to sufficiently tackle amyloid burden in AD. Thus, this project sought to reduce amyloid burden by replacing and/or manipulating these malfunctional cells. Recent studies suggest that peripherally-derived myeloid cells recruited to the brain are better at combating Aβ than their CNS-resident counterparts as they were shown to contain Aβ species and associate with plaques *in vivo*, hinting towards a better phagocytosing capability [109]. In addition, restricting the entry of peripheral cells to the CNS by deletion of the chemokine receptor CCR2, increased plaque load and modulated Aβ deposition [27, 112].

3.5.2.1 Project Aim 2: Replacement of resident microglia by peripherally-derived myeloid cells in Alzheimer's disease

The invasion of peripheral cells into the amyloid loaded CNS and the underlying biological processes have not been studied in detail. Most of the literature as well as our own previous work only provides a brief overview: the results of the study by Grathwohl *et al.* (2009) rely on histological snap-shots of amyloid burden in transgenic mice at two, three or four weeks post depletion of resident microglia using the CD11b-HSVTK mouse model [104]. The second aim of this study therefore aimed at pursuing the microglial depletion and repopulation process in the diseased CNS in an intravital context over longer time periods in order to study differential effects of microglia and peripherally-

derived myeloid cells. Along this line, soma and process tree parameters of Aβ-associated microglia were compared to peripherally-derived myeloid cells, to cells not touching amyloid deposits - as well as to the setting within the healthy CNS. Likewise, dynamics of these cells and plaque occupancy were analyzed. These measurements were aimed at clarifying whether peripheral myeloid cells are indeed better capable to clear Aβ.

3.5.2.2 Project Aim 3: Phenotypic modulation of endogenous microglia by NALP3 inflammasome inhibition as therapeutic strategy for Alzheimer's disease

Reversing the malfunctional phenotype of microglia in the diseased CNS presents an additional therapeutic approach to tackle amyloid burden. Recent studies (3.3.1) described a novel role of the NALP3 inflammasome in the pathogenesis of Alzheimer's disease. This sensor of innate immunity, present in monocytes and microglia, is a promising target for therapeutic manipulation. Genetic NALP3 knock-out reduced amyloid burden, which encompassed an improvement in microglial phagocytosis [127]. Nevertheless, until recently, no specific inhibitor of this multicomplex protein was known. Ebselen, a safe organoselenium compound, was recently identified as specific NALP3 inhibitor by Prof. Hornung at the University of Bonn (personal communication). Ebselen is listed as safe and approved drug by the US National Institutes of Health Clinical Collection and is known to cross the blood-brain barrier. Thus, the third aim of this thesis was to test Ebselen as a potential therapeutic to combat AD. Therefore, mice exhibiting AD-like pathology were treated for three months with intraperitoneal injections of Ebselen and subsequently, their brains were analyzed for amyloid burden and inflammasome activation at an age of 120 days.

4 Methods

4.1 In vivo *experiments*

4.1.1 Animal handling and cross-breeding procedures

As an animal model for Alzheimer's disease APPPS1+ (termed APP+) mice [136], kindly provided by Matthias Jucker (University of Tuebingen), or APPPS1- (termed APP- or wildtype, wt) littermate controls were used. This transgenic strain expresses the Swedish mutation KM670/671NL in APP, which affects the BACE1 cleaving site and shifts cleavage towards the amyloidogenic pathway. Furthermore, these mice express the L166P mutation in the presenilin1 enzyme, thus shifting the $A\beta_{40}/A\beta_{42}$ ratio towards $A\beta_{42}$ without increasing the total amount of Aβ. These mutations, known from familiar AD cases, result in robust amyloid plaque pathology in these mice, starting already at two months postnatally in the cortex. [136]

To visualize microglia for *in vivo* microscopy experiments, APPPS1 mice were crossed to CX_3CR1-GFP mice [137] (termed FracGFP), kindly provided by Helmut Kettenmann (MDC, Berlin). Here, the enhanced green fluorescent protein (GFP) was knocked into the fractalkine receptor locus. To sustain fractalkine signaling, only heterozygous mice (termed $FracGFP^{+/-}$) were used.

To ablate microglia, $FracGFP^{+/-}$;APP+ or – mice were bred to CD11b-HSVTK mice (termed TK+ or TK-; described in 3.4). For *in vivo* microscopy $FracGFP^{+/-}$;APP+ or – ;TK+ or – mice, as described in the experimental setup in the results section, were used.

For all experiments male or female mice at various ages were analyzed. Animals were housed in standard cages under pathogen-free conditions on a 12 hour (h) light/dark cycle with food and water *ad libitum*. All animal experiments were performed in accordance to the national animal protection guidelines approved by the regional offices for health and social services in Berlin (G0289/11, G0333/13; LaGeSo Berlin).

4.1.2 Polymerase chain reaction genotyping

Mouse ear biopsies were lysed in approximately 100 µl genotyping lysis buffer (10 mM Tris(hydroxymethyl)-aminomethan (Tris) hydrochlorid (Merck; pH 9), 50 mM potassium chloride, 0.5 % Nonidet P-40, 0.5 % Tween20) containing 0.1 mg/ml proteinase K (in 10 mM Tris (pH 7.5); Roche) per tail at 55°C overnight. After inactivation (5 minutes (min),

95°C) and centrifugation (10 min, 13000 rounds per min (rpm)) 2 µl of the lysate was used for genotyping. Each polymerase chain reaction (PCR) reaction was performed in a volume of 20 µl with 2 µl of the sample (1:10 dilution for FracGFP samples), 1x RED Mastermix (Invitek), 375 nM primer dNTP's (refer to Table 1 for sequences). The PCR reaction was performed in a Thermocycler PCR machine with the respective cycle conditions for each transgenic line depicted in Table 2. The PCR products were confirmed by gel electrophoresis (1.5% w/v agarose gel with 0.5 mg/ml Ethidium bromide in Tris-acetate-ethylenediaminetetraacetic acid buffer (TAE, Life technologies)), 120V for 45 min using negative and positive controls as well as HyperLadder™ 500 bp (Bioline) as size marker. DNA was visualized under ultraviolet light.

Table 1: Oligonucleotide primer for genotyping

Primer	Sequence 5'-3'
APP CT 5'	GAA TTC CGA CAT GAC TCA GG
APP CT 3'	GTT CTG CTG CTG CAT CTT GGA CA
FracGFP 5'	CCC AGA CAC TCG TTG TCC TT
FracGFP wt 3'	GTC TTC ACG TTC GGT CTG GT
FracGFP knock-in 3'	CTC CCC CTG AAC CTG AAA C
TK 5'	GAC TTC CGT GGC TTC TTG CTG C
TK 3'	GTGCTGGCATTACAGGCGTGAG

Table 2: PCR profiles for genotyping

PCR	APP			TK			FracGFP		
Initial denaturation	94°C	2 min	1 x	94°C	90 s	1 x	94°C	2 min	1 x
Denaturation	94°C	30 s	35 x	94°C	30 s	35 x	94°C	20 s	10x +1.5°C per cycle
Annealing	58°C	30 s		53°C	30 s		65°C	15 s	
Elongation	72°C	30 s		72°C	30 s		68°C	10 s	
Denaturation	-			-			94°C	15 s	28 x
Annealing							50°C	15 s	
Elongation							72°C	10 s	
Final elongation	72°C	5 min	1 x	72°C	5 min	1 x	72°C	2 min	1 x

4.1.3 Generation of bone marrow-chimeric mice

To generate bone marrow (BM) chimeras for fluorescent visualization of peripheral myeloid cells, BM from ROSA26-tandem red fluorescent protein (tdRFP) reporter mice ([138]; kind gift of Jana Glumm, Charité – Universitätsmedizin Berlin) was extracted. Briefly, femur and tibia were removed and BM was flushed out with sterile Dulbecco's modified Eagle's medium (DMEM; Invitrogen). The cell suspension was mashed

through a 70 µm filter, centrifuged (7 min, 1300 rpm), resuspended in DMEM and cells were counted. Recipient mice were exposed to 10 Grey whole-body irradiation, after which they received intravenous (i.v.) injection of 10^7 BM cells. Subsequently, animals received treatment with antibiotics (0.01% Enrofloxacin, Baytril®, Bayer Vital) for one month. Animals were subjected to further *in vivo* manipulations four weeks after BM transplantation.

4.1.4 Cranial window and pump implantation

One day prior to surgery, miniosmotic pumps (Model 2001 or 2004, Alzet®) were filled with 2.5 mg/ml GCV (Cymevene®, Roche) in artificial cerebrospinal fluid (aCSF (in mM: 125 NaCl, 2.5 KCl, 2 $CaCl_2$, 1 $MgCl_2$, 25 $NaHCO_3$, 1.25 NaH_2PO_4, 25 glucose). For surgery the mice were kept under general anesthesia (fentanyl, 0.05 mg/kg; midazolam, 5 mg/kg; medetomidine, 0.50 mg/kg). The pump was placed into a pocket formed under the skin on the back of the animal. The skin and the periost were removed to expose the skull. Depending on the experimental setup, the flexible tube connected to the miniosmotic pump was fixed on the skull with dental cement (Flowline, Hereaus Kultzer) or attached to an icv cannula (Connector w/o pedestal, Plastics One). The cannula was inserted at anterior-posterior +0.1 mm, medial-lateral +1.0 mm and dorsal-ventral -3 mm from bregma for GCV delivery into the ventricle. It was held in place by dental cement. On the left hemisphere a round cranial window (4 mm diameter, 0.13 mm thickness) was installed over an intact Dura mater as previously described [139, 140] together with a custom build titanium ring for automatic relocation of the imaging position (Figure 8B). Following surgery, mice were treated with an intraperitoneal (i.p.) injection of 4 mg/kg rimadyl (Carprofen®, Pfizer) and additionally with 200 mg paracetamol (ben-u-ron®, Bene) in the drinking water for seven days. After ten days, the pump reservoir of the 2001 model was exchanged for the 2004 model or removed through a small incision into the animal's shoulder, without disturbing the brain infusion cannula. The 2004 model was removed likewise after four weeks. After surgery, the animals were allowed to recover for five days before starting the imaging process.

4.1.5 Two-photon imaging and laser lesion quantification

One day prior to imaging, APP+ animals were i.p. injected with 10 mg/ml Methoxy X04, an amyloid staining solution to visualize Aβ plaques [141]. For two-photon imaging, a custom built head fixation apparatus that allows precise relocation of imaging positions

over weeks (see [139] and Figure 8A) was installed on the motorized xy stage of the two-photon microscope (LaVision Biotech).

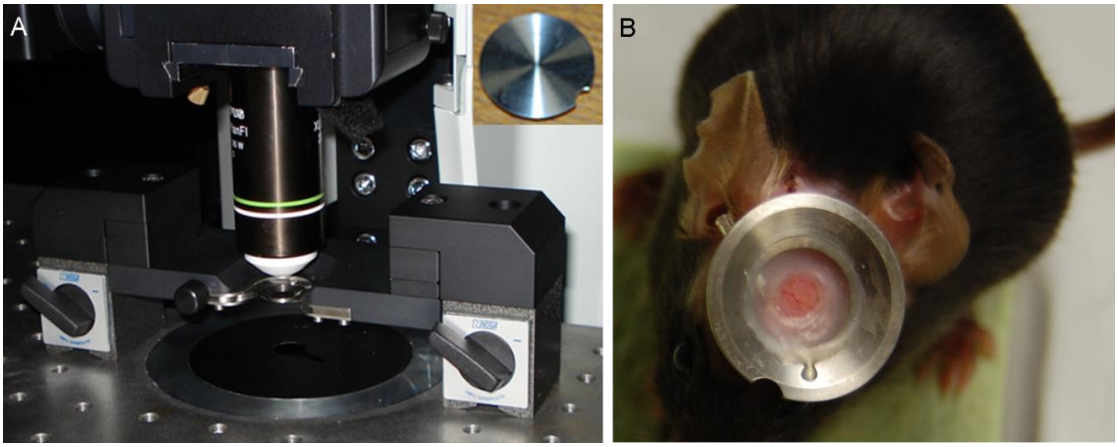

Figure 8: Technical establishment of two-photon imaging. (A) Custom built head fixation for automatic relocation of imaging positions and localization ring (top right corner) to set microscope coordinates to origin (x=0, y=0). (B) Picture of an installed cranial window together with the icv cannula and a custom made titanium ring for fixation of the animal in the head fixation apparatus.

The microscope coordinates were set to origin (x=0, y=0) at a defined fluorescently marked label on a localization ring (upper right panel in Figure 8A). Next, mice were placed on a heating pad, kept under isoflurane anaesthesia (induction at 2%, subsequently reduced and held at 0.5 - 1%) and fixed into the head fixation apparatus with a custom built titanium ring, that was installed together with the cranial window (Figure 8B). The cover slip of the cranial window was cleaned with ddH_20 and the coordinates for imaging were localized with the automated xy locator function of ImSpector Pro (LaVision Biotech) and the motorized stage. If necessary, the position was manually fine-tuned with respect to the characteristic three-dimensional plaque pattern or blood vessel landmarks. Imaging was performed using a 20X XLPLAN water-immersion objective (0.95 numerical aperture; Olympus) and multiphoton excitation of a Spectra Physics Mai-Tai laser connected to an optical parameter oscillator (HPE, tunable 710-1100 nm) to visualize GFP+ microglia and Methoxy-X04 at 850 nm and peripheral tdRFP+ cells at 1100 nm. Signals were detected via photomultipliers and following filters: 525/50 for GFP, 460/40 for Methoxy-X04 and 590/60 for tdRFP. During each imaging session three regions of interest (ROI) per mouse were imaged at 400 Hz with constant laser power and a resolution of 300x300 µm, 512x512 pixels. A z-stack of approximately 70 µm thickness was recorded, starting at a cortex depth of a minimum of 40 µm with a step size of 2 µm. All ROI were imaged once every minute for a minimum of 30 minutes.

For laser induced lesions, laser power of ~200 mW for 3 seconds (s) in a point scan mode was applied. Imaging was performed right after lesion induction as described.
After the last imaging session, mice were euthanized with dry CO_2 and transcardially perfused with ice cold phosphate buffered saline (PBS). The right brain hemisphere was snap frozen in liquid nitrogen for biochemical analysis and the left hemisphere was transferred for 48 hours (h) to 4% paraformaldehyde (PFA), followed by 24 h in 30% aqueous sucrose at 4°C for generation of free floating sections (4.2.1)

4.1.6 Analysis of two-photon microscopy data

All recorded imaging videos were registered using the “Correct 3D drift” Plugin of ImageJ to correct for translational drifts [142]. Further analyses were performed using Imaris 7.0 (Bitplane).
For evaluating the fluorescent properties of FracGFP$^{+/-}$ and Iba1-GFP+ mice, the fluorescent GFP+ signal of imaged maximum intensity projections was assessed using the integrated density measurement of ImageJ. For cell fluorescence, a round shaped ROI was set around individual cells and the measured integrated density was normalized to the cell area and signal background of the image. Fluorescent bleaching was calculated as a percentage of the integrated density of the whole image at a given time point to the integrated density of the first imaged time point.
For soma values, the surfaces of cells were detected (Figure 9A) and tracked with the surface reconstruction algorithm of the Imaris software (Figure 9B). All cell soma of one ROI were detected and tracked automatically as a batch and subsequently filtered manually for high quality somas. In detail, soma with too little fluorescence, incorrect reconstruction or tracking and cells where the soma was too close to the imaging border were excluded from further analysis. For soma size and soma sphericity, only values from the first recorded time points were used. For soma speed, cells were tracked over 30 min. For long-term soma movement somas were tracked over recorded movies for the whole duration of the experiment, i.e. seven weeks.
In order to analyze cell distances between cells and measure cell proximity to plaques, cells were detected using the spot recognition algorithm of Imaris at the first recorded time point (Figure 9C). Spots were manually controlled for to exclude double labeling of one cell and to ensure detection of every soma present in the imaging volume. Plaques were detected at the same time point using the surface reconstruction algorithm. The xyz coordinates of spots and plaques were exported and the distances between cells as

well as cells and plaques were measured for every detected cell with a customly written algorithm (kindly provided by Zoltan Cseresnyes, JIMI Berlin).

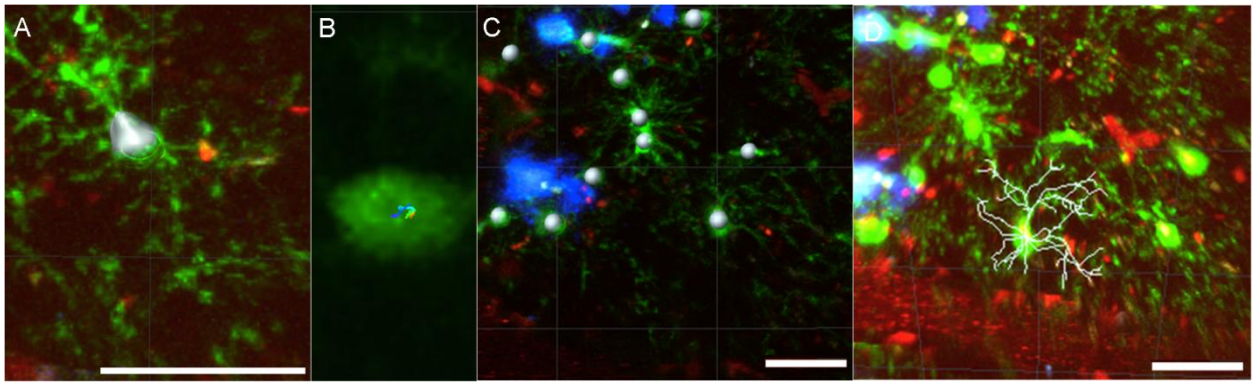

Figure 9: Bitplane Imaris 7.0 analysis of two-photon data. (A) Representative image of a reconstructed microglial cell soma. (B) Representative track of an endogenous microglial cell soma over 30 minutes. (C) Spot detection of cell somata for cell-to-cell and cell-to-plaque distance analysis. (D) Representative image of process detection of myeloid cells.

The cell processes were reconstructed using the filament detection algorithm of Imaris for each cell individually. Only cells not extending over the imaged volume were used for analysis and each cell was double checked manually after automated tracking (Figure 9D). To quantify process extension and retraction, I analyzed maximum intensity projections from the first recorded time point to those five minutes later. For each imaging time point three ROI with high quality resolution and signal were chosen. Five extensions and retractions of two up to five cells were randomly quantified with ImageJ as described before [5].

Quantification of microglial reaction after a laser lesion was performed in ImageJ using maximum intensity projections for every recorded minute of one ROI. The distance of microglial processes to the auto-fluorescent lesion was measured every two minutes.

4.1.7 Application of Ebselen *in vivo*

To test the effect of the selenium derivate Ebselen *in vivo*, the compound was dissolved in dimethylsulfoxide (DMSO, 0.5 mM) and further diluted in 25% w/v hydroxypropyl β-cyclodextrin (termed β-cyclodextrin), serving as vehicle. 30 day old APP+ or wt mice were treated with 30 mg/kg of Ebselen or vehicle by i.p. injections three times weekly (3x10 mg/kg) or alternatively the substance was dissolved in drinking water (see Figure 30A). Upon treatment mice were euthanized using dry CO_2, transcardially perfused with ice cold PBS, blood was collected (4.1.8) and the brain devoid of the cerebellum and olfactory bulb was divided into three parts (see Figure 30A). The left hemisphere was transferred into ice cold hanks buffered saline solution (HBSS) for CD11b+ cell

extraction and gene expression analysis (4.3, 4.5.2), the upper right hemisphere was snap frozen in liquid nitrogen for biochemical analysis (4.4) and for generation of free floating sections the lower right hemisphere was transferred into 4% paraformaldehyde (PFA) for 48 h, followed by 24 h in 30% aqueous sucrose at 4°C (4.2.1).

4.1.8 Screening of blood, liver and kidney in Ebselen treated animals

For blood sampling from alive animals during an experiment, 300 µl of blood were collected from the facial vein using a lancet. For terminal blood collection, mice were euthanized with dry CO_2 and as much blood as possible was collected from the heart using a 27 gauge (G) syringe prior to transcardial perfusion. Synlab GmbH, Berlin, analyzed various blood and several serum parameters.

4.2 Staining procedures

4.2.1 Generation of free floating sections

Sections of PFA-fixed brain tissue were prepared by embedding the tissue in tissue tec (Richard-Allan Scientific™ Neg-50™ Frozen Section medium, Thermo Scientific). The tissue was frozen at -21°C, cut as serial coronal sections of 30 µm thickness using a cryostat (HM560, Microm) and stored free floatingly in cryoprotectant solution (30% ethylenglycol, 20% glycerol, 50 mM sodium phosphate buffer, pH 7.4) at 4°C in a 24 well plate.

4.2.2 Amyloid staining

4.2.2.1 Pentameric formyl thiophene acetic acid (pFTAA)

For luminescent conjugated oligothiophene pFTAA labeling of soluble pre-fibrillar Aβ as well as Aβ plaques [143], free floating sections were washed three times in PBS and subsequently incubated with 2.8 µM pFTAA solution for 30 min at room temperature (RT) on a shaker. Finally, sections were rinsed again three times with PBS and mounted on a glass slide with aqueous mounting agent (Microscopy Aquatex, Merck, Germany).

4.2.2.2 Congo red

For labeling of fibrillar Aβ, free floating sections were washed twice in PBS and mounted on a glass slide, followed by counterstaining with matured hematoxilin. After subsequent incubation in stock solution I (0.5 M NaCl in 80% ethanol, 1% NaOH) for 20

min and stock solution II (8.6 mM Congo red in stock solution I, 1% NaOH) for 45 min, glass slides were rinsed twice in absolute ethanol. To fix the sections, they were incubated twice in xylene for one minute and covered using Roti®-Histokitt II mounting medium.

4.2.3 Immunohistochemistry

Immunohistochemical stainings were used to detect amyloid (4G8 antibody) as well as microglial cells (Iba1 antibody; Iba1+). To evaluate the amounts of endogenous microglia versus peripherally-derived myeloid cells in the brain, antibodies were used to detect the fluorescent tags GFP and tdRFP.

For 4G8, Iba1 and GFP stainings, free floating sections were washed three times with PBS, followed by blocking with 10% normal goat serum (NGS) in PBS containing 0.3% Triton-X-100 (PBS-TX) for 1 h at RT on a shaker. Next, the blocking solution was discarded and the primary antibody was added in 5% NGS in PBS-TX (Table 3) and incubated overnight at 4°C. The next day, sections were washed three times with PBS and incubated with the respective secondary antibody (Table 3) in 5% NGS in PBS-TX for 90 min at RT on a shaker. After another washing round (3x PBS), the peroxidase coupled secondary antibodies were developed with liquid diaminobenzidine (DAB; Dako, K3647) and counterstained with matured hematoxilin. Sections were mounted on a glass cover slide, dehydration was performed in an ascending alcohol series (70, 80, 96 and 100%) and the slide was bathed in xylene for 1 min twice before covering, using Roti®-Histokitt II mounting medium.

For colocalization of Iba1 cells in FracGFP$^{+/-}$ and Iba1-GFP+ mice fluorescent stainings were performed to account for innate GFP fluorescence. Therefore, a fluorescent second antibody was used as indicated in Table 3. Here, no DAB development was necessary and slices were directly mounted with aqueous mounting medium (Aquatex®, Merck) after incubation and washing of the second antibody.

For tdRFP staining, free floating sections were washed twice with PBS containing 0.3% Tween-20 (PBS-T), followed by 20 min incubation in PBS-T at 37°C. Blocking was performed for 1 h at RT on a shaker with 5% fetal bovine serum (FBS) in PBS-T. Next, the blocking solution was discarded and the primary antibody in PBS-T (Table 3) was added and incubated for 1 h at RT and overnight at 4°C. The next day, sections were washed three times with PBS-T and incubated with the respective secondary antibody (Table 3) in PBS for 30 min at RT on a shaker. After another washing round (3x PBS),

the peroxidase coupled secondary antibody was developed with liquid DAB containing 20 µl/ml Nickel solution and counterstained with matured hematoxilin. Sections were mounted on a glass cover slide, dehydration was performed in an ascending alcohol series (70, 80, 96 and 100%) and the slide was bathed in xylene for 1 min twice before covering, using Roti®-Histokitt II mounting medium.

Table 3: Antibodies for immunohistochemical staining

Primary antibody	Host	Dilution	Company	Secondary antibody	Host	Dilut-ion	Company
4G8	mouse	1:1000	Covance	**POD anti-mouse IgG**	goat	1:300	Dianova
Iba1	rabbit	1:500	Wako	**POD anti-rabbit IgG**	goat	1:300	Dianova
				Alexa-Fluor®568 anti-rabbit IgG	Don-key	1:300	Life technologies
GFP	rabbit	1:2000	Abcam	**POD anti-rabbit IgG**	goat	1:300	Dianova
tdRFP	rabbit, biotin conjugated	1:50	Rockland	**Avidin- POD**		1:50	Vector Labs

4.2.4 Stereological quantification of amyloid and immunohistochemical staining

All stereological quantifications were performed using the Stereo Investigator system (Microbrightfield) including an Olympus microscope BX53, the QImaging camera COLOR 12 BIT and a stage controller MAC 6000. For quantification of amyloid plaque counts stained by 4G8 antibody, Congo and pFTAA, as well as counts of Iba1, GFP and tdRFP labeled cells, the optical fractionator workflow was used. Here, ten systematically random sampled sections throughout the cortex were analyzed, counting individual plaques or cells (parameters described in table 4; [144]). To quantify 4G8, Congo and pFTAA amyloid covered area the same ten sampled sections were used and analyzed with the area fractionator workflow detecting stained areas of the tissue throughout the cortex (parameters described in table 4).

Table 4: Parameters for stereological quantification.

	Objective	Counting frame	scan grid size	Cavallieri grid spacing
amyloid count	10X	300 X 300	500 X 500	NA
cell count	60X	75 X 75	300 X 500	NA
amyloid area covered	10X	300 X 300	500 X 500	10 µm

4.3 Quantification of gene expression

For gene expression quantification, RNA was isolated from CD11b+ cells using peqGOLD TriFast™ reagent (peqlab) according to manufacturer's protocol. After RNA quantification and quality validation using i-control™ Tecan software, 12 µl of RNA were transcribed to cDNA using the QuantiTect® Reverse Transcription Kit (Qiagen) according to manufacturer's protocol. For quantitative-RealTime-PCR, TaqMan® Gene Expression Assays for respective genes and the TaqMan® Fast Universal PCR Master Mix (Invitrogen) were used with 0.5 µl cDNA as technical triplicates. The plate was read using ABI 7900HT Real-Time PCR System (Applied Biosystems) and data was analyzed with the delta-delta C_t method [145].

4.4 Quantification of protein expression

4.4.1 Protein extraction from brain tissue

To determine IL-1β and IL-18 protein levels in APP+ and wt mice of different ages, brains from transcardially PBS-perfused mice were extracted, weighted and homogenized in 10 µl/mg radioimmunoprecipitation assay buffer (RIPA; 50 mM Tris-HCl (pH 7.5), 150 mM NaCl, 1% Nonidet, 0.5% Natriumdesoxycholat, 0.1% sodiumdodecylsuflat (SDS)) containing protease inhibitor (Roche, 1 tablet per 10 ml). Homogenization was performed mechanically using syringes with cannulas of decreasing diameter (23, 27 and 30 G) followed by an incubation time of 30 min on ice. After centrifugation (30 min, 12000 g, 4°C) supernatants were snap frozen in liquid nitrogen.

For quantification of amyloid in brains of experimental mice, a four step extraction of snap frozen brains was performed as described previously [146]. Briefly, brains were weighted and mechanically homogenized in 10 µl/mg Tris buffered saline (TBS; 20 mM Tris, 137 mM NaCl, pH 7.6) containing protease inhibitor, as above. Homogenates were centrifuged (100000 g, 45 min), the supernatant snap frozen in liquid nitrogen and the cell pellet subsequently homogenized in TBS containing 1% Triton X-100 (TX) using a 1 ml pipette and the same volume of buffer as for the TBS fraction. After 30 min incubation on ice, the sample was centrifuged with above parameters and the supernatant snap frozen. The procedure was repeated for SDS buffer (2% SDS in ddH_2O) and formic acid (FA; 70% in ddH_2O), which were incubated at RT. Protein concentrations of each fraction were determined using the Quantipro™ BCA Protein

Assay Kit (Pierce) according to the manufacturer's protocol and the Photometer Tecan Infinite® 200M (Tecan).

4.4.2 Quantification of IL-18 protein expression

To determine IL-18 protein levels in RIPA or 4-step extracted homogenates, an enzyme-linked immunosorbent assay (Elisa; MBL Bioscience) was used, following the manufacturer's protocol. Each homogenate was measured at a volume of 100 µl (1:10 dilution for RIPA samples, 1:2 dilution for the TBS fraction of 4-step extracted brains) and technical duplicates were produced. Absorption was read at 450 nm and 570 nm (for wavelength correction) on a microplate reader (Infinite® 200M, Tecan) and analyzed using the Magellan™ Software.

4.4.3 Quantification of IL-1β and Aβ protein expression

To determine IL-1β, $A\beta_{40}$ and $A\beta_{42}$ protein levels in RIPA or 4-step extracted homogenates, an Elisa using the Mesoscale Discovery (MSD) 96-Well system was performed. For IL-1β, the SMALL-SPOT® assay was performed including technical duplicates using 50 µl of 1:2 diluted RIPA homogenate or TBS-fraction in manufacturer supplied buffer. For Aβ, the MULTI-SPOT® Human (6E10) Triplex Assay using 25 µl of sample in technical duplicates was used. For this purpose, TBS- and TX-fractions were diluted 1:2, SDS-fractions 1:10 and the FA fraction was first neutralized by 1:10 dilution in 1M Tris (pH 8.0) and subsequently diluted 1:125 in a 1% BSA solution (supplied by the manufacturer). All plates were analyzed with a MS6000 (MSD) machine.

4.4.4 Western blotting

For detection of Pro-Caspase1 and its cleaved fragment, synaptic markers PSD95, GAD65 and synaptophysin as well as Aβ degrading enzymes NEP and IDE, brain homogenates of mice treated i.p. with Ebselen were analyzed using Western Blots. For analysis of synaptic markers, TX- and SDS-fractions were used whilst TX-fractions were used for Caspase-1 detection and SDS-fractions for Aβ degrading enzymes respectively. During the blotting procedure, 30 µg protein per lane (in LDS loading buffer (Invitrogen) containing 5% mercaptoethanol, cooked 5 min at 95°C) were run on 10-20% Tricine gradient polyacrylamide gels (Novex) for approximately 90 min at 120V in running buffer (0.1 M Tris, 0.1 M Tricine, 0.1% SDS, pH 8.3).

Table 5: Antibodies for Western blotting

Primary antibody	Host	Dilution	Company	Secondary antibody	Host	Dilution	Com-pany
PSD95	mouse	1:1000	Maguk	**HRP anti-mouse IgG**	sheep	1:5000	GE health-care
GAD65	mouse	1:2000	Abcam	**HRP anti-mouse IgG**			
Synapto-physin	rabbit	1:2000	Antikörper online	**HRP anti-rabbit IgG**	donkey		
IDE	rabbit	1:1000	Cal-biochem	**HRP anti-rabbit IgG**			
6E10	rabbit	1:2000	Covance	**HRP anti-rabbit IgG**			
Caspase1	rabbit	1:250	Santa Cruz	**HRP anti-rabbit IgG**			
NEP	mouse	1:500	Abcam	**HRP anti-rabbit IgG**	sheep		
GAPDH	mouse	1:5000	Millipore	**HRP anti-mouse IgG**			

For analysis of APP processing (6E10 amyloid antibody), self-made 3-layered stacked gels were used (layer 1: 33.3% acrylamidsolution (14.7% Acrylamid + 0.9% Bis-Acrylamid in ddH_2O), 33.3% gel buffer (3 M Tris-HCl, 0.3% SDS), 33.3% glycerol (32% glycerin in ddH_2O); layer 2: 20% acrylamidsolution, 33% gel buffer, 46.9% ddH_2O; layer 3: 10% acrylamide solution, 25% gel buffer, 64.9% ddH_2O; all layers polymerized with 0.09% ammonium persulfate (APS, 1:10 diluted) and 0.01% tetramethylethylene diamine (TEMED)) with cathode (0.1 M Tris-HCl, 0.1M Tricine, 0.1% SDS) and anode buffer (0.2M Tris, pH 8.9). The gel was loaded with 40 µg protein per lane (in LDS loading buffer containing 5% mercaptoethanol, 5 min at 95°C) for approximately 90 min at 120 V. All proteins were subsequently electro blotted on nitrocellulose membranes (Hybond, Amersham Biosciences) for 1 h at 100V in transfer buffer (25 mM Tris, 192 mM Glycin). After blocking the membranes with 5% Amersham^{TM} ECL^{TM} blocking agent (GE healthcare) in PBS-Tween 0.1% wash-buffer (ECL-PBS-T) for 1h at RT, the respective primary antibody (Table 5) was diluted in 1% ECL-PBS-T and incubated for 15 min at RT and overnight at 4°C. Following three 10 min PBS-T washing steps, the membrane was incubated for 90 min at RT on a shaker with the according secondary antibody in 1% ECL-PBS-T (Table 5). After repeated washing of the nitrocellulose membrane three times for 10 min with PBS-T, the immunoreactive bands were visualized using the Amersham^{TM} ECL^{TM} immunoblotting detection system (GE healthcare) for 5 min at RT. GeneTool Software (Syngene, Cambridge, UK) was used to quantify the signal, data was analyzed with Adobe Photoshop CS6 and normalized to the internal GAPDH signal.

4.5 Cell culture experiments

4.5.1 Primary cell culture of peritoneal macrophages

Peritoneal macrophages were prepared from adult wt or APP+ mice euthanatized with dry CO_2. The peritoneum was carefully exposed, 10 ml sterile PBS was i.p. injected and the mouse was gently shaken for 1 min. Next, PBS containing the resident macrophages was slowly withdrawn and centrifuged for 7 min at 800 rpm. Cells were counted, plated at desired density in Roswell Park Memorial Institute medium (RPMI; Invitrogen) supplemented with 10% FBS and 50 U/ml penicillin/streptomycin (PenStrep; Invitrogen) and maintained at 37 °C in a 5% CO_2 humidified atmosphere.

4.5.2 Isolation and culture of CD11b+ cells

Isolation of CD11b+ cells was performed from brain tissue of APP+ or wt mice. Mice were euthanized with dry CO_2 and transcardially perfused with ice cold PBS. The brain was extracted, the cerebellum and olfactory bulb was discarded and the remaining tissue was manually cut finely in HBSS using scalpels. Subsequently, the tissue was dissociated into a cell suspension using the MACS®Neural Tissue Dissociation Kit (P) (Miltenyi Biotech) following the manufacturer's protocol. Briefly, the tissue was digested using enzymes and buffers supplemented with the kit at 37°C and homogenization with the gentleMACS® Dissociator (Miltenyi Biotech). Afterwards, the homogenate was filtered through a 70 µm mash filter, centrifuged (1300 rpm, 10 min) and suspended in ice cold MACS buffer (PBS, pH 7.2, 0.5% FBS). Next, cells were incubated with 20 µl magnetic CD11b+ MicroBeads (Miltenyi Biotech) per brain hemisphere and incubated for 15 min at 4°C. After a washing step, the cell suspension was resuspended in 1500 µl of MACS buffer and separated over LS magnetic columns (Miltenyi Biotech) placed in the MidiMACS® magnetic separation unit (Miltenyi Biotec). Cells were counted, 10^6 cells were plated per well in a 24 well plate containing DMEM supplemented with 10% FBS and 50 U/ml PenStrep and maintained at 37°C in a 5% CO_2 humidified atmosphere.

4.5.3 Viability assay

To evaluate the maximal tolerated concentration of Ebselen *in vitro*, a WST-1 (Life Technologies) cell viability assay was performed according to the manufacturer's instructions. For this, peritoneal macrophages were extracted from wt mice as

described, $5x10^4$ cells per well were plated in a 96 well plate and maintained overnight (37°C, 5% CO_2). The next day, medium was changed and indicated amounts of Ebselen, DMSO or pure medium as negative control were added and incubated for 24 h (37°C, 5% CO_2). Indicated concentrations of hydrogen peroxide (H_2O_2) were used as positive control. Afterwards, 10 µl WST-1 was added per well and incubated for 4 h at the same conditions, followed by 1 min thorough shaking. Cell viability was measured at 450 nm on a Tecan Infinite® 200M (Tecan) Photometer with a reference wavelength of 600 nm. Values were blank reduced to wells containing only supplemented RPMI.

4.5.4 *In vitro* IL-1β and TNFα protein expression

To quantify the effects of Ebselen treatment on NALP3 inflammasome dependent (IL-1β) and independent (TNFα) protein expression *in vitro*, peritoneal macrophages from wt mice were extracted as described and 10^6 cells were plated in a 24 well plate. To activate the NALP3 inflammasome *in vitro* LPS, acting over TLRs, as first signal and adenosine-tri-phosphate (ATP), acting as second sterile inducer, were used ([147]; see Figure 5). 24 h after extraction and plating of peritoneal macrophages, culture medium was discarded and LPS (1 µg/ml) with 50 µM, 100 µM Ebselen or vehicle (DMSO) diluted in culture medium was added to stimulate the cells. An equivalent amount of PBS in medium was used as a negative control for stimulation. After 24 h of incubation (37°C, 5% CO_2) 5 mM ATP was added for 30 min, then cell supernatants were collected and measured for protein content with the respective Elisa following the manufacturer's protocol (eBioscience). 50 µl of supernatant were used as technical duplicates and diluted to fit into the range of the standard curve. Absorption was measured at 450 nm and 570 nm (for wavelength correction) on a microplate reader (Infinite® 200M, Tecan) and analyzed using the Magellan™ Software.

4.5.5 Phagocytosis assay

To evaluate the influence of Ebselen on microglial phagocytosis *in vitro*, CD11b+ cells from 120 day old APP+ and wt mice were extracted and plated on cover slips in 24 well plates as described (4.5.2). After one day, medium was changed and cells were stimulated with 50 µM Ebselen or DMSO. After another 24 h medium was changed to serum-free DMEM containing 50 µM Ebselen or DMSO to starve the cells and thus induce phagocytosis. Yellowgreen fluorescent Fluoresbrite® carboxylated microspheres (2 µm diameter, Polysciences Europe GmbH) were coated with FBS by shaking at 1000

rpm for 30 min at RT. Microspheres were centrifuged at 3000 rpm for 5 min and then washed twice in DMEM, followed by a centrifugation step at 3000 rpm for 5 min. Finally, the coated beads were resuspended in DMEM and applied to the plated cells at $8.4x10^6$ microspheres per well. After 30 min incubation (37°C, 5% CO_2), cells were washed twice with pre-warmed PBS, followed by overnight fixation with 4% PFA at 4°C. The next day, in order to stain CD11b+ cells, the coverslips were washed three times with PBS and blocked with 10% NGS in PBS-TX for 1 h at RT on a shaker. The Iba1 primary antibody (Table 3) was diluted 1:500 in 5% NGS in PBS-TX and applied to the cells for 2 h at RT on a shaker. Rinsing the cells again three times with PBS was followed by 90 min incubation at RT on a shaker with AlexaFluor®568-conjugated anti-rabbit IgG (Table 3; in 5% NGS in PBS-TX). Finally, cover slips were rinsed with PBS (3x) and mounted with 4',6-Diamidino-2-Phenylindole (DAPI)-containing aqueous mounting medium (Fluoroshield® Mounting Medium with DAPI, abcam). Phagocytosis was analyzed from confocal pictures (10 ROI per condition, 3 animals per genotype) acquired with Zeiss Axio Observer Z1 and the software Axio vision 4. For evaluation the percentage of phagocytic microglia per image was determined using the ImageJ cell counter plugin in addition to the phagocytic index, as described [102].

4.6 Statistical analysis

All data was expressed as mean ± standard deviation (s.d.). For comparison of the mean between two groups, statistical analysis was performed by applying the Mann-Whitney U-test in GraphPad Prism 5. Comparisons of the mean among more than two groups were undertaken using a one-way or two-way analysis of variance (ANOVA) with Tukey's multiple comparisons post-test, as indicated in the figure legends. P values of less than 0.05 were considered to be significant and were indicated as follows: * $p < 0.05$, ** $p < 0.01$, *** $p < 0.001$ and **** $p<0.0001$.

5 Results

For the *in vivo* characterization of microglia replacement by peripherally-derived myeloid cells using CD11b-HSVTK mice in the healthy and AD diseased brain, technical establishment of long-term *in vivo* two-photon imaging together with the surgical procedures for CD11b-HSVTK depletion had to be established.

5.1.1 Technical establishment of long-term two-photon imaging and microglial depletion

First, I had to establish two-photon imaging and surgery techniques, which had not been used in our lab so far. To enable long-term microscopy, I decided to use chronic cranial windows instead of thinned skull techniques, which only allow up to three repeated imaging sessions over time ([148]; see discussion chapter 6.1). The window technique was adapted from a published protocol and trained to perfection by installing the cranial window over an intact Dura mater being as non-invasive as possible to circumvent microglial activation after the surgery [139]. Furthermore an imaging setup to fixate operated mice under the microscope was needed. For this, first a custom made imaging apparatus, published by Hefendehl *et al.,* was optimized by Dr. Jan Leo Rinnenthal (Neuropathology, Charité – Universitätsmedizin Berlin) [139]. The custom made titanium ring with a frontal guide notch and circular guide groove was permanently attached around the cranial window with dental cement and ensured head fixation of the animals at identical angles between long-term imaging sessions. The mouse with an installed custom made titanium ring was fixated in a custom made imaging apparatus, which was installed at the two-photon microscope facility prior each imaging session.

To induce repopulation of the brain by peripherally-derived myeloid cells, the established protocols in the lab used an icv cannula for GCV delivery in order to deplete CD11b-HSVTK+ microglia. Since this cannula was too big to fit on the skull together with the custom made titanium ring, approaches for topical GCV delivery were tested to circumvent icv cannula installation. In these cases, the cranial window was installed, leaving a hole in the dental cement around the cranial window of 5 mm diameter. Through the gap, 50 mg/ml GCV was applied to anesthetized animals daily and manually with a syringe. Even though microglia were depleted efficiently in the area of application, this setup led to severe side effects, such as infections and bleeding, as well as death due to the daily anesthesia. Thus, an automated approach was

established, where a miniosmotic pump filled with 50 mg/ml GCV was connected to tubing that allowed topical GCV application when installed together with an angular cranial window (Figure 10A). Microglia were depleted up to 90% in the area of GCV application after ten days (Figure 10B), mice did not suffer from infections or bleedings and showed normal survival rates. Nevertheless, the angular window showed signs of turbidity after one month of installation and could not be used for microscopy thereafter. One can therefore conclude that the topical automated application of GCV is a useful tool for short term studies of microglial depletion, as it is not invasive in comparison to icv GCV administration and leads to a robust local microglial depletion. For long-term microscopy, a 4 mm diameter cranial window was installed on the left hemisphere and 2.5 mg/ml GCV was administered via a special icv cannula that fitted onto the right hemisphere (Figure 10C). As established in our lab, icv administration of 2.5 mg/ml GCV leads to microglial depletion of >90% in the whole brain after ten days (see Figure 6).

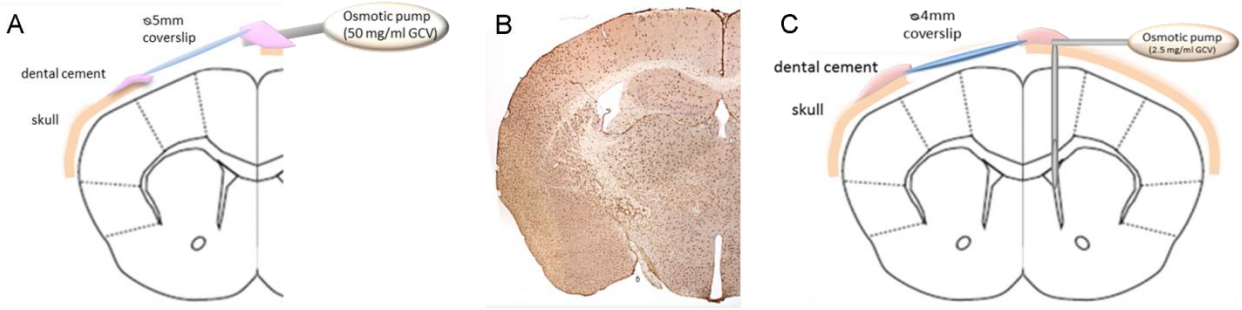

Figure 10: Technical establishment of *in vivo* microglial depletion. (A) Scheme depicting the installation of an angular cranial window (5 mm diameter) with topical administration of 50 mg/ml GCV via a miniosmotic pump. (B) GFP staining of microglia depleted via topical administration of GCV in FracGFP$^{+/-}$;TK+ mice shows a major reduction of cells in the application area (>90%). (C) Scheme depicting the installation of a cranial window (4 mm diameter) with icv administration of 2.5 mg/ml GCV via a miniosmotic pump.

5.1.2 Establishing the visualization of microglia

Next to the establishment of microglial depletion, I had to determine the fluorescent properties of two different microglia reporter mouse lines. The available mouse lines were: the CX_3CR1-GFP (termed FracGFP) mice, where GFP is knocked into the gene of the fractalkine receptor as described in 4.1.1, and Iba1-GFP mice, where GFP is expressed under the control of the Iba1 promoter.

This analysis showed that FracGFP$^{+/-}$ mice are brighter than Iba1-GFP+ mice (Figure 11A). Furthermore, imaging of these mice over one hour confirmed that the fluorescent

signal of FracGFP$^{+/-}$ animals is less prone to fluorescent bleaching (Figure 11B). Colocalization staining and stereological quantification of brain sections from both strains showed that both mouse models, namely FracGFP$^{+/-}$ and Iba-GFP+, label all Iba1 positive cells in the brain, incorporating microglia, perivascular macrophages and other subtypes of myeloid cells (Figure 11C, D). Due to the evaluated advantages in certain fluorescent properties of FracGFP$^{+/-}$ mice, we decided to use this line in all experiments.

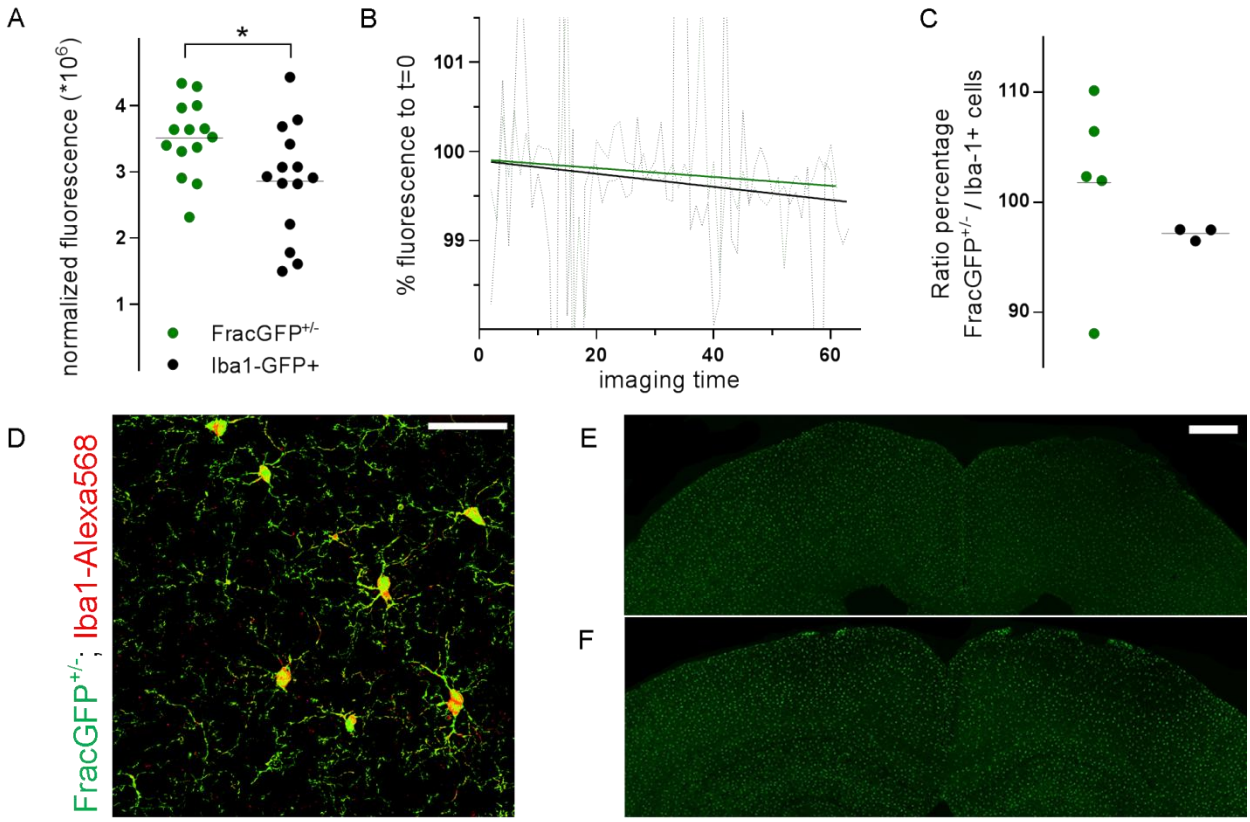

Figure 11: Technical establishment of microglia visualization and experimental start point. (A) Mean fluorescent intensity of FracGFP$^{+/-}$ and Iba1-GFP+ mice normalized to background. N = 14 cells (B) Bleaching curves of FracGFP$^{+/-}$ and Iba1-GFP+ animals plotted as mean fluorescence over time divided by the fluorescence of the first imaging time point. A less pronounced linear decline of fluorescence depicts greater bleaching robustness. N = 3 animals (C) Stereological cell count of Iba1-Alexa568-stained and GFP-tagged Iba1-GFP+ and FracGFP$^{+/-}$ cells. One dot is depicting one analyzed mouse brain. (D) Representative picture of a FracGFP$^{+/-}$ cortex region stained with Iba1-Alexa568 for colocalization of signals, as analyzed in C (scale 50 µm). (E, F) No morphological signs of microglial activation are visible in the cortex of FracGFP$^{+/-}$ mice with an installed chronic cranial window after two (E) or seven days (F; scale 500 µm). Statistics (A, C): Mann-Whitney test.

As there are conflicting reports about microglial activation after installation of a cranial window [149, 150], I validated if microgliosis induced by the required manipulation is a caveat in the experimental setup. Therefore, a cranial window was installed and FracGFP$^{+/-}$ mice were sacrificed two (Figure 11E) or seven (Figure 11F) days after the

surgery. No morphological signs of microglial activation were seen at both time points, indicating that microscopy of operated mice can, in principle, be started as early as two days after cranial window installation.

5.2 Project Aim 1: In vivo *characterization of myeloid cell dynamics in the healthy brain*

5.2.1 *In vivo* monitoring of the replacement of resident microglia by peripherally-derived myeloid cells in the healthy central nervous system

To characterize the microglial depletion process in CD11b-HSVTK mice and to follow the repopulation process of peripherally-derived myeloid cells, a visual discrimination of these cell types was required. As described, up to date no stand-alone marker exists to distinguish microglia from peripheral monocytes. Iba1 and the fractalkine receptor (CX_3CR1) are most commonly used to identify microglia in the brain, but these markers are likewise expressed by myeloid cells in the periphery. Thus, all available transgenic mouse models fluorescently labeling microglia, such as the herein used FracGFP$^{+/-}$ mice, also label peripheral myeloid cells with the same fluorophore. It has therefore not been possible so far to distinguish these cell types in currently available genetic mouse models. Therefore, we established a protocol using bone marrow (BM) chimeric mice allowing for discrimination of microglia in the brain from peripheral myeloid cells.

First, FracGFP$^{+/-}$ mice were crossed to CD11b-HSVTK mice to enable microglial depletion. Taking into account the previous work from the group of Frank Heppner (Neuropathology, Charité – Universitätsmedizin Berlin), where TK mediated depletion of microglia in an AD-like context at the age of 200 days had been achieved (see chapter 3.4), the experimental procedure had to be started at the age of 127 days in FracGFP$^{+/-}$;TK+ or - mice in order to model the respective findings in an AD-like setting (second aim of this thesis). Therefore, FracGFP$^{+/-}$;TK+ or – mice at the age of 127 days were lethally irradiated, resulting in the extinction of all hematopoietic cells, including green fluorescent cells in the periphery, while sparing FracGFP$^{+/-}$ positive microglia in the CNS. After subsequent adoptive transfer of bone marrow taken from tdRFP mice into FracGFP$^{+/-}$;TK+ or – recipients, all peripheral immune cells were tdRFP-positive, while microglia carried the GFP signal. After one month of recovery, microglial depletion via icv GCV delivery was initiated and a chronic cranial window was installed.

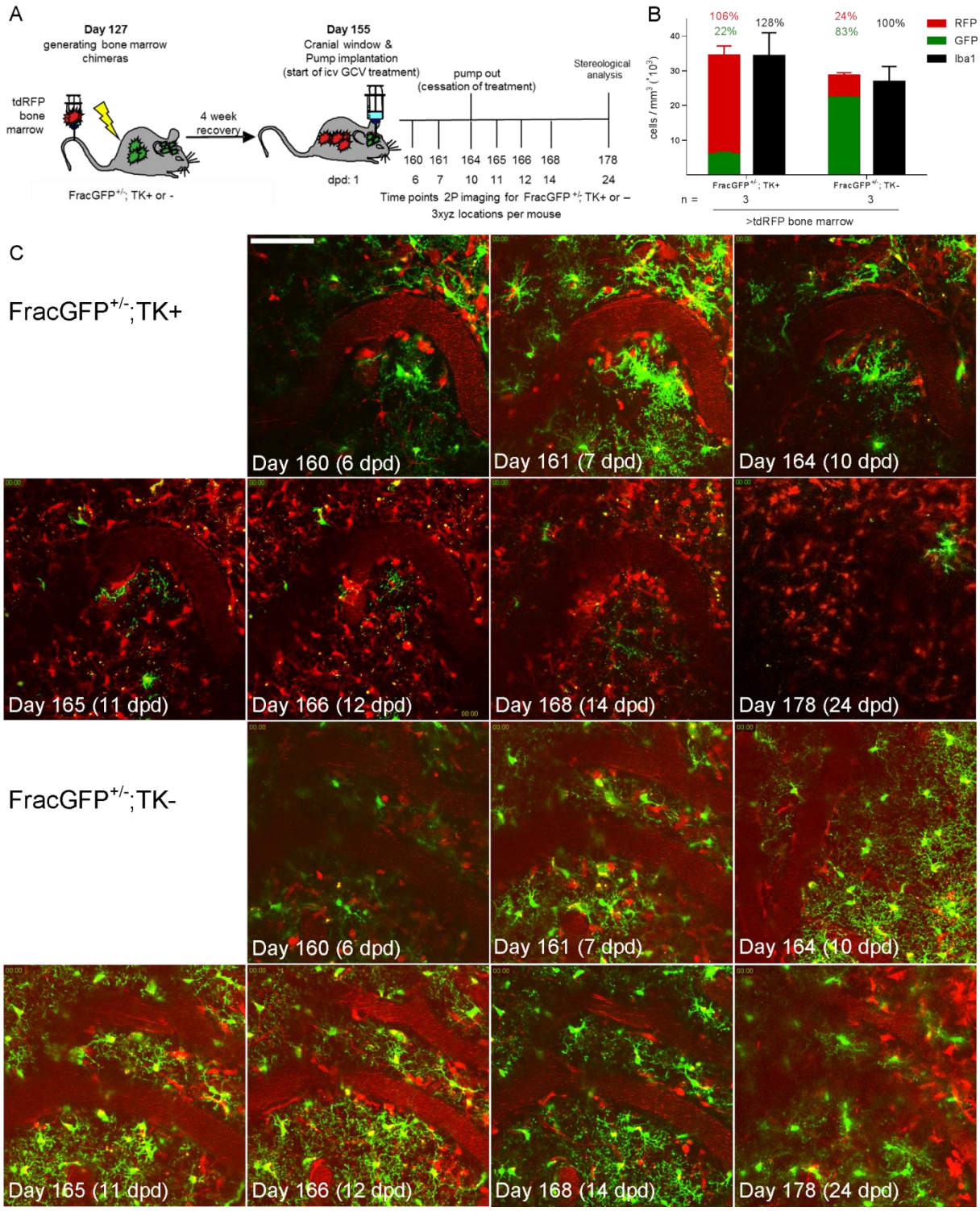

Figure 12: *In vivo* imaging of endogenous microglia replacement by peripherally-derived myeloid cells. (A) Experimental setup: To distinguish endogenous microglia from peripherally-derived myeloid cells FracGFP$^{+/-}$; TK+ or – mice were lethally irradiated and reconstituted with BM from tdRFP reporter mice at an age of 127 days. After one month of recovery, a cranial window was installed together with a miniosmotic pump connected to an icv cannula for delivery of 2.5 mg/ml GCV. After five days of recovery, mice were imaged at the depicted days using two-photon microscopy. Three ROI per animal were imaged for a minimum of 30 minutes. (B) Stereological counts of Iba1, GFP and tdRFP positive cells at termination of the experiment. (C) Representative maximum intensity projections from the first time point

of recorded two-photon imaging movies for both experimental conditions. The blood landmarks demonstrate the precise relocation of the imaging positions over time. Scale 100µm.

Previous experiments had shown that peripheral cells start to repopulate the brain six days after start of microglial depletion in a similar experimental setup (data not shown). Therefore, mice were imaged six and seven days after initiation of the depletion of microglia (mouse age 160 and 161 days, corresponding to days post depletion (dpd) 6, 7) to visualize the first repopulating cells. Additionally, imaging was performed 10 days after initiation of microglial depletion to visualize the endpoint of GCV delivery, where >90% of resident microglia are known to be ablated [104]. The repopulation process was followed at four more time points over the following two weeks (mouse age 165, 166, 168 and 178 days corresponding to dpd 11, 12, 14, 24; Figure 12A). For each time point it was possible to relocate the exact imaging position due to the establishment of the custom made head fixation system, additionally blood vessel landmarks were used as reference (Figure 12C). As expected, tdRFP-peripherally-derived myeloid cells started to invade the brain at day 160 (6 dpd) in microglia depleted FracGFP$^{+/-}$;TK+ mice. In these mice, nearly no GFP+ microglia were found at day 165 (10 dpd) and the brain was already repopulated entirely with red fluorescent cells that adapted microglial morphology. In FracGFP$^{+/-}$;TK- controls, where no microglia depletion occurred, tdRFP+ peripheral cells could only rarely be detected in the brain (Figure 12C). In addition, these rare tdRFP+ cells in TK- mice did not exhibit the typical ramified morphology of resting microglia and migrated rapidly through the tissue (Figure 13A).

After termination of the experiment, brains were stereologically analyzed for cell composition, which was shown to reflect the *in vivo* imaging movies: in FracGFP$^{+/-}$;TK- control mice, peripherally-derived cells contributed only to 24% to the overall amount of CNS myeloid cells (6448 ± 773), while the majority of Iba1+ cells (26862 ± 4404) was of resident origin, i.e. consisted of FracGFP$^{+/-}$ microglia (22234 ± 207; Figure 12B). The invasion of peripheral cells in the control context was most likely due to leakiness of the BBB as a result of irradiation and/or tissue disruption by the icv cannula. Microglia depleted FracGFP$^{+/-}$;TK+ mice, however, had an increased Iba1+ cell number in the brain (34302 ± 6667; 128%), that was mainly composed of peripherally-derived myeloid cells (28553 ± 2741), while 78% of resident microglia were depleted (down to 5900 ± 1141 cells; Figure 12B).

5.2.2 Analysis parameters are not substantially influenced by the CD11b-HSVTK genotype

Movies from two-photon imaging suggested, that peripherally-derived myeloid cells resemble resident microglia phenotypically. To thoroughly characterize the morphology of these newly recruited myeloid cells, relevant soma and process tree parameters of the distinct cell types were analyzed. In order to allow the comparison of endogenous microglia in non-depleted FracGFP$^{+/-}$;TK- animals and peripherally-derived myeloid cells in FracGFP$^{+/-}$;TK+ animals, we aimed to ensure that the TK genotype does not intrinsically influence the parameters. Thus, endogenous microglia as well as peripherally-derived cells underwent soma reconstruction in FracGFP$^{+/-}$;TK- and + animals using Imaris 7.0 (Bitplane). While soma movement over 30 minutes of recording (termed soma speed) was increased in peripherally-derived cells of TK- (10.08 ± 5.43 nm/s) compared to TK+ cells (8.29 ± 4.57 nm/s), endogenous microglia showed no differences (TK+ 6.73 ± 3.21 nm/s; TK- 6.85 ± 2.88 nm/s; Figure 13A).

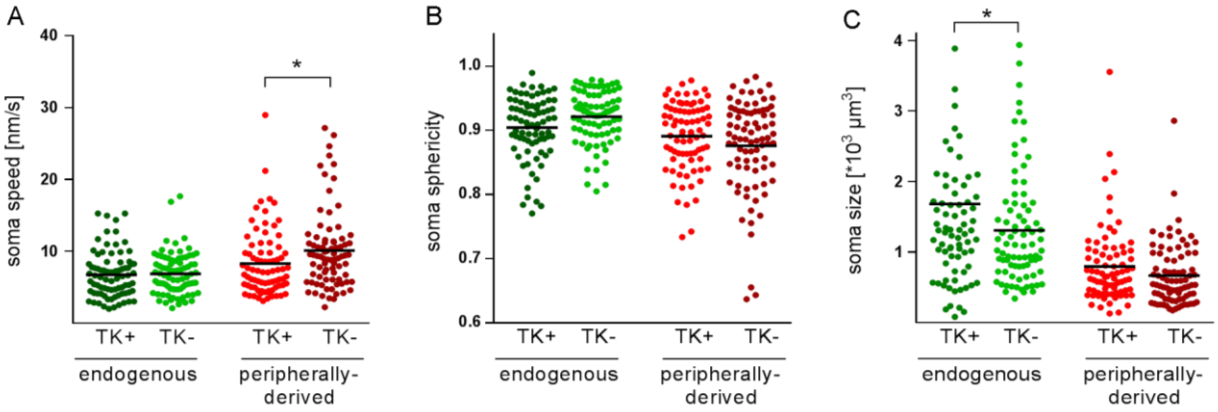

Figure 13: Soma parameters are not substantially influenced by the CD11b-HSVTK genotype. Parameters of reconstructed somata from all imaged ROI at all investigated time points were analyzed for microglia as well as for peripherally-derived myeloid cells from FracGFP$^{+/-}$;TK+ (TK+) and FracGFP$^{+/-}$;TK- (TK-) animals upon GCV delivery. (A) Soma speed measured for 30 minutes. (B) Soma sphericity, i.e. roundness of the soma. (C) Soma size. Statistics: 1-way ANOVA, only significance between TK+ and TK- cells in endogenous and peripherally-derived groups is shown; One dot equals one cell, N=4 animals per genotype, 3 ROI per animal.

This reflects the impression from imaging movies that peripherally-derived myeloid cells in non-depleted TK- animals did not adopt microglial morphology, but were rapidly moving within the CNS environment. The measure for the roundness of the soma, i.e. soma sphericity, was unchanged between the experimental groups (endogenous: TK+ 0.90 ± 0.05; TK- 0.92 ± 0.04; peripheral: TK+ 0.89 ± 0.05; TK- 0.88 ± 0.07; Figure 13B). In addition, soma size of peripherally-derived cells did not differ between TK+

(795.3 ± 541.4 µm^3) and TK- (663.6 ± 433.9 µm^3) animals. Only soma size of endogenous microglia was significantly elevated in TK+ animals (1682 ± 1376 µm^3; TK- 1308 ± 901.9 µm^3), as these cells undergo activation before undergoing GCV-mediated cell death (Figure 13C), offering an explanation for these differences.

Thus, soma parameters are not substantially influenced in otherwise untreated CD11b-HSVTK mice.

5.2.3 Peripherally-derived myeloid cell somata move faster and are smaller in size

As mentioned in the previous chapter, two-photon movies indicate that peripherally-derived myeloid cells resemble microglia phenotypically. To assess the morphology of the newly invading cells more thoroughly, different cell body parameters of distinct cell types were analyzed. First, soma parameters of imaged cells were assessed with respect to putative changes over time. Thus, soma values of TK+ peripherally-derived myeloid cells and TK- endogenous microglia were analyzed for each imaged time point and plotted over time. Furthermore, TK+ endogenous microglia were included in the analysis at day six and seven dpd to characterize cells that undergo GCV-mediated cell death. Peripheral myeloid cells, invading the brain at day six and seven dpd, showed a more rapid soma speed compared to endogenous microglia at these time points (endogenous TK+: 10.33 ± 4.14 nm/s; endogenous TK-: 9 ± 2.56 nm/s; peripheral: 16.17 ± 7.16 nm/s; Figure 14B). Thereafter, the soma speed of the peripherally-derived myeloid cells stayed constant over time (Figure 14A).

Furthermore, we analyzed all soma parameters independently from how long they had been exposed to CNS tissue, as no major changes were detected when plotting them over time. Thus, resident microglia and peripherally-derived myeloid cells, previously analyzed separately for each imaging time point, were now combined into a pool of cells. Here, analysis of soma speed over all imaged time points showed an increase in the motility of peripherally-derived myeloid cells, similar to the results from day six and seven dpd (endogenous: 10.29 ± 3.93 nm/s; peripheral: 12.81 ± 5.47 nm/s; Figure 14C). Thus, the soma speed of peripherally-derived myeloid cells remained increased, at least when recorded for 24 days in the brain.

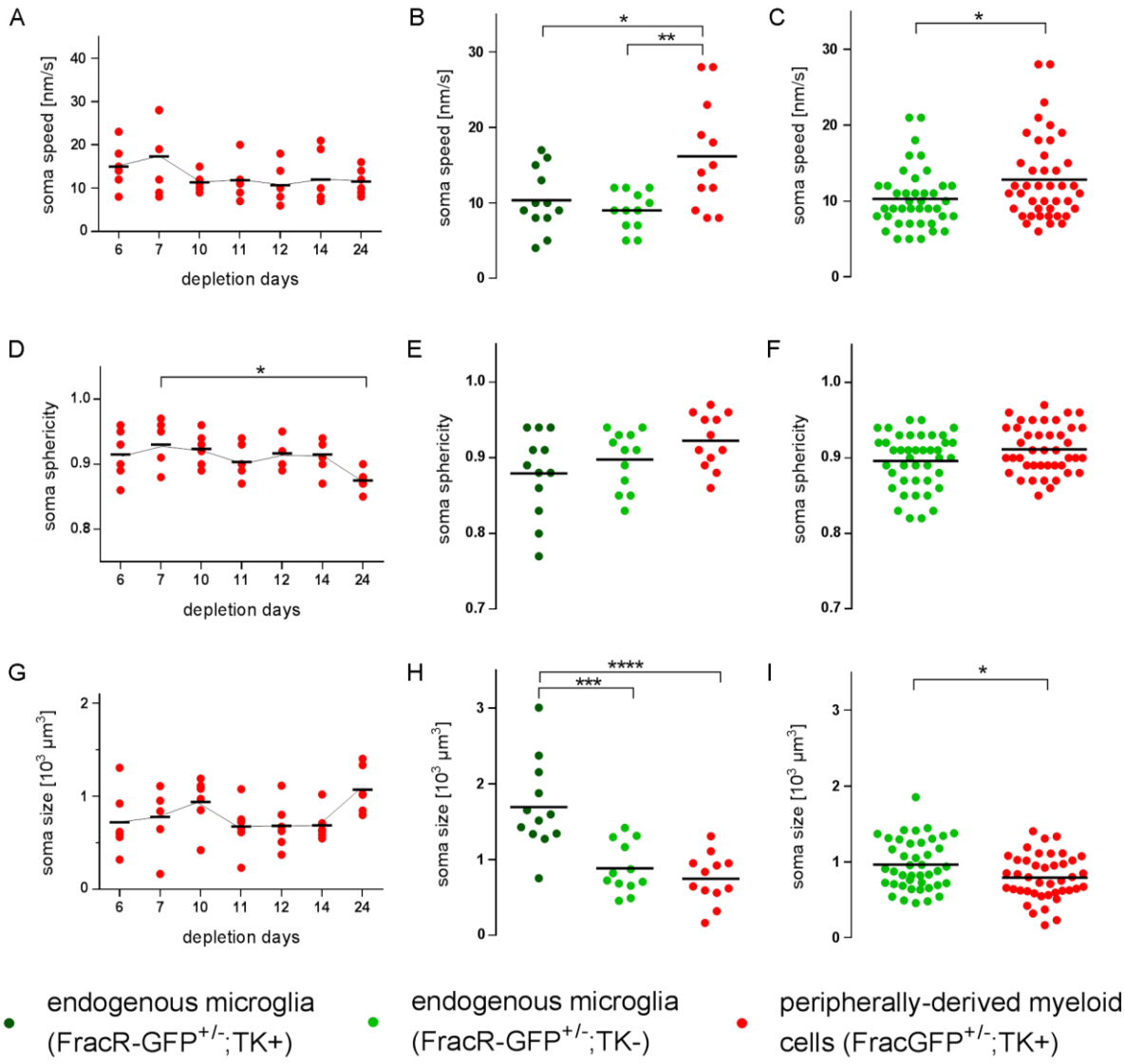

Figure 14: Somata of peripherally-derived myeloid cells are smaller and faster compared to endogenous microglia. (A) Soma speed of peripherally-derived myeloid cells over time in the CNS. (B, C) Soma speed of resident microglia and peripherally-derived myeloid cells at (B) day six and seven in the CNS tissue and (C) analyzed over all recorded time points. (D) Soma sphericity of peripherally-derived myeloid cells over time in the CNS. (E, F) Soma sphericity of resident microglia and peripherally-derived myeloid cells (E) at day six and seven in the CNS and (F) analyzed over all recorded time points. (G) Soma size of peripherally-derived myeloid cells over time in the CNS. (H, I) Soma size of peripheral cells and endogenous microglia at (H) day six and seven dpd and (I) analyzed over all recorded time points. Statistics: 1-way ANOVA (A, B, D, E, G, H), Mann-Whitney test (C, F, I). One dot represents the average value of 9 cells from one ROI, 3 animals per genotype with 3 ROI per animal.

When analyzing the roundness of cell somata, i.e. soma sphericity, the peripherally-derived myeloid cells appeared to get less spherical after 24 days in the brain tissue (Figure 14D). Nevertheless, soma sphericity did not differ between compared cell types at day six and seven dpd (endogenous TK+: 0.88 ± 0.06; endogenous TK-: 0.9 ± 0.04; peripheral: 0.92 ± 0.03; Figure 14E) nor over all analyzed time points (endogenous: 0.9 ± 0.04; peripheral: 0.91 ± 0.03; Figure 13F).

Likewise, soma size of peripherally-derived myeloid cells was not altered over time and did not differ at day six and seven dpd compared to TK- microglia (Figure 14G, H). Nevertheless, these cells were smaller than endogenous microglia when analyzed over all time points (endogenous: 963.3 ± 329.6 µm^3; peripheral: 792.9 ± 294.7 µm^3; Figure 14I). As already described in Figure 13C, an increased soma size of TK+ endogenous microglia was detected at day six and seven dpd, which is well explained by the activation of these cells following GCV-mediated cell death (endogenous TK+: 1692 ± 591.8 µm^3; endogenous TK-: 883.8 ± 332.2 µm^3; peripheral: 748.6 ± 327.1 µm^3; Figure 14H).

In summary, peripherally-derived myeloid cells invade the brain already six days after initiation of GCV-mediated depletion of resident microglia and adapt microglial morphology. Their somata are largely similar to that of endogenous microglia, while being slightly faster and smaller over a period of 24 days in the CNS.

5.2.4 Processes of peripherally-derived myeloid cells are smaller and less ramified

Next, we aimed to compare parameters that describe microglial processes. For this, the amount of process branch points per cell, the sum of all process lengths as well as the amount of primary filaments, defined as processes originating directly from the soma, were analyzed. Again, the time-dependent evolution of all investigated parameters were analyzed by plotting them over time, where peripherally-derived myeloid cells did not show any alterations (Figure 15A, C, E). Thus, these cells did not change in process length or branching when being exposed to the brain tissue, at least within the observed time span of 24 days.

Furthermore, similar to the analysis of soma parameters, all analyzed processes of endogenous microglia and peripherally-derived myeloid cells were compared independently of the time exposed to the CNS tissue. Peripherally-derived cells had overall less branched and shorter processes (Figure 15B: endogenous: 45 ± 30; peripheral: 15 ± 9; Figure 15D: endogenous: 802.6 ± 401.2 µm; peripheral: 231.8 ± 104.7 µm). However, these changes in the process tree were not due to a reduced number of primary filaments originating from the soma (endogenous: 5 ± 2 µm; peripheral: 4 ± 2; Figure 15F).

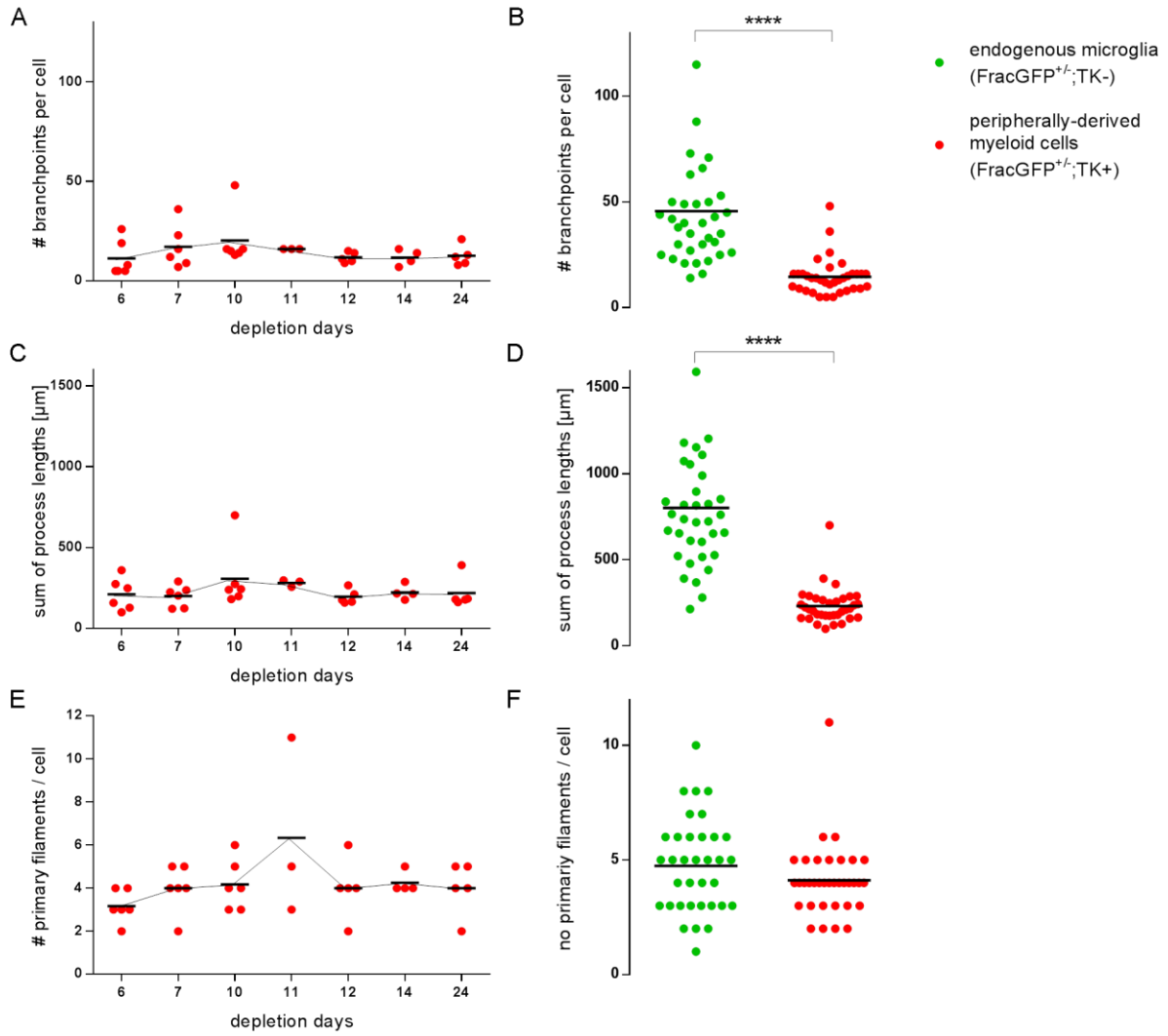

Figure 15: Peripherally-derived myeloid cells have shorter processes that are less ramified. (A, B) Branch points per cell of (A) peripherally-derived myeloid cells over time and (B) resident microglia and peripherally-derived myeloid cells analyzed over all time points. (C, D) Sum of all process' lengths per cell of (C) peripherally-derived myeloid cells over time and (D) resident microglia and peripherally-derived myeloid cells analyzed over all time points. (E, F) Amount of filaments originating from the cell soma of (E) peripherally-derived myeloid cells over time and (F) resident microglia and peripherally-derived myeloid cells analyzed over all time points. Statistics: 1-way ANOVA (A, C, E), Mann-Whitney test (B, D, F); One dot represents one cell from 3 animals per genotype; 3 ROI per animal.

In summary, peripherally-derived myeloid cells adapt microglial process morphology as soon as they enter the brain. However, the amount of primary filaments, and thus the foundation of the process arbor does not differ between these cells. Nevertheless, peripherally-derived myeloid cells have shorter and less branched processes, indicating that within 24 days – the time-span investigated by us - there is no additional, substantial evolution of processes once they have formed within the CNS microenvironment.

5.2.5 Processes of peripherally-derived myeloid cells are functional and react more rapidly towards a laser-induced lesion

Next, we aimed to test whether peripherally-derived myeloid cell processes are functional. For this purpose, process retractions and extensions of peripherally-derived myeloid cells as well as of endogenous microglia were quantified after 10 dpd up to 24 dpd in the CNS tissue. Here, no time-dependent changes in subtle process movements were detected (Figure 16A, B).

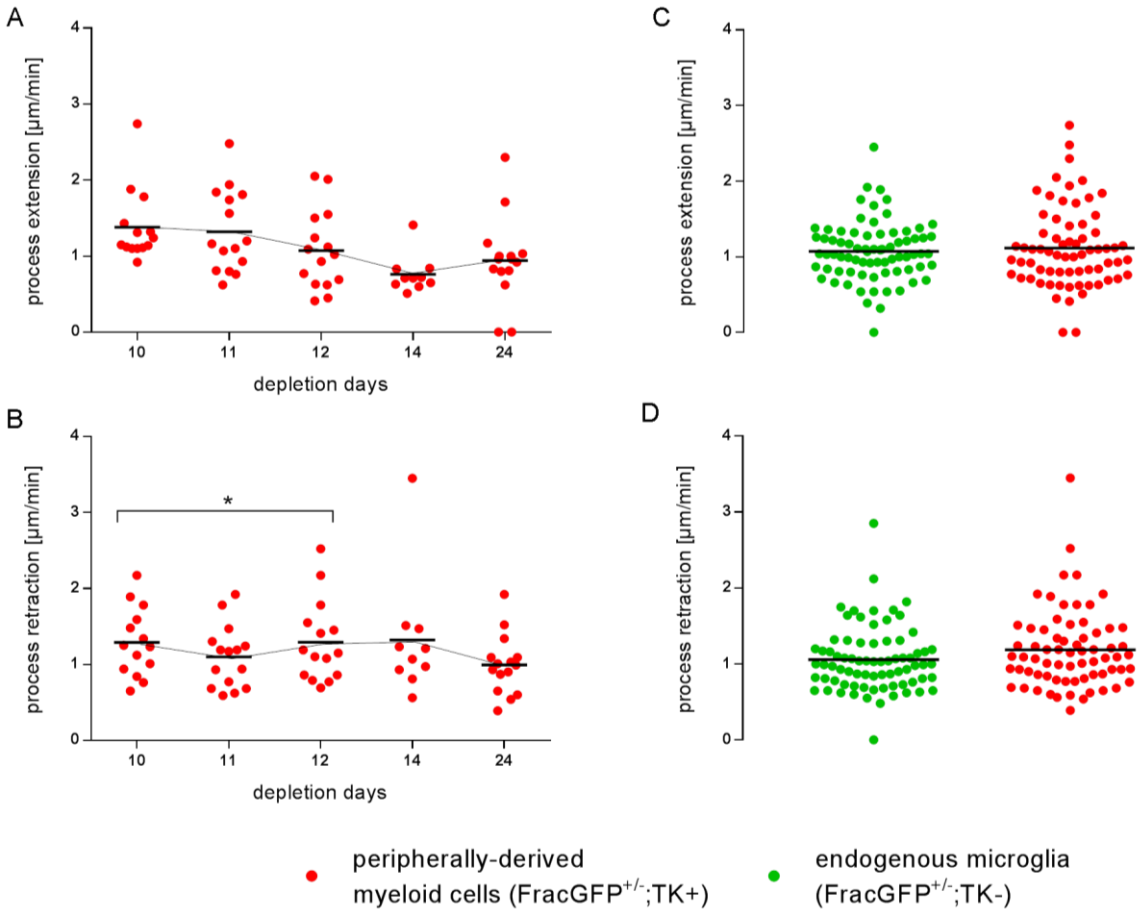

Figure 16: Peripherally-derived myeloid cells are able to extend and retract their processes to the same extent as microglia. Baseline movements of processes measured over five minutes. (A) Process extension speed of peripherally-derived myeloid cells over time. (B) Process retraction speed of peripherally-derived myeloid cells over time. (C) Process extension speed of endogenous microglia and peripherally-derived cells analyzed over all time points. (D) Process retraction speed of endogenous microglia and peripherally-derived cells analyzed over all time points. Statistics: 1-way ANOVA (A, B), Mann-Whitney test (C, D); One dot represents one process movement; 5 movements per ROI from 4 animals per genotype; 3 ROI per animal.

When looking at process movements independently of the imaging time point, peripherally-derived cells moved their processes at around 1.06 µm per minute (Figure 16C, D). These movements were not significantly different to those of endogenous

microglia, which showed a mean movement of 1.02 µm per minute (Figure 16C, D). Thus, peripherally-derived myeloid cells appear to be well equipped to scan the brain environment by extending and retracting their processes.

Furthermore, we quantified the ability of peripherally-derived myeloid cells to react to injury by measuring process movements towards a laser-induced lesion [4]. To this end, a small focal tissue damage was induced by a laser lesion in the cortex of the brain. As visible in Figure 17A, microglial processes immediately extended towards injury and appeared to “seal” the lesion with their processes shortly after 30 minutes. To our surprise, even though peripherally-derived myeloid cells had shorter, less branched processes, they were able to react faster to a laser-induced lesion by extending their processes with 0.68 ± 0.16 µm/min when compared to endogenous microglia (0.55 ± 0.µm/min; Figure 17B, C).

In summary, peripherally-derived myeloid cells have a functional process tree that is able to react faster towards an injury, compared to endogenous microglia.

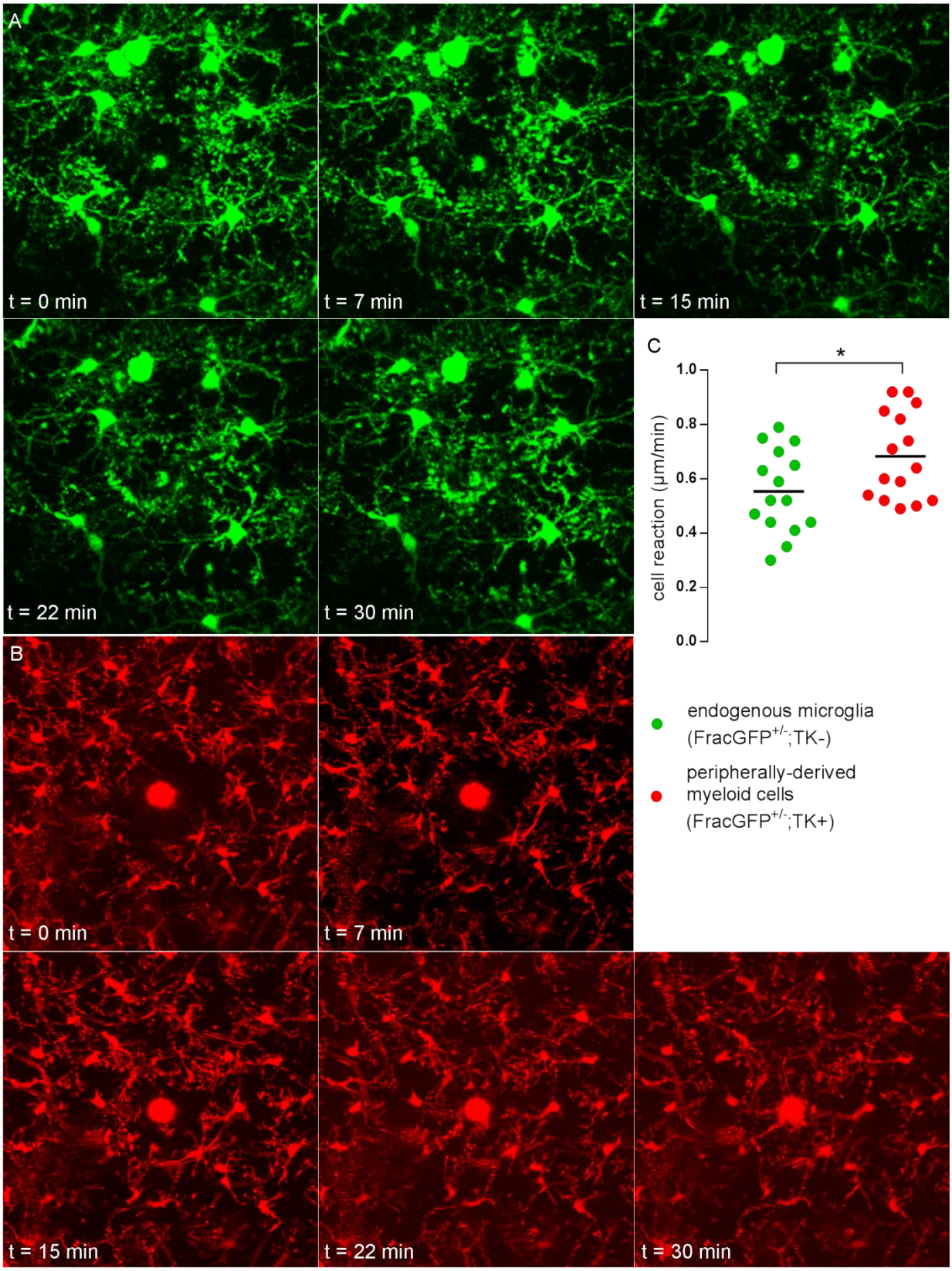

Figure 17: Peripherally-derived myeloid cells react faster to a laser-induced lesion. Representative maximum intensity projections from indicated time points of two-photon imaging videos. (A) Microglial process extension to a laser-induced tissue lesion. The cells extend their processes towards the auto-fluorescent lesion right after injury induction. The "sealing" of the lesion is not yet complete after 30 minutes. (B) Process extension of peripherally-derived myeloid cells to a laser-induced lesion. These cells

are faster the site-directed process motility towards lesion, reaching the injury after 30 minutes. (C) Quantification of process movements towards the lesion. N = 5 animals per genotype. Statistics: Mann-Whitney test.

5.2.6 Peripherally-derived myeloid cells are denser and more numerous in the cortex

Since the stereological analysis showed that more Iba1+ cells are found in repopulated brains (Figure 12B), the distribution of peripherally-derived myeloid cells in the CNS tissue was analyzed. For this purpose, the *in vivo* distances between endogenous microglia and peripherally-derived myeloid cells were derived from all recorded two-photon movies. To achieve this, the xyz coordinates of cell somata were used and the distances between these coordinates were calculated with a custom written program (Zoltan Czeresnyes, JIMI Berlin). We found, that peripherally-derived myeloid cells were in closer vicinity to each other compared to the cell-to-cell distances of endogenous microglia (Figure 18A).

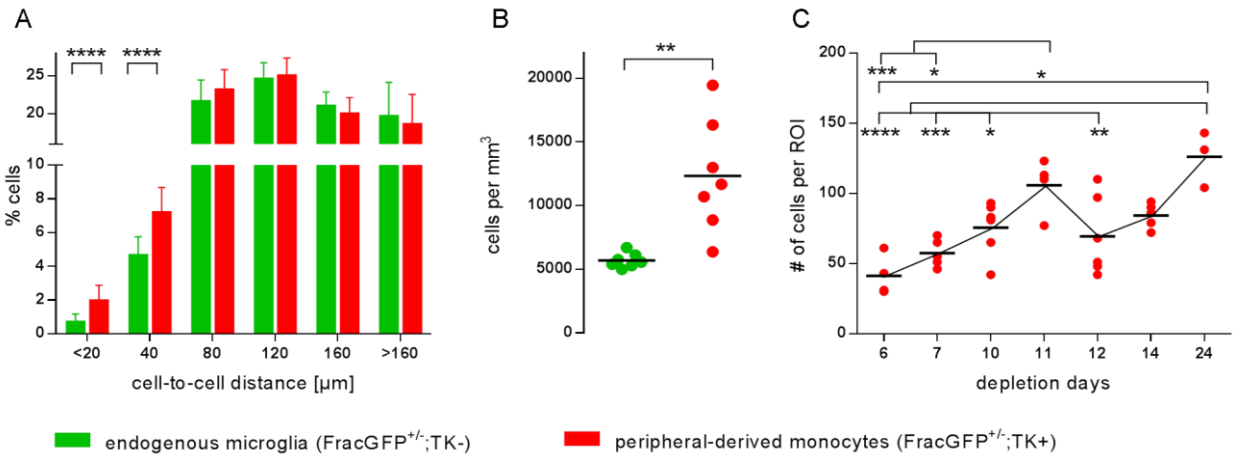

Figure 18: Peripherally-derived myeloid cells are arranged in denser networks compared to microglia. (A) Percentage of peripherally-derived myeloid cells and microglia in set cell-to-cell distance radii. (B) Cells per mm^3 brain parenchyma. (C) Amount of peripherally-derived cells in the brain at different time points in the CNS. One dot incorporates the average value of one ROI, 3 animals per genotype with 3 ROI per animal. Statistics: Counterpart comparisons between endogenous microglia and peripherally-derived myeloid cells: Mann Whitney test (A, B), 1-way ANOVA (C).

This explains the elevated number of cells in repopulated brains, which, in the cortex, increased in a time-dependent fashion at least until day 24 after microglial depletion (Figure 18C). In addition, as the processes of peripherally-derived myeloid cells were shorter, they require to be in closer vicinity to each other in order to cover the entire brain tissue with their processes. Thus, while ~5500 endogenous microglia were

present in 1 mm^3 of cortex, >11600 peripherally-derived myeloid cells were required to surveil the same volume of tissue (Figure 18B).

In summary, our data show that microglial depletion mediated through the CD11b-HSVTK transgene and subsequent repopulation of the brain by peripherally-derived myeloid cells starts as early as six days after the start of GCV treatment. The invading cells adopt a “microglial-like” morphology rapidly after brain tissue entry. The analyzed cell populations have similar shaped soma and a comparable predisposition of their process tree. Nevertheless, even if peripherally-derived myeloid cells mimic microglia well, they exhibit smaller somata with shorter and less branched processes when analyzing them over 24 days in the CNS tissue. Surprisingly, these newly incoming cells also appear to be more functional, as they are able to react faster to a laser-induced tissue injury, while baseline process extensions and retractions are comparable to endogenous microglia. Thus, we next tested this type of myeloid cell exchange and its effect in on Alzheimer’s disease, namely to test the functionality of these cells in combating amyloid deposits.

5.3 Project Aim 2: Replacement of resident microglia by peripherally-derived myeloid cells in Alzheimer’s disease

5.3.1 *In vivo* monitoring of the replacement of resident microglia by peripherally-derived myeloid cells in the Alzheimer diseased central nervous system

To characterize the microglial depletion process induced by the CD11b-HSVTK transgene followed by repopulation of peripherally-derived myeloid cells in the AD context, a similar experimental setup as described in project aim 1 (5.2.1) was chosen. We therefore crossed $FracGFP^{+/-}$;TK+ or – mice to APPPS1 mice, which develop an AD-like pathology (termed APP+ or –). For discrimination between microglia and peripheral myeloid cells, 127 day old mice of the various genotypes (Figure 19A) were lethally irradiated and reconstituted with tdRFP BM from the respective reporter mice, as described before. After one month of recovery, microglial depletion via icv GCV delivery was initiated and a chronic cranial window was installed. To enable the myeloid cell exchange in the CNS of AD-like mice, we chose an experimental setup with long-term delivery of GCV, which was shown to reduce amyloid burden (see chapter 3.4). After the start of depletion of resident microglia at an age of 155 days, the GCV osmotic

pump reservoir was exchanged for a long-term pump at day 165 in all experimental mice in order to ensure delivery of GCV until day 192. Imaging time points for healthy APP- control mice were very similar to those chosen in the first project aim, enabling long-term imaging of the repopulation process up to 38 days after starting microglial depletion. APP- (non-AD) control mice were sacrificed for stereological analysis after cessation of treatment at day 192. The depletion and repopulation in APP+ mice was imaged weekly for 48 days after the initiation of microglial depletion and mice were sacrificed for stereological analysis at day 202. (Figure 19A). Amyloid plaques were labeled by Methoxy-X04 injections i.p. 24 hours prior each imaging session in order to visualize Aβ plaques *in vivo*.

The stereological analysis to characterize cell composition reflected the *in vivo* imaging movies (Figure 20): in non-AD FracGFP$^{+/-}$;APP-;TK- (termed FracGFP$^{+/-}$;TK-) control mice, 32% CNS myeloid cells were of peripheral origin (9393 ± 4078), while the majority of Iba1+ cells (28853 ± 1630) was made up of FracGFP$^{+/-}$ myeloid cells, that is resident microglia (24989 ± 4078; Figure 19B). The invasion of peripheral cells in the control context could be explained by the leakiness of the BBB due to irradiation and/or tissue disruption by icv cannula implantation. Microglia-depleted FracGFP$^{+/-}$;APP-;TK+ (termed FracGFP$^{+/-}$;TK+) mice exhibited increased Iba1+ cell numbers in the brain (38447 ± 6596; 133%), that were mainly composed of peripherally-derived myeloid cells (31327 ± 2512; 109%). In this experimental setup 83% of microglia were depleted (down to 4994 ± 1676 cells; Figure 19B). Cell composition in AD mouse brains were comparable to the non-AD setting: FracGFP$^{+/-}$;APP+;TK+ brains consisted of 35% more numerous Iba1+ cells (33897 ± 5070) mainly comprising peripherally-derived myeloid cells (109%; 27261 ± 3051), while only a minority of resident endogenous microglia (down to 23%; 5756 ± 1540; Figure 19C) was detectable. On the other hand, FracGFP$^{+/-}$;APP+;TK- mouse brains mainly exhibited resident microglia and at best harbored 18% of peripherally-derived myeloid cells (4547 ± 916; Figure 19C).

When analyzing amyloid plaques positive for the 4G8 antibody after termination of the experiment, a trend towards a reduced amyloid load by the amount of plaques (TK+: 1030 ± 173/mm^3; TK-: 1570 ± 185/mm^3) and a trend towards a reduction in the area covered by amyloid burden (TK+: 4.04 ± 0.75%; TK-: 5.44 ± 1.69%) in the cortex could be detected, which, however, was not significant (Figure 19D).

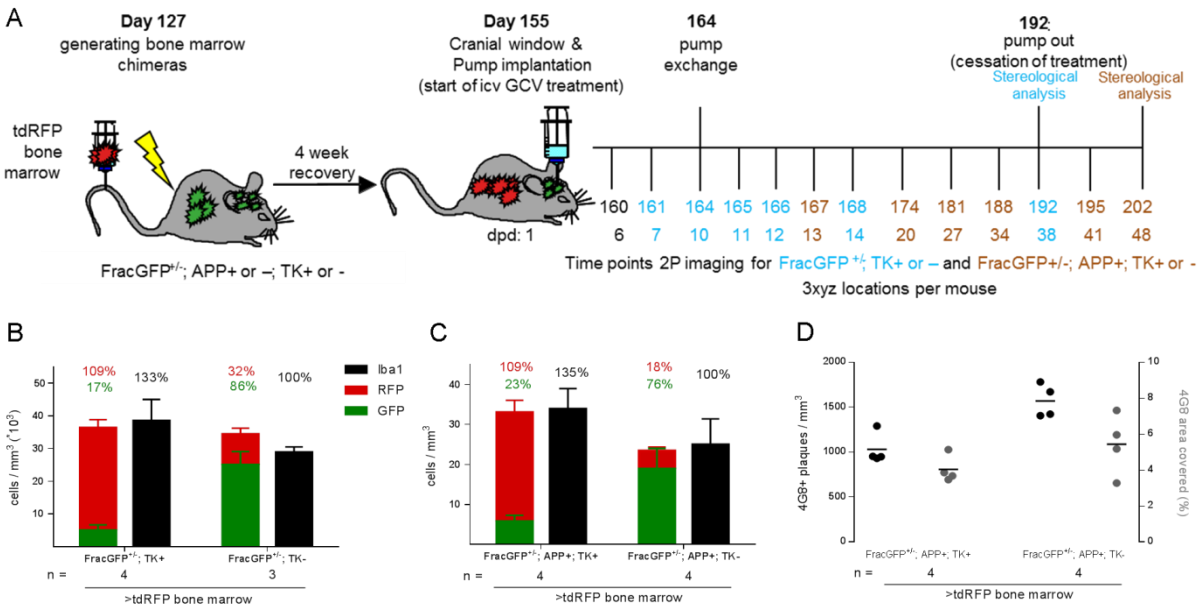

Figure 19: *In vivo* imaging of the replacement of endogenous microglia by peripherally-derived myeloid cells in AD-like mice – Cell and Plaque Counts. (A) Experimental setup: To distinguish endogenous microglia from peripherally-derived myeloid cells FracGFP$^{+/-}$;APP+ or -;TK+ or – mice were lethally irradiated and reconstituted with BM from tdRFP reporter mice at an age of 127 days. After one month of recovery, a cranial window was installed together with a miniosmotic pump connected to an icv cannula for delivery of 2.5 mg/ml GCV to induce microglial depletion. After five days of recovery, mice were imaged at the days mentioned in (A) using two-photon microscopy. GCV delivery was prolonged after ten days by implanting a new miniosmotic pump that ensured GCV-delivery for another 28 days until day 192. Three ROI per animal were imaged for a minimum of 30 minutes. Amyloid deposits in APP+ mice were labeled by Methoxy-X04 i.p. injection 24 hours prior to each imaging time point. (B, C) Stereological counts of Iba1-, GFP- and tdRFP-positive cells in (B) FracGFP$^{+/-}$;APP-;TK+ and – (termed FracGFP$^{+/-}$;TK+ and –) and (C) FracGFP$^{+/-}$;APP+;TK+ and – mice at termination of the experiment. (D) Stereological counts of 4G8-positive amyloid deposits in FracGFP$^{+/-}$;APP+;TK+ and – animals at termination of the experiment. Dpd = days post depletion. Statistics: Mann-Whitney test (D).

Similarly to project aim 1, the exact recovery of the imaging position was possible for every microscopy session due to our custom made head fixation system, since blood vessel landmarks and Methoxy-X04 labeled plaques could be re-identified (Figure 20A, B).

As expected, red peripherally-derived myeloid cells started to invade the brain at day 160 (6 dpd) in microglia depleted healthy FracGFP$^{+/-}$;TK+ mice (Figure 20A) as well as microglia depleted FracGFP$^{+/-}$;APP+;TK+ (Figure 20B) animals. In these mice nearly no GFP+ endogenous microglia were detected after day 167 (10 dpd), while the brain was already entirely repopulated with red fluorescent cells originating from the periphery, that had adapted “microglia-like” morphology.

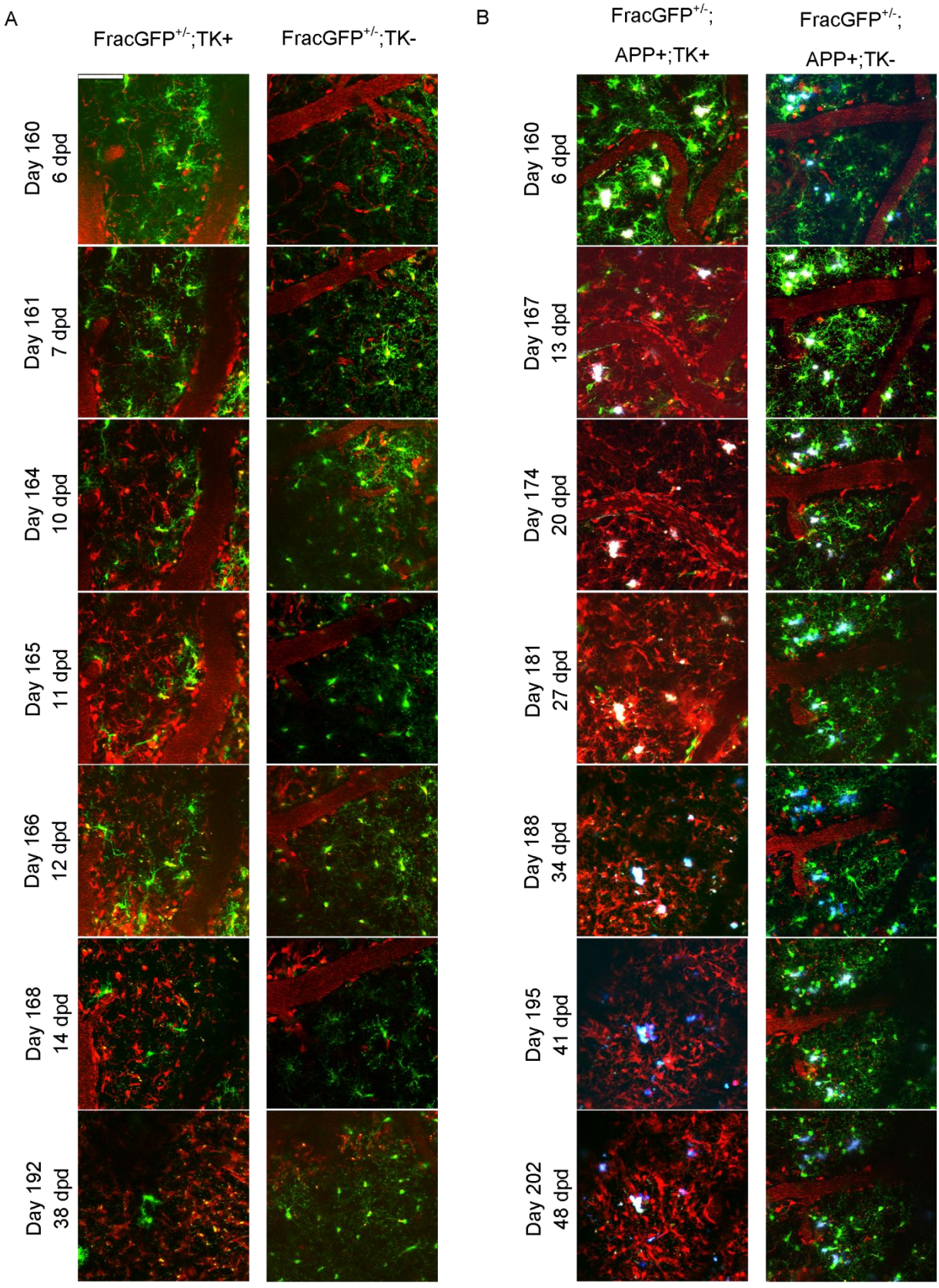

Figure 20: *In vivo* imaging of the replacement of endogenous microglia by peripherally-derived myeloid cells in AD-like mouse brains. Representative maximum intensity projections from the first time point of two-photon imaging movies in FracGFP$^{+/-}$;TK+ and - mice in the healthy (A) and AD-like (B)

context. The blood landmarks and Methoxy-X04 labeled plaques in (B) demonstrate the precise recovery of the imaging positions over time. Scale 100µm, dpd = days post depletion.

In TK- controls, where no depletion of resident microglia occurred, only rarely peripheral cells were found in the brain (Figure 20A, B). In addition, peripherally-derived myeloid cells in TK- mice did not look “microglia-like” but were mostly roundish cells migrating fast through the tissue which was true for both the AD and non-AD context (see Figure 13A).

5.3.2 Peripherally-derived myeloid cell somata are overall smaller and slower in the Alzheimer-diseased context

To characterize peripherally-derived cells in the healthy and AD context upon the long-term GCV treatment paradigm, firstly soma values were analyzed at day six and seven dpd in healthy control animals (APP-negative; APP-) for TK+ peripherally-derived myeloid and TK- endogenous microglial cells. Furthermore, TK+ endogenous microglia were included in the analysis to characterize cells undergoing GCV-mediated cell death. Figure 21A depicts that in long-term GCV-treated FracGFP$^{+/-}$;APP-;TK+ (termed FracGFP$^{+/-}$;TK+) mice peripherally-derived myeloid cells were faster than endogenous microglia (at day six and seven after depletion) as detected in the first thesis aim for healthy animals, where GCV treatment was stopped after 10 days (see Figure 13B; endogenous TK+: 12.64 ± 3.7 nm/s; endogenous TK-: 10.91 ± 4.42; peripheral: 21.36 ± 10.4 nm/s). For soma sphericity no differences were detected between the various experimental conditions (Figure 21B; endogenous TK+: 0.90 ± 0.03; endogenous TK-: 0.83 ± 0.10; peripheral: 0.89 ± 0.06). However, as described before, an increased soma size of TK+ endogenous microglia was detected at day six and seven dpd in non-AD brains, which can be explained by the activation of these cells in the course of GCV-mediated cell death (endogenous TK+: 2043 ± 639.9 µm^3; endogenous TK-: 1012.8 ± 321.2 µm^3; peripheral: 839.1 ± 476.5 µm^3; Figure 21C).

In the AD context, long-term soma movement was measured over seven weeks in FracGFP$^{+/-}$;APP+;TK+ or - mice. Here, the first imaging time point from weekly imaging sessions was registered to correct for translational imaging drifts and somata were tracked over 48 days. Even though peripherally-derived cells showed a trend towards faster soma movement in the amyloid loaded brain (7.53 ± 2.42 µm/week), the difference to endogenous microglia was not significant (4.96 ± 2.44 µm/week; Figure 21D).

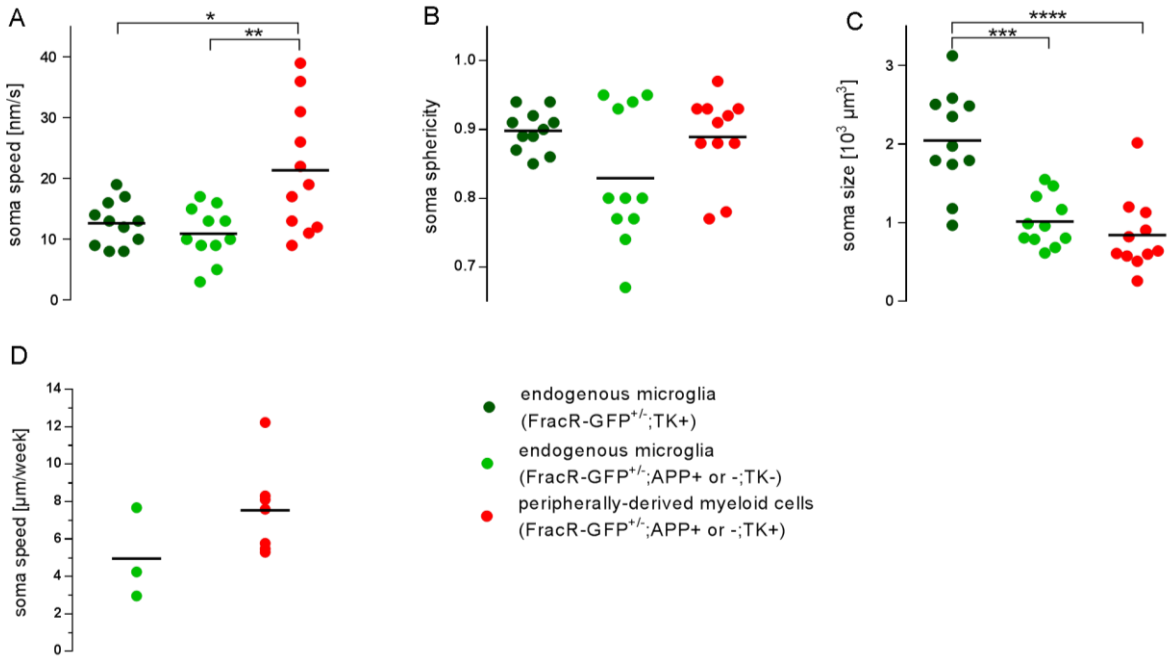

Figure 21: Peripherally-derived myeloid cells have smaller somata that move faster in wildtype brains at early time points after microglial depletion, but show an equal soma speed in the AD brain over 48 days. (A) Soma speed of peripherally-derived myeloid cells in the healthy non-AD brain. (B) Soma sphericity in healthy brains at six and seven dpd. (C) Soma size in healthy brains at six and seven days in the CNS. (D) Soma speeds in AD-like mouse brains, tracked over 48 days. (A-C) One dot incorporates an average of >6 cells from two animals per genotype, 3 ROI per animal. (D): One dot represents all somata from one ROI with 3 ROI per animal tracked over 48 days. Statistics: 1-way ANOVA (A, B, C), Mann-Whitney test (D)

Next, we analyzed soma parameters of peripherally-derived myeloid cells and resident microglia in non-AD versus AD-like brains for all recorded time points. In brains exhibiting AD-like changes, we furthermore discriminated myeloid cells which were in direct proximity to amyloid plaques, thus touching the amyloid deposit with the soma or their processes as well as cells that were more distant to plaques.

Soma speed of peripherally-derived myeloid cells, recorded over 30 minutes, decreased, while soma size increased over time in the brain parenchyma (Figure 22A). Thus, in healthy APP- control brains, the freshly invading cells evolved with respect to their morphology and appearance during the time being exposed to the CNS environment. However, a time-dependent change of soma speed, soma sphericity or soma size of peripherally-derived myeloid cells was not detected in brains of AD-like animals, regardless of their distance to amyloid (Figure 22A).

When analyzing soma speed independent of time in the CNS tissue, there were no changes of endogenous microglia in the healthy brain when compared to microglia in the vicinity of or further away from amyloid plaques (Figure 22B; non-AD: 10.41 ± 3.61

nm/s plaque proximity: 10.46 ± 4.76 nm/s plaque distance: 9.07 ± 4.09 nm/s). Thus, subtle soma movements of endogenous microglia appeared to be not impaired by amyloid deposits. On the other hand, somata of peripherally-derived myeloid cells in the AD-like brain moved significantly slower compared to healthy controls. In addition, somata of peripheral myeloid cells in a wildtype CNS environment as well as peripheral myeloid cells that were more distant to amyloid plaques, were significantly faster compared to their endogenous resident counterparts. Peripherally-derived myeloid cells in direct proximity to a plaque displayed a similar soma speed as endogenous cells touching a plaque (Figure 22B; peripheral; non-AD: 15.6 ± 8.44 nm/s plaque proximity: 10.48 ± 4.12 nm/s plaque distance: 11.03 ± 4.92 nm/s) indicating that the CNS-invading myeloid cells were faster than their endogenous counterparts, but seemed to be functionally impaired in the vicinity of amyloid deposits.

Furthermore, soma sphericity of resident microglia in direct plaque vicinity was reduced when compared to microglia being distant to amyloid plaques (Figure 22C; endogenous; non-AD: 0.88 ± 0.07 plaque proximity: 0.86 ± 0.05 plaque distance: 0.90 ± 0.04). This may be explained by the fact, that soma touching a plaque wind around it, polarize towards the deposit and are thus not as spherical. When examining peripherally-derived myeloid cells, no differences between cells in a non-AD or AD CNS environment were detected. Peripherally-derived myeloid cells close to plaques were more spherical than their endogenous counterparts (Figure 22C; peripheral; non-AD: 0.91 ± 0.04 plaque proximity: 0.91 ± 0.04 plaque distance: 0.90 ± 0.03). This could be due to their greater distance to amyloid deposits (see Figure 27B) and thus their lack of polarization towards Aβ plaques.

The somata of peripherally-derived myeloid cells were overall smaller compared to those of endogenous microglia both in AD and non-AD brains (Figure 22D; peripheral non-AD: 986.3 ± 449.9 µm3 plaque proximity: 924.6 ± 423.3 µm3 plaque distance: 725.6 ± 300.0 µm3; endogenous non-AD: 1309.0 ± 520.4 µm3 plaque proximity: 1387.7 ± 748.7 µm3 plaque distance: 1201.0 ± 682.5 µm3). In contrast to soma sphericity, no differences in soma size were detected between cells close to amyloid plaques and cells further away from them (Figure 22D).

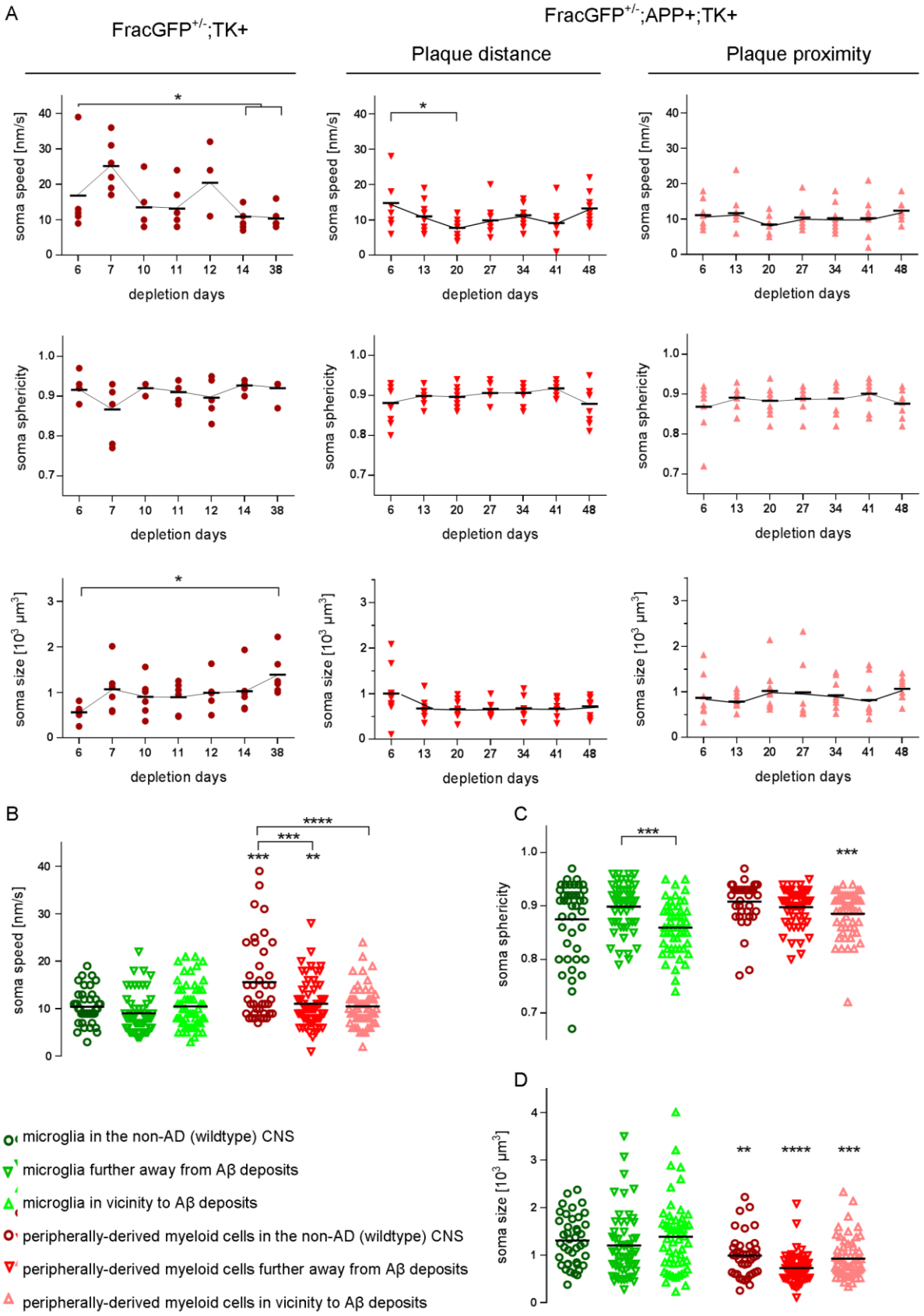

Figure 22: Peripherally-derived myeloid cell somata are overall smaller and slower in brains with AD-like pathology. (A) Soma speed, sphericity and size of peripherally-derived myeloid cells over time in the non-AD (wildtype) and AD-like CNS. (B-D) Soma parameters of peripherally-derived myeloid cells and

resident microglia analyzed over all time points. (B) Soma speed, (C) soma sphericity, (D) soma size. One dot incorporates the average of >6 microglia from 3 (APP-, wildtype) or 6 (APP+) animals or > 7 peripherally-derived myeloid cells from 5 animals; 3 ROI per animal. Statistics: Counterpart comparisons between microglia and peripherally-derived myeloid cells: Mann-Whitney test (denoted as asterisk over the peripheral population), comparisons in the endogenous or peripheral population between conditions: 1-way ANOVA.

In summary, cell somata of long-term GCV treated resident microglia in wildtype mouse brains are as fast as their cellular counterparts of wildtype brains, where GCV treatment had been stopped, as shown in first part of this thesis. Furthermore, the speed of cell somata of myeloid cells repopulating the brain after endogenous microglia depletion seems reduced when being in direct contact to amyloid deposits. Peripherally-derived myeloid cells have overall smaller soma sizes than endogenous microglia, while their somata move faster when being not in close contact to amyloid deposits. In addition, while peripherally-derived myeloid cells adapte to their environment by decreasing the speed of soma movement and increasing soma size in the non-AD (wildtype) CNS environment, soma parameters of myeloid cells in the AD-like mouse brain do not change substantially over a period of 48 days analyzed in this thesis.

5.3.3 Peripherally-derived myeloid cells have a smaller and less ramified process tree independent of amyloid plaque vicinity

Next, we wanted to characterize peripherally-derived myeloid cells and endogenous microglia in the long-term GCV treatment setup in healthy and AD brains by assessing the arborization of their processes. Processes of peripherally-derived myeloid cells were analyzed independently for each imaged time point and plotted over time (Figure 23A). A slight, but not significant, increase in the number of branch points per cell and the sum of process lengths was visible in peripherally-derived myeloid cells residing 38 days in the non-AD CNS as well as for peripherally-derived myeloid cells residing 48 days in the AD-like brain. Thus, as already concluded for peripherally-derived myeloid cells studied in the first project aim, the repopulating myeloid cells, which normally do not harbor processes, adapted a microglial-like morphology very quickly upon entering the brain. Furthermore, their morphology by and large did not change over up to 48 days.

When analyzing branch points per endogenous microglial cell independent from time, a significant reduction of ramification was detected for microglia being in plaque proximity compared to microglia being further away from amyloid deposits. As known from the

literature, microglia have an altered morphology next to Aβ plaques and thus it is not unsurprising that the process tree of these cells is smaller and less branched, giving a more “amoeboid” appearance in the vicinity of amyloid deposits. Process tree branching of peripherally-derived myeloid cells was overall reduced when compared to endogenous microglia in the healthy and AD-like brain (Figure 23B; endogenous non-AD: 27 ± 13 plaque proximity: 20 ± 13 plaque distance: 34 ± 18; peripheral non-AD: 15 ± 9 plaque proximity: 10 ± 6 plaque distance: 15 ± 8). Likewise, the sum of the lengths of all processes per cell was significantly lower in peripherally-derived myeloid cells compared to endogenous microglia in the healthy and in the AD context. Similarly, as seen for the ramification branching points, the sum of the process lengths of endogenous microglia next to amyloid plaques was decreased in comparison to microglia being further away from deposits, possibly due to their “amoeboid” morphology exhibiting shorter, less branched processes (Figure 23C; endogenous non-AD: 539.9 ± 251.2 µm plaque proximity: 342.6 ± 238.8 µm plaque distance: 629.0 ± 282.4 µm; peripheral non-AD: 221.5 ± 126.1 µm plaque proximity: 143.2 ± 75.8 µm plaque distance: 212.9 ± 112.2 µm). Notably, peripherally-derived myeloid cells showed no difference in terms of ramification and process length as a function of their distance to amyloid plaques, most likely because the process tree of these new myeloid cells in the brain was too small to be further decreased. The fact that peripherally-derived myeloid cells were per se not in close contact to amyloid deposits (Figure 27B) speaks in favor that peripherally-derived myeloid cells were not actively recruited to Aβ plaques.

The reduced size and ramification of the process tree of peripherally-derived myeloid cells was not due to a reduced number of filaments originating from the soma, as measured by the number of primary filaments per cell, but can be ascribed to a more distal branching point at the process arbor (endogenous non-AD: 4 ± 2 plaque proximity: 4 ± 2 plaque distance: 4 ± 1; peripheral non-AD: 4 ± 1 plaque proximity: 4 ± 2 plaque distance: 4 ± 1; Figure 23D).

In summary peripherally-derived myeloid cells adapt a microglial-like process morphology, including the development of processes, as soon as they enter the brain. The amount of primary filaments, and thus the foundation of the process arbor, does not differ between peripherally-derived myeloid cells and resident microglia in the non-AD and AD brain. Nevertheless, peripheral myeloid cells have shorter and less branched

processes over a time period of up to 48 days in the CNS tissue when compared to microglia.

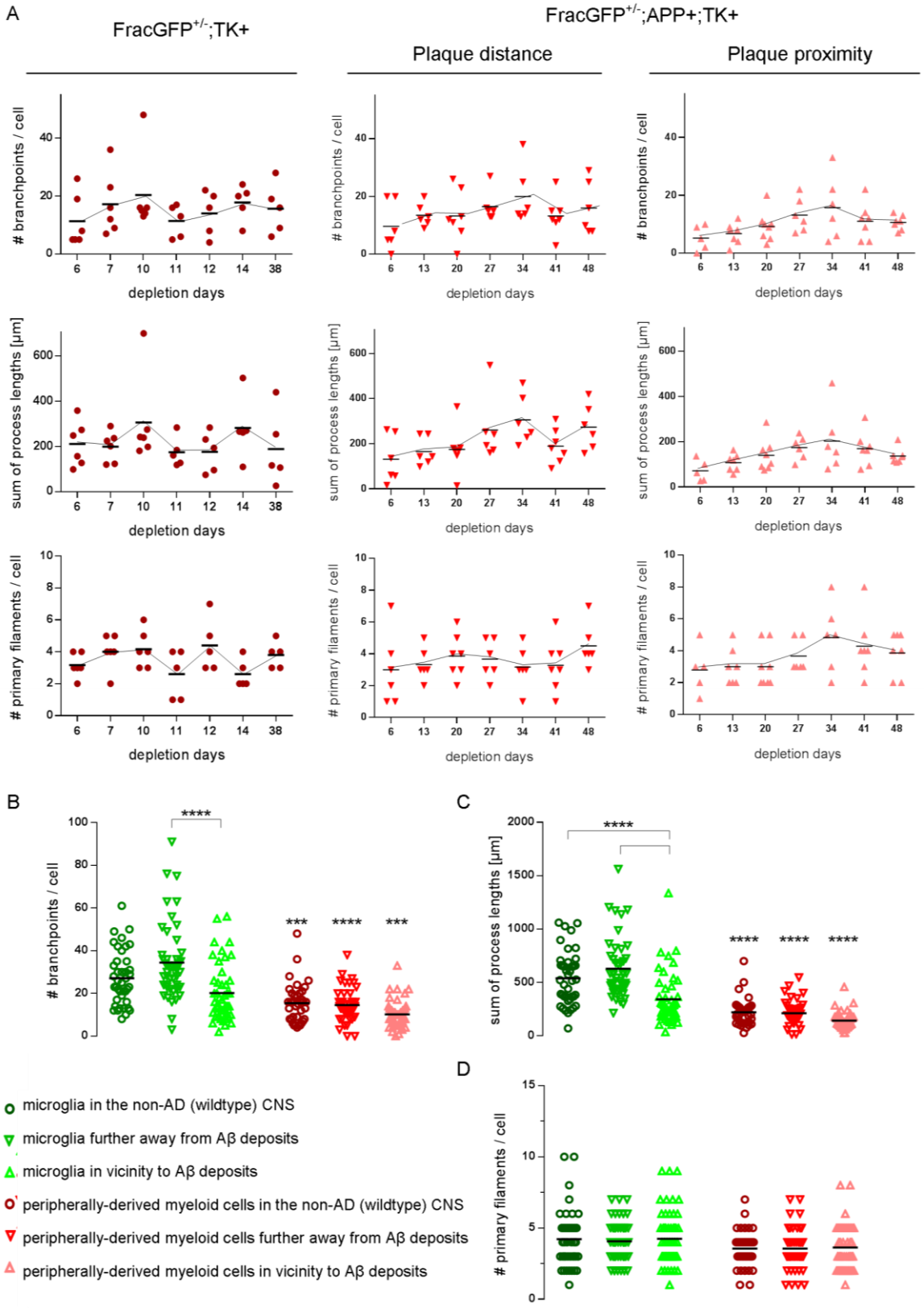

Figure 23: Peripherally-derived myeloid cells have smaller and less ramified processes independent of amyloid plaque vicinity. (A) Process branch points, sum of process lengths and

primary filaments per cell, i.e. processes originating from the soma, of peripherally-derived myeloid cells over time in the non-AD (wildtype) and AD-like CNS. (B-D) Process parameters of peripherally-derived myeloid cells and resident microglia analyzed over all time points. (B) Process branch points per cell, (C) sum of process lengths per cell, (D) primary filaments per cell, i.e. processes originating from the soma. One dot represents one cell from 6 (APP-, wildtype) or 4 (APP+) animals; 3 ROI per animal. Statistics: 1-way ANOVA, significance between endogenous microglia and their peripherally-derived counterparts is denoted as asterisk over the peripheral population.

Additionally, while resident microglia display an altered morphology with shorter, less branched bifurcations, the morphology of peripherally-derived myeloid cells is not influenced by the vicinity to Aβ, at least for the herein investigated parameters.

5.3.4 Process movements of peripherally-derived myeloid cells and microglia are reduced in the Alzheimer-diseased brain

Next, we wanted to test if peripherally-derived myeloid cell processes act normally in the AD brain. As described, endogenous microglia continuously scan the brain environment for pathogens by extending and retracting their processes. Thus, we quantified retractions and extensions of peripherally-derived myeloid cells as well as endogenous microglia after 10 dpd in the non-AD and after 13 dpd in the AD-like brain, incorporating all imaged time points. As before, we separately analyzed cells in close proximity as well as being more distant to Aβ plaques in brains of APP+ animals. We found that subtle process movements did not change substantially in the healthy and AD-like brain up to 48 days in the tissue, irrespective of the distance to Aβ plaques in the latter (Figure 24A).

When pooling process extensions of all analyzed time points, peripherally-derived myeloid cells in the healthy brain showed faster process movements (1.10 ± 0.41 µm/min) compared to their endogenous cellular counterparts (0.86 ± 0.28 µm/min; Figure 24B). In the AD-like brain, peripherally-derived myeloid cells and endogenous microglia showed no differences with respect to the extension speed of their processes (plaque distance: peripheral 0.96 ± 0.42 µm/min, endogenous 0.84 ± 0.29 µm/min; proximal: peripheral 0.62 ± 0.25 µm/min, endogenous 0.65 ± 0.25 µm/min; Figure 24B). Nevertheless, amyloid deposits had a marked influence on process extensions, as they significantly reduced process extension speeds of peripherally-derived myeloid cells as well as of endogenous microglia in proximity to amyloid plaques (Figure 24B). Similarly, process retraction speeds of peripheral myeloid cells and microglia were significantly slowed in the vicinity of amyloid deposits (non-AD: peripheral 0.96 ± 0.34 µm/min, endogenous 0.90 ± 0.33 µm/min; plaque distance: peripheral 0.87 ± 0.34 µm/min,

endogenous 0.84 ± 0.30 µm/min; proximal: peripheral 0.61 ± 0.24 µm/min, endogenous 0.63 ± 0.26 µm/min; Figure 24C).

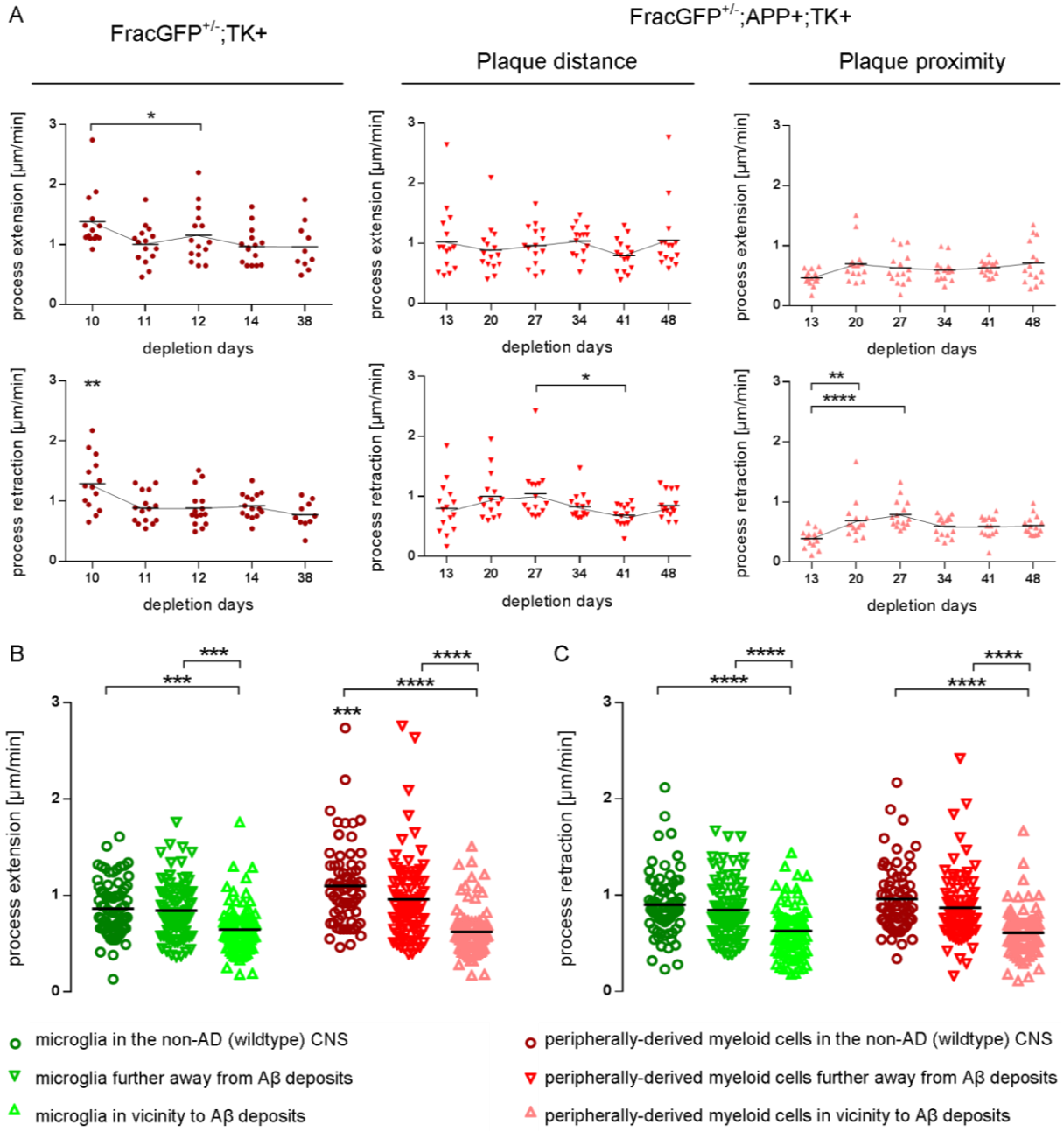

Figure 24: Peripherally-derived myeloid cells are able to extend and retract their processes alike resident microglia and are similarly paralyzed in the vicinity of Aβ. Baseline movements of cell processes measured over five minutes. (A) Peripherally-derived myeloid cell process extension and retraction speeds over time. (B, C) Process speeds of peripherally-derived myeloid cells and endogenous microglia analyzed over all time points for (B) extensions and (C) retractions. Statistics: 1-way ANOVA; Differences between peripherally-derived myeloid cells and microglia are denoted as asterisk over the peripheral cell population. One dot represents one process speed from 3 ROI per time point , 3 animals per genotype.

Thus, peripherally-derived myeloid cells appear to be sufficiently equipped to scan the brain environment by extending and retracting their processes in the healthy and in the

AD-like brain. However, being in close vicinity to amyloid deposits, peripherally-derived myeloid cell movements were reduced to the same extent as microglia cells are.

Next, we wanted to quantify the site-directed motility of peripherally-derived myeloid and of endogenous microglia cell processes towards a laser-induced lesion in the proximity to Aβ plaques and compare this motility to results from the healthy brain, as shown in Figure 17. Therefore, laser lesions were performed in APP+ animals upon depletion of microglia followed by the repopulation of peripherally-derived myeloid cells. As visible in Figure 25A, resident microglia in AD-like brains were markedly impaired in their reaction towards a laser-induced lesion.

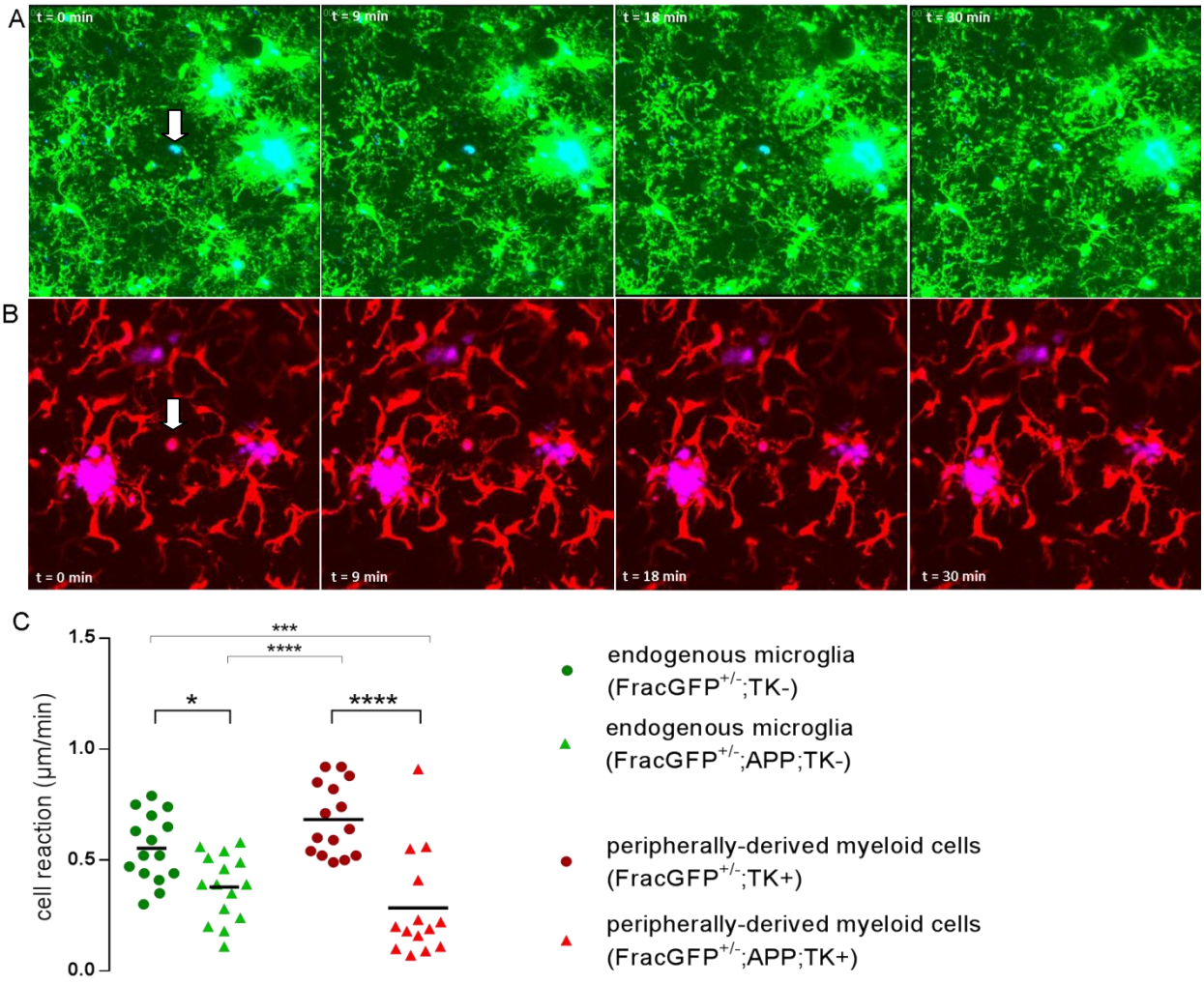

Figure 25: More rapid reactivity of peripherally-derived myeloid cells towards a laser-induced lesion is paralyzed in the Alzheimer-diseased brain. Representative maximum intensity projections from indicated time points of two-photon imaging in the AD-like brain. (A, B) Process extension towards a laser-induced tissue lesion (highlighted by an arrow) of microglia (A) and peripherally-derived myeloid cells (B) in the AD-like brain. (C) Quantification of site-directed process motility. One dot represents one laser lesion from n = 5 animals per genotype; images for APP- animals are visible in Figure 17A and B, data points from APP- animals in (C) are the same as depicted in Figure 17C. Statistics: 1-way ANOVA.

While resident microglia were able to project and extend their processes to a laser lesion in the healthy brain and “sealing” the tissue injury shortly after 30 minutes (as shown in Figure 17A), there was a markedly impaired reaction detectable in the Aβ-carrying brain. Similarly, peripherally-derived myeloid cells in the healthy brain “sealed” the lesion with their processes in around 30 minutes (as shown in Figure 17B), while in the AD-like brain this site-directed reaction was similarly impaired and not complete after 30 minutes (Figure 25B). Surprisingly, while in the non-AD (wildtype) brain peripherally-derived myeloid cells had significantly faster process movements towards the lesion when compared to resident microglia (Figure 17C), in the AD-like brain this difference was not detectable any longer (Figure 25C). The quantification of these cell reactions showed that alike endogenous microglia also peripherally-derived myeloid cells exhibit markedly impaired process movements when entering the Aβ-containing AD-like brain (Figure 25C).

5.3.5 Peripherally-derived myeloid cells are more numerous and are more densely distributed in the cortex, but do not cluster around amyloid deposits

As the stereological analysis revealed that more Iba1+ cells were found in repopulated brains (Figure 19B, C), we aimed to analyze the distribution of peripherally-derived myeloid cells in the tissue. For this purpose, the distances between xyz coordinates of somata of endogenous microglia as well as peripherally-derived myeloid cells were measured. The number of peripherally-derived myeloid cells repopulating microglia-depleted brains increased in a time-dependent fashion in the cortex, but became stable at 38 days in non-AD brains and at 48 days in the brain of APP+ animals (Figure 26A). This underlines that the repopulation of the brain by peripherally-derived myeloid cells after microglial depletion is a rapid and robust process. On the other hand, peripherally-derived cells in the non-depleted brain, that may infiltrate into the CNS presumably through a leaky BBB, were less numerous and did not increase over time in the AD-like brain (Figure 26A).

Furthermore, we found that peripherally-derived myeloid cells were in closer vicinity to each other compared to the cell-to-cell distances of endogenous microglia in the wildtype and amyloid loaded CNS environment (Figure 26B). As the processes of peripherally-derived myeloid cells were shorter, the cells needed to close ranks in order

to be capable to surveil the entire brain tissue with their protrusions. Indeed, while ~5100 endogenous microglia were present in 1 mm^3 of cortex in the non-AD brain, >11000 peripherally-derived myeloid cells were present in the same volume of CNS tissue (Figure 26C).

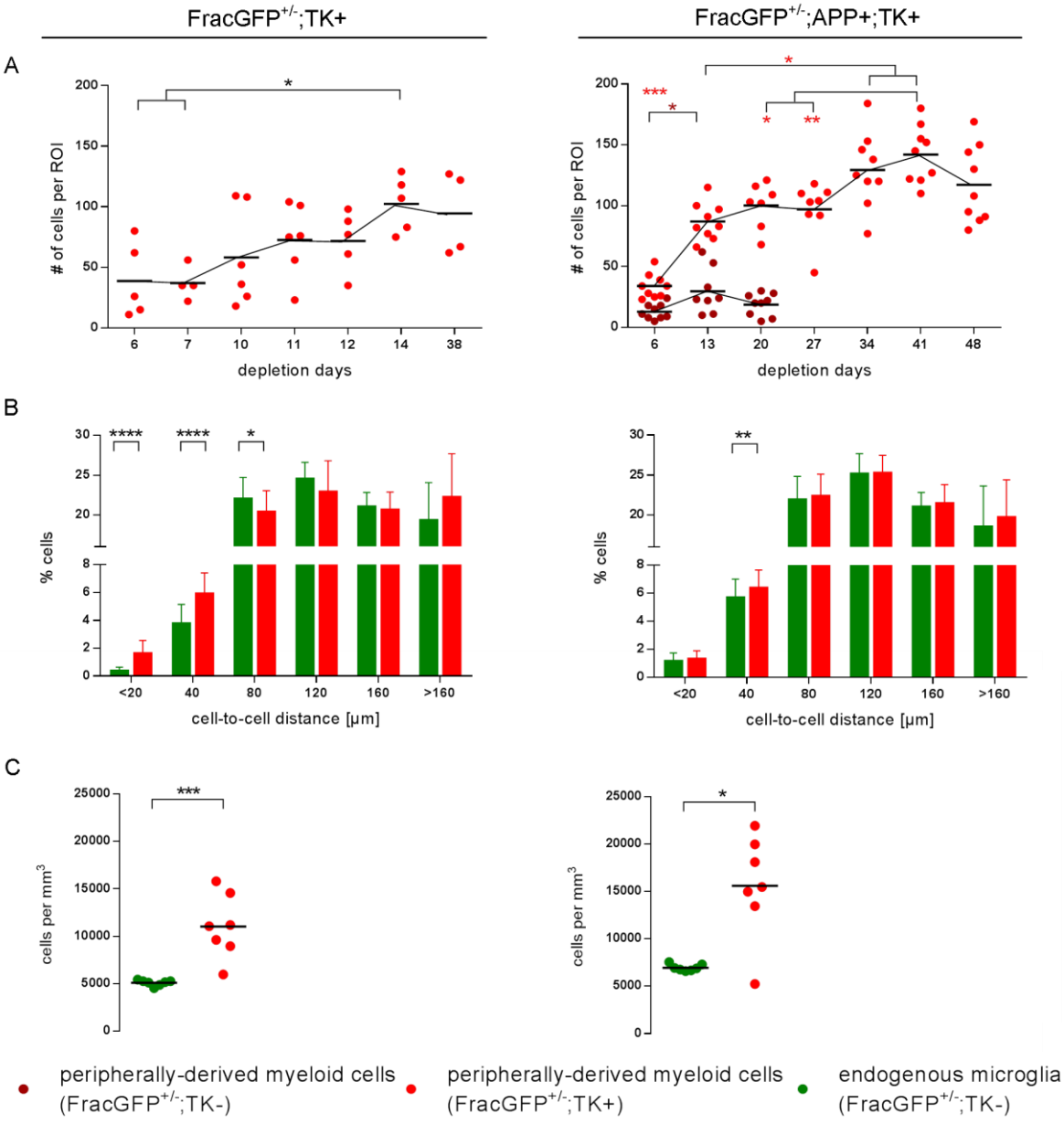

Figure 26: Peripherally-derived myeloid cells built up denser networks compared to resident microglia. (A) Peripherally-derived cell numbers in microglia depleted healthy (FracGFP$^{+/-}$;TK+) and AD-like (FracGFP$^{+/-}$;APP+;TK+) brains plotted over time (color coded significances in the APP+ animals relate to TK+ peripherally-derived cells). (B) Percentage of peripherally-derived myeloid cells and microglia in set cell-to-cell distance radii. (C) Cell numbers per mm^3 of brain parenchyma. One dot incorporates the average value of one ROI, 6 (APP- wildtype) or 4 (APP+) animals with 3 ROI per animal. Statistics: 1-way ANOVA (A), Mann-Whitney test (B, C); asterisks over one condition indicate significant differences to all other conditions.

These differences were very similar for APP+ brains; here ~6800 resident microglia versus 15000 peripherally-derived myeloid cells were detectable in 1 mm^3 of CNS tissue (Figure 26C). Notably, cell numbers of endogenous as well as of peripherally-derived myeloid cells per mm^3 were elevated by >30% in AD brains.

Next, we evaluated whether brain-repopulating myeloid cells were recruited to amyloid plaques. After microglial depletion, the cell number of peripherally-derived myeloid cells increased next to amyloid deposits over time (Figure 27A). This was only detectable in microglia-depleted brains, as in TK- brains, where no microglia depletion occurs, the very few invading peripheral myeloid cells did not increase in numbers (Figure 27A). Surprisingly, when analyzing the distance of endogenous cells and of peripherally-derived myeloid cells to amyloid deposits, peripherally-derived myeloid cells were not actively clustering around Aβ plaques, as only few peripherally-derived myeloid cells were found in 10 µm or 20 µm distance to amyloid plaques (Figure 27B).

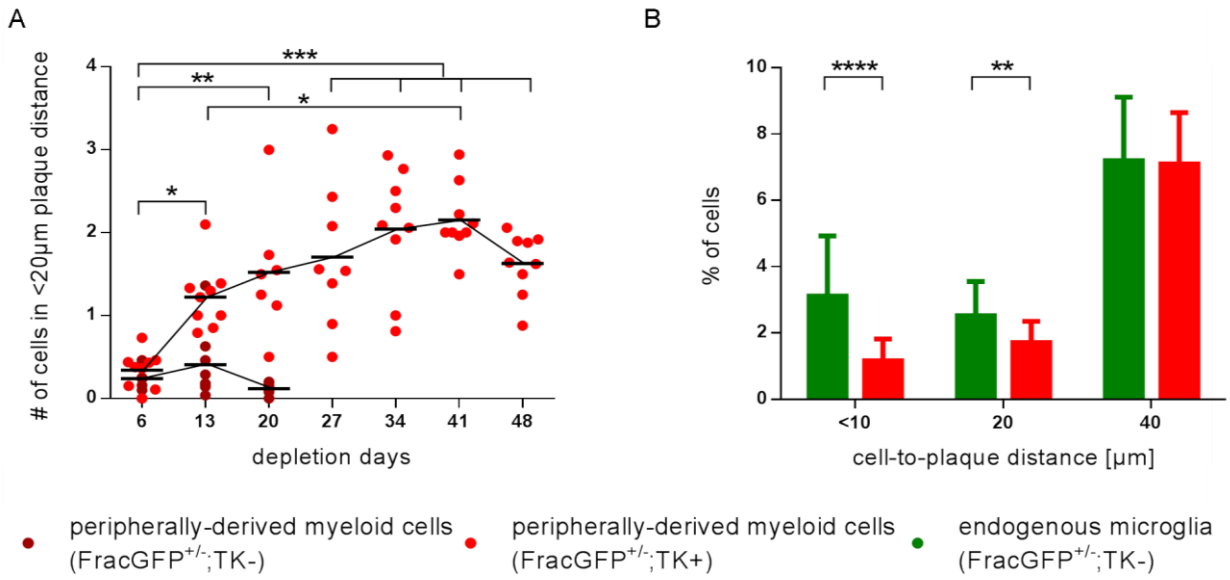

Figure 27: Peripherally-derived myeloid cells do not cluster around amyloid plaques. (A) Peripherally-derived myeloid cell numbers in distances <20µm to amyloid plaques plotted over time. (B) Percentage of cells in set cell-to-plaque distance radii. (A) One dot incorporates the average value of one ROI; (B) means of all analyzed ROI; (A, B) ROI from 6 (APP- wildtype), 4-5 (APP+) animals; 3 ROI per animal. Statistics: (A) 1-way ANOVA, (B) 2-way ANOVA.

Altogether we could show with this study that brains harboring peripherally-derived myeloid cells upon long-term GCV treatment show a trend towards amyloid plaque reduction. Peripherally-derived myeloid cells quickly adapt microglia-like morphology in the microglia-depleted brain and cover the entire parenchyma in a rapid and robust fashion within the first two weeks after microglia depletion. These new cells show no

major evolvement in their process tree morphology up to 48 days in the healthy and in the AD-like brain. On the other hand, somata of peripherally-derived myeloid cells move slower and are larger until day 38 in the healthy brain. In the AD-like brain, no time-dependent changes in soma parameters are detectable. The analyzed cell populations show no major differences in soma shape and in their composition of the arborization of their processes. However, peripherally-derived myeloid cells have smaller somata that move faster, exhibite a shorter and less branched process tree, which close ranks to each other in the brain parenchyma.

The results of the first project aim showed that the newly invading cells are able to scan and surveil the brain tissue by continuously extending and retracting their processes similar to resident microglia; they appear to be even more active than resident microglia when quantifying their site-directed motility in response to a laser-induced lesion. In the AD context, on the other hand, subtle soma movements, baseline process extensions and retractions as well as the reaction towards a laser lesion are found to be impaired in the vicinity of amyloid plaques. Additionally, these newly recruited cells are more distant from amyloid plaques when compared to endogenous microglia. Thus, even if these peripherally-derived myeloid cells have the potential to be more active and to be better amyloid combaters, they seem to be functionally impaired by the AD microenvironment and ae not recruited to amyloid plaques.

5.4 Project Aim 3: Phenotypic modulation of endogenous microglia by NALP3 inflammasome inhibition as therapeutic strategy for Alzheimer's disease

As recruitment of peripherally-derived myeloid cells may have the potential to fight amyloid burden, but – apparently, as shown in the project aim 1 and 2 - is not sufficient, we focused on the manipulation of endogenous microglia in the AD-like brain to modulate their impaired phenotype in order to increase their ability to clear amyloid deposits.

Inflammasomes are multimolecular protein complexes in myeloid cells that sense infectious agents, as well as host-derived danger signals as part of the innate immune system (Figure 5, [128]). The inflammasome subtype NALP3 was recently shown to be activated by Aβ [129]. Genetic deletion of NALP3 in an AD mouse model resulted in increased microglial phagocytosis, an increased expression of IDE and thus, a marked

reduction in cerebral amyloid deposits as well as improved cognitive function [127]. Therapeutic targeting of NALP3 therefore appears to be a very promising approach to fight AD pathology, while at the time of initiating the herein described experiments no NALP3-specific inhibitor was known or published.

5.4.1 Ebselen as safe selenium-derivate is a specific NALP3 inhibitor

Our collaborator Prof. Veit Hornung (University of Bonn) identified the selenium-derivate Ebselen (Figure 28A) as specific inhibitor of the NALP3 inflammasome (personal communication). Before testing this compound as potential therapeutic drug interfering with AD pathology *in vivo* in APPPS1 mice, we first ensured *in vitro* that Ebselen is non-toxic and indeed inhibits the inflammasome in myeloid cells. Thus, we first tested Ebselen *in vitro* at different concentrations with respect to its potential to reduce IL-1β, a protein mainly secreted after NALP3 inflammasome activation. We activated the inflammasome in cultured peritoneal macrophages by administration of LPS for 24 h, followed by the addition of ATP for 30 min. Ebselen was dissolved in DMSO at a concentration of 0.5 mM, further diluted in cell culture medium and supplied together with LPS. Supernatants were analyzed by Elisa. Already 50 µM Ebselen were found to block IL-1β secretion, while TNFα, a NALP3 independent protein, remained unchanged (Figure 28B).

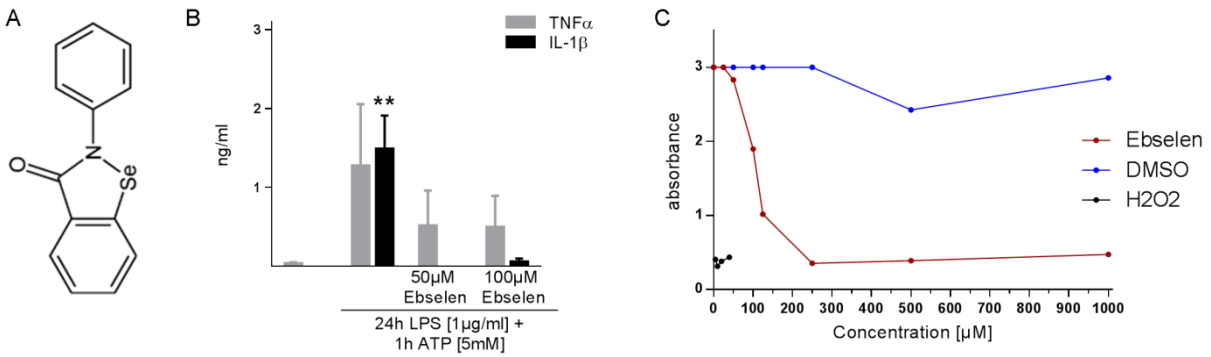

Figure 28: Ebselen significantly reduces IL-1ß in cultured peritoneal macrophages and is non-toxic up to 100µM. (A) Chemical structure of the selenium derivate Ebselen, adapted from [72]. (B) Concentration of IL-1β and TNFα secreted by stimulated peritoneal macrophages (N = 3 with three technical replicates). (C) WST-1 viability assay of peritoneal macrophages correlating cell death to a decrease in absorbance. Hydrogen peroxide served as positive control (N=1 with two technical replicates). Statistics: 1-way ANOVA (B).

Lastly, we performed an *in vitro* viability assay over 24 hours in peritoneal macrophages derived from wildtype mice to test the toxicity of Ebselen. Here, we used different Ebselen concentrations or only the DMSO vehicle. Hydrogenperoxide (H_2O_2) served as

positive control to reduce cell viability. Absorbance of the WST-1 reagent was used to assess cell viability. Ebselen was shown to be tolerated up to a concentration of 100 µM, while a concentration of 50 µM Ebselen turned out to be the preferred concentration for all *in vitro* experiments (Figure 28C).

5.4.2 Cytokines induced by NALP3 inflammasome activation are elevated in APPPS1 mice

As mentioned in the introduction, the NALP3 inflammasome was shown to be activated *in vitro* by Aβ in AD patients as well as in an AD mouse model [127, 129]. To quantify NALP3 inflammasome activation in the APPPS1 AD mouse model used herein, we analyzed brain tissue at different ages. CD11b+ microglia were isolated and tested for gene expression of different inflammasome components. Furthermore, brain tissue homogenates were generated using RIPA buffer to measure IL-1β and IL-18 levels, the main cytokines secreted upon NALP3 inflammasome activation. APPPS1 mice exhibit not yet plaque pathology at the age of 30 days (Figure 29A, adapted from [136]) and subsequently the pro-inflammatory response of activated microglia clustering around amyloid deposits is not developed. Hence, neither upregulation of the pro-inflammatory cytokine TNFα nor Iba1, which is increased in activated microglia, could be detected. Likewise, all tested genes that are part of making up the NALP3 inflammasome (these are NALP3, Caspase1 (Casp1), ASC) and the mRNA levels of IL-1β and IL-18, the cytokines induced by NALP3 inflammasome activation, were not elevated (Figure 29D). At the age of 120 days, APPPS1 mice display robust amyloid plaque pathology in the cortex and showed elevated IL-1β gene expression in microglial cells (Figure 29B, E), while whole brain IL-1β and IL-18 protein expression was not elevated (Figure 29G, I). At 250 days of age, where APPPS1 mice present with full blown amyloid pathology, changes in NALP3-relevant genes were not detectable any longer, while whole brain IL-1β protein levels were significantly increased and IL-18 protein was unaltered (Figure 29C, F, H, J). To detect Caspase1 cleavage as yet another marker for NALP3 inflammasome activation, Triton-X fractions from brain homogenates of wildtype mice (at 160 days of age) and 120 or 250 day old APPPS1 mice were probed for p10, which is the cleaved and active form of Caspase1, using Western blotting (Figure 29K, L).

Thus, in the APPPS1 mouse model, amyloid induced NALP3 inflammasome activation is detectable on the genetic level at 120 days of age, while protein changes can only be seen at later stages.

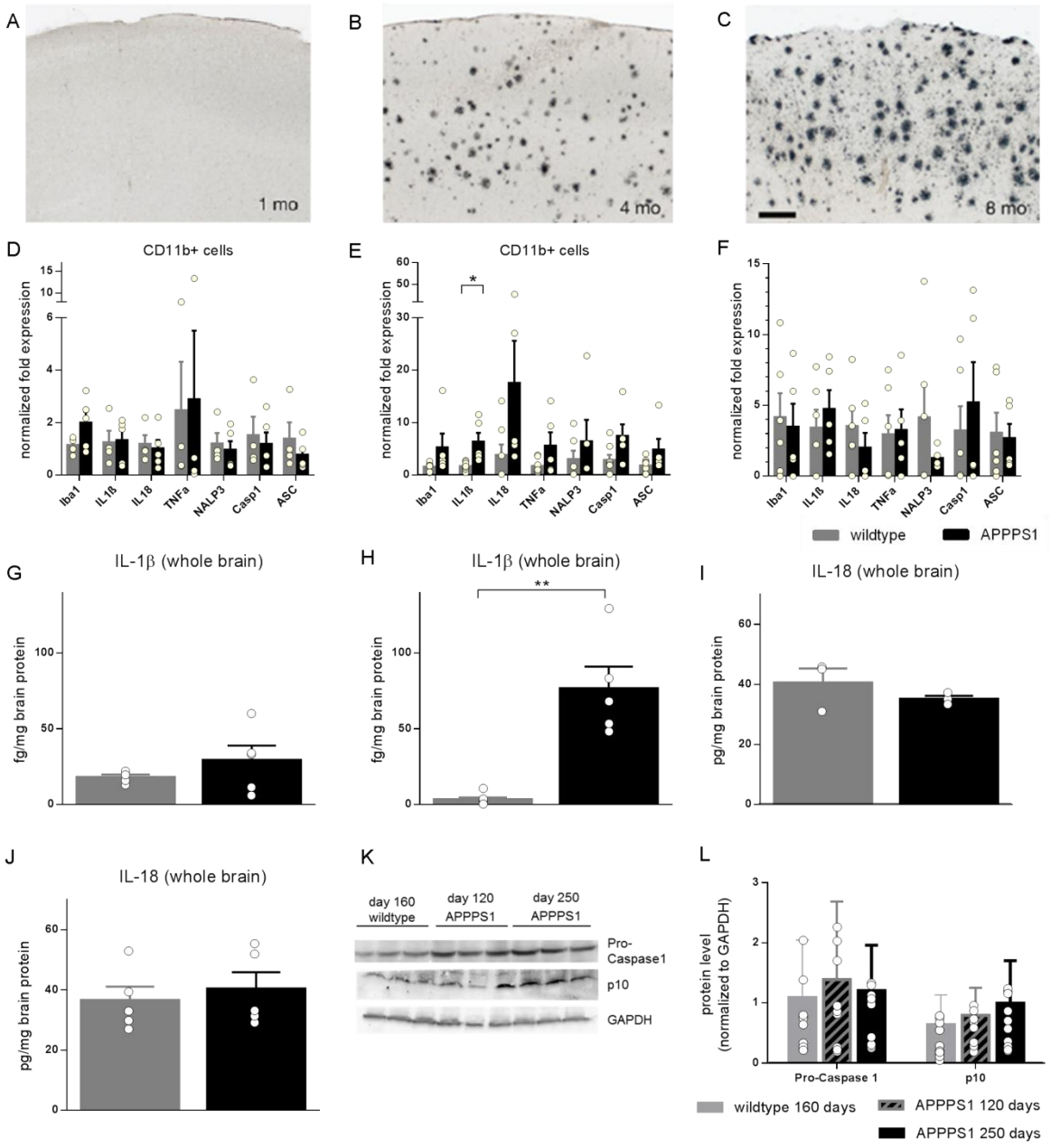

Figure 29: Microglial IL-1β mRNA is elevated in 120 day old APPPS1 mice, while cerebral IL-1β protein levels and active forms of Caspase1 are elevated only at later stages. (A) APPPS1 mice show no plaque pathology at an age of 30 days, with (B) robust amyloid deposition at 120 days and (C) full blown pathology at 250 days of age (Figure adapted from [136]). (D-F) Gene expression of NALP3-related genes in CD11b+ sorted microglia of APPPS1 mice at (D) 30 days, (E) 120 days as well as (F) 250 days of age. (G, H) Whole brain IL-1β protein level of APPPS1 mice aged (G) 120 days or (H) 250 days. (I, J) Whole brain IL-18 protein levels of APPPS1 mice aged (I) 120 days or (J) 250 days. (K) Representative picture of a Caspase1 Western Blot with the respective (L) quantification. Each dot is representing one analyzed animal with (D, E, F) three or (G, H, I, J, L) four technical replicates; Statistics: Mann-Whitney test or (L) 2-way ANOVA.

5.4.3 Intraperitoneal application of Ebselen results in a reduced survival of mice, while not inducing a systemic infection

To interfere with the initiation of amyloid deposition *in vivo*, we started to treat 30 day old APPPS1 mice. For *in vivo* inhibition of the NALP3 inflammasome, Ebselen was dissolved first at a concentration of 0.5 mM in DMSO and further diluted in 25% β-cyclodextran, which served as vehicle. Ebselen was i.p. injected three times weekly at 10 mg/kg, a dose that was shown before to have an effect on the CNS when administered peripherally [151]. For control purposes, the same amount of DMSO was applied upon dissolving it in vehicle. Overall, the DMSO concentration was below 0.5%, an amount that is not considered to be toxic [152]. Similarly, the vehicle concentration used herein has been shown earlier to be tolerated by mice over long treatment periods [153]. Thus, to inhibit the NALP3 inflammasome in AD, APPPS1 mice were left untreated or i.p. injected with Ebselen or vehicle control three times per week starting at 30 days of age until 120 days (Figure 30A). To check various blood parameters and thus systemic Ebselen tolerability in these mice, blood was collected from the facial vein at day 75. Unfortunately, 50% of Ebselen-treated mice died around day 70 (Figure 30B). These animals presented with a indurated and hardened peritoneum and showed signs of mild peritonitis at autopsy. Vehicle-treated mice were healthy and showed no such adverse side-effects. Thus, we stopped both vehicle and Ebselen injections at day 75 and terminated the experiment at day 95, where amyloid pathology is already present in APPPS1 mice. When terminating the experiment, blood and serum was collected and brains were taken for further protein and gene analyses (Figure 30A).

Levels of C-reactive protein (CRP), an indicator for systemic inflammation, in the serum of all Ebselen- or vehicle-treated mice was not elevated (Figure 30C). Likewise, all mice had unaltered weight and various analyzed blood parameters at day 75 (data not shown) and day 95 (Figure 30D, E) as well as kidney (Figure 30F) and liver (Figure 30G) parameters were unaffected, being within the range of age-matched control wildtype mice supplied by Synlab GmbH, irrespective of whether Ebselen-, vehicle- or un-treated mice were analyzed. Thus, we concluded a local peritonitis rather than a severe systemic, i.e. inflammatory, event to be the cause of Ebselen-induced death.

In summary, a systemic infection of Ebselen-treated mice can be excluded after analysis of blood and serum parameters. Mice that died prematurely during the

experiment around day 75 showed signs of a local peritonitis, which was accompanied by an indurated and swollen peritoneum prior to death.

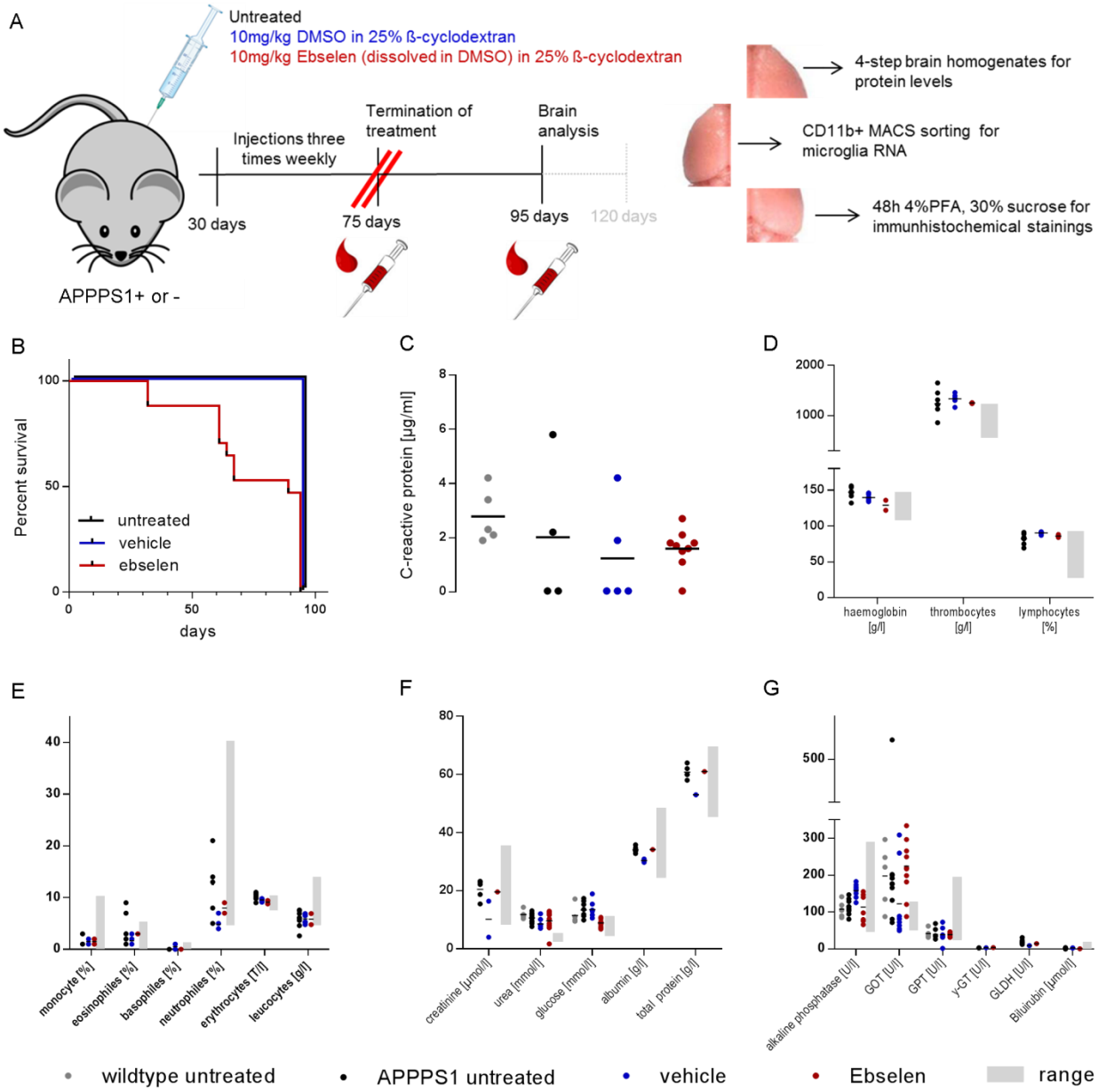

Figure 30: Intraperitoneal application of Ebselen reduced survival of mice, while not inducing a systemic infection. (A, B) Experimental setup and survival curve: APPPS1 or wildtype mice at an age of 30 days were left untreated or were i.p. injected with 10 mg/kg Ebselen (in 25% β-cyclodextran vehicle) or vehicle three times per week for three months. After half of the treatment period, blood was collected to assess potential treatment related side-effects. Over 50% of Ebselen-treated mice died around day 70 (B), which was the reason why the treatment was stopped at day 75 and the experiment was halted at day 95. (C) Serum levels of C-reactive protein (CRP) at day 95. (D, E) Blood, (F) kidney and (G) liver parameters at day 95. Each dot is representing one analyzed animal.

Since all other mice that survived looked healthy and showed no signs of a swollen abdomen, peritonitis, or other systematic changes, we regarded a substantial influence

on CNS parameters as less likely. This is why we decided to analyze all remaining brains for NALP3 inflammasome activation and amyloid pathology.

5.4.4 Microglial IL-1β mRNA levels, but not IL-1β or IL-18 protein levels, are reduced upon Ebselen treatment

First, CD11b+ microglia were extracted from the left hemisphere of mice from various experimental groups in order to analyze gene expression of NALP3 inflammasome-associated genes. Since we found IL-1β gene expression to be decreased in Ebselen-treated microglia compared to vehicle controls, we reasoned that Ebselen inhibited the NALP3 inflammasome in these animals (Figure 31A). Furthermore, NALP3 gene expression was upregulated five fold in Ebselen-treated mice compared to all other analyzed animals, which may present a compensatory mechanism at the gene level to compensate for NALP3 multicomplex-protein inhibition (Figure 31A).

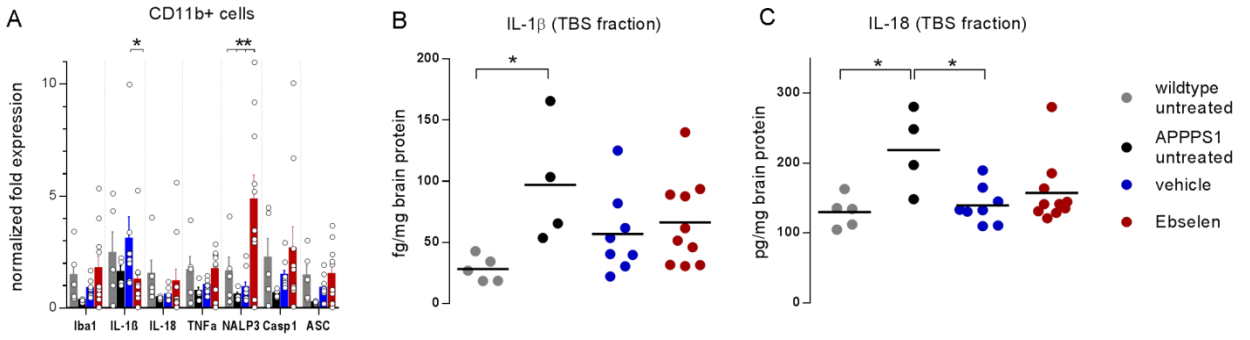

Figure 31: Microglial IL-1β mRNA, but not protein levels are reduced upon Ebselen treatment. (A) IL-1β gene expression in CD11b+ microglia. (B) IL-1β and (C) IL-18 protein levels, measured in the TBS fraction of homogenized brains. Each dot is representing one analyzed animal with (A) three or (B, C) two technical replicates; Statistics: Mann-Whitney test (A), 1-way ANOVA (B, C).

An elevation of IL-1β and IL-18 protein in the brains of APPPS1 mice at day 95 of the treatment could be detected in comparison to wildtype mice (Figure 31B, C). However, Ebselen-treated animals did not show reduced IL-1β or IL-18 protein levels (Figure 31B, C).

5.4.5 Congophilic and diffuse amyloid plaque load is reduced upon intraperitoneal Ebselen treatment

Next, we wanted to analyze if the subtle reduction in microglial IL-1β mRNA expression, without changes in inflammasome-associate protein levels, was sufficient to lessen amyloid plaque burden. Therefore, half of the right hemisphere was cut into 30 µm thick free floating sections and stained with (i) 4G8 antibody, (ii) the luminescent conjugated

oligothiophene pFTAA and (iii) Congo red. These dyes stain amyloid with various predominance for certain types of Aβ. While the antibody 4G8 stains soft and core Aβ plaques, Congo Red has a preference to label core plaques. PFTAA, however, also detects prefibrillar Aβ species [143]. As visible in Figure 32A, D and G, all stainings showed a marked reduction in 95 day old APPPS1 mice that were treated with Ebselen for 45 days, when compared to vehicle-treated and untreated controls.

Stereological analysis showed that 585 ± 167 Congo red-positive plaques per mm^3 occupied 0.28 ± 0.08% of the cortex in Ebselen-treated mice, while 863 ± 136 plaques (0.53 ± 0.16%) in vehicle-treated and 926 ± 75 in untreated mouse brains were visible (0.53 ± 0.11%; Figure 32B, C). PFTAA labeled plaques were likewise significantly reduced in Ebselen-treated mice (untreated: 2046 ± 117, vehicle: 2197 ± 348, Ebselen: 1562 ± 316 plaques/mm^3; Figure 32E). Here, the cortical area covered by amyloid plaques was only reduced when compared to vehicle-treated animals (untreated: 1.16 ± 0.21%, vehicle: 1.27 ± 0.35%, Ebselen: 0.83 ± 0.16%; Figure 32F). For 4G8-positive plaques, the plaque number per mm^3 was strongly reduced for Ebselen-treated mice compared to all control groups (untreated: 1820 ± 112, vehicle: 1411 ± 183, Ebselen: 1126 ± 182; Figure 32G). In addition, vehicle-treated mice showed a significant reduction in 4G8-positive plaques compared to untreated animals. For 4G8-labeled plaques, Ebselen-treated animals also showed a marked reduction in the area covered by amyloid in the cortex when compared to vehicle-treated and untreated animals (untreated: 2.58 ± 0.32%, vehicle: 2.07 ± 0.44%, Ebselen: 1.34 ± 0.39%; Figure 32H).

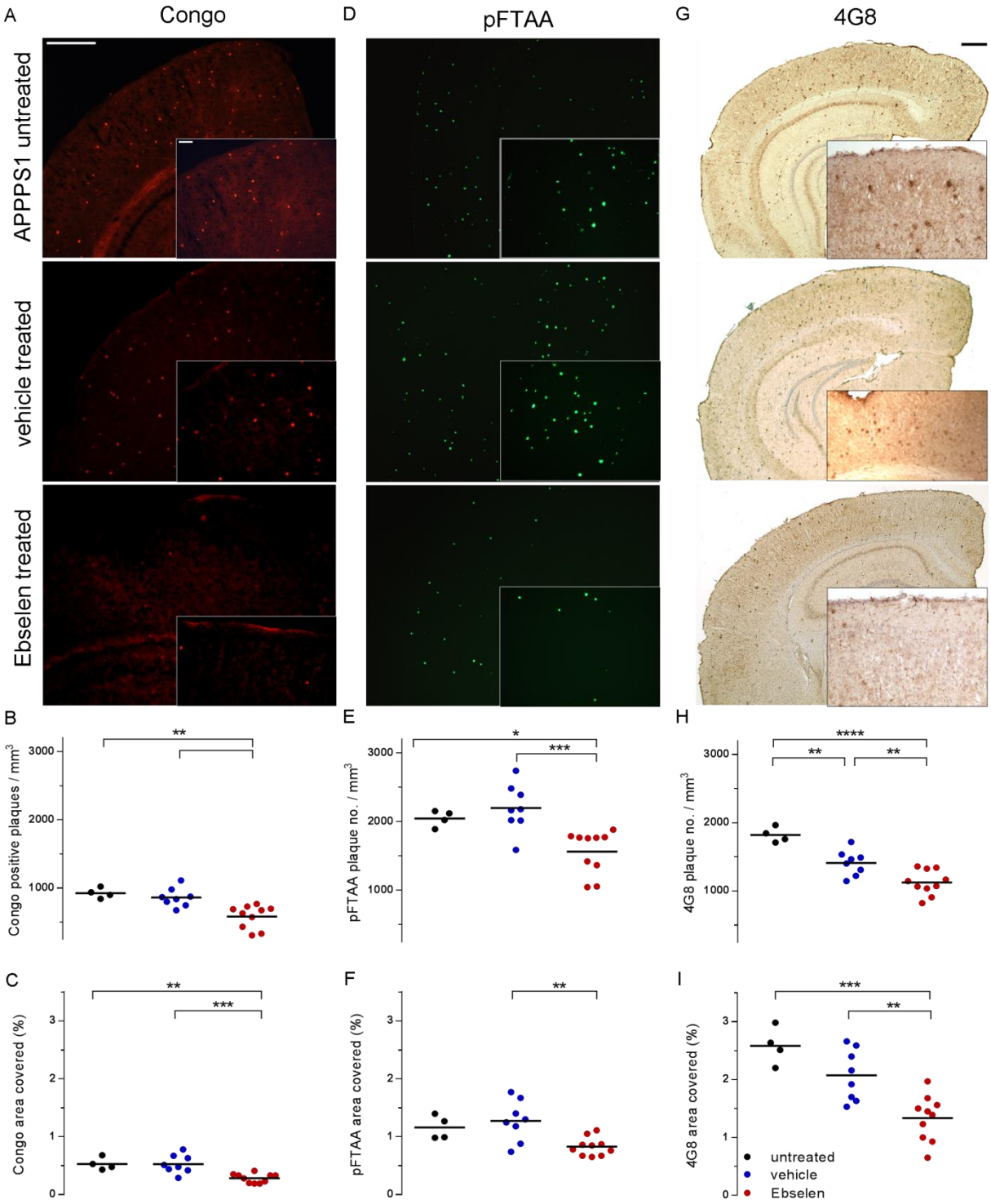

Figure 32: Amyloid plaque burden is significantly reduced in Ebselen-treated animals. (A) Congo red staining. (B, C) Stereological analysis of Congo red-positive plaques. (D) pFTAA to staining. (E, F) Stereological analysis of pFTAA-positive plaques. (G) Immunohistochemistry using 4G8 antibody. (H, I) Stereological analysis of 4G8-positive plaques. Each dot is representing one analyzed animal; Statistics: 1-way ANOVA; Scale: insert 100µm, outlet 5 mm.

This marked reduction of amyloid deposits can, in principle, be ascribed to either a reduction in APP processing and thus amyloid production or to an elevated amyloid

clearance. First, we analyzed amyloid production by quantification of APP levels and BACE-1 cleaved APP-C-terminal fragment ($APP_{\beta CTF}$)in the amyloidogenic pathway, which is known to serve as substrate for Aβ. Therefore, these proteins were analyzed in TX and SDS fractions of brain homogenates worked up by a 4-step extraction protocol (for details see 4.4.1) using the 6E10 antibody in Western Blots. Both fractions did not show differences in protein levels when analyzed separately (figure not shown). As visible in Figure 33, the mean of APP and $APP_{\beta CTF}$ protein levels in TX and SDS fractions likewise was not altered in Ebselen-treated mice versus the control groups. Thus, the reduced amyloid load in these animals was presumably not caused by decreased Aβ production.

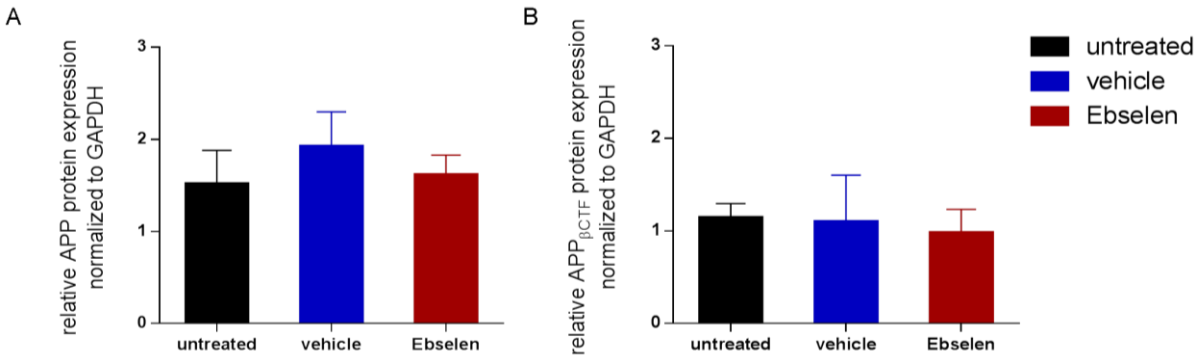

Figure 33: APP processing does not differ between treatment groups. Western Blot analysis of (A) APP protein expression and (B) $APP_{\beta CTF}$ in TX and SDS fractions of brain homogenates. Each group represents the mean of TX- and SDS-protein levels of brain homogenates, using 4 biological and 3 technical replicates. Statistics: 2-way ANOVA.

As described by Heneka *et al.,* [127], genetic NALP3 inflammasome inhibition in an AD-like mouse model led to amyloid deposit reduction via increased amyloid clearance and phagocytosis of microglia. Thus, we next tested the influence of Ebselen on microglial phagocytosis *in vitro* and measured the amount of the Aβ degrading enzymes neprilysin (NEP) and insulin-degrading enzyme (IDE) in SDS brain homogenate fractions of Ebselen-treated and control mice.

5.4.6 Phagocytosis is not altered by Ebselen *in vitro*, but Aβ insulin-degrading enzyme is upregulated *in vivo*

To analyze the influence of Ebselen on phagocytosis, we isolated CD11b+ microglia from 120 day old wildtype and APPPS1 animals and cultured them for one day. Subsequently, the cells were incubated with 50 µM Ebselen *in vitro* for 24 hours before a phagocytosis assay was performed. As visible in the Imaris software-based

reconstruction of one wildtype microglial cell in Figure 34A and orthogonal views of cultured and Iba1-stained wildtype microglia after the phagocytosis experiment in Figure 34B, microglia incorporated FBS-coated green fluorescent beads within 30 minutes.

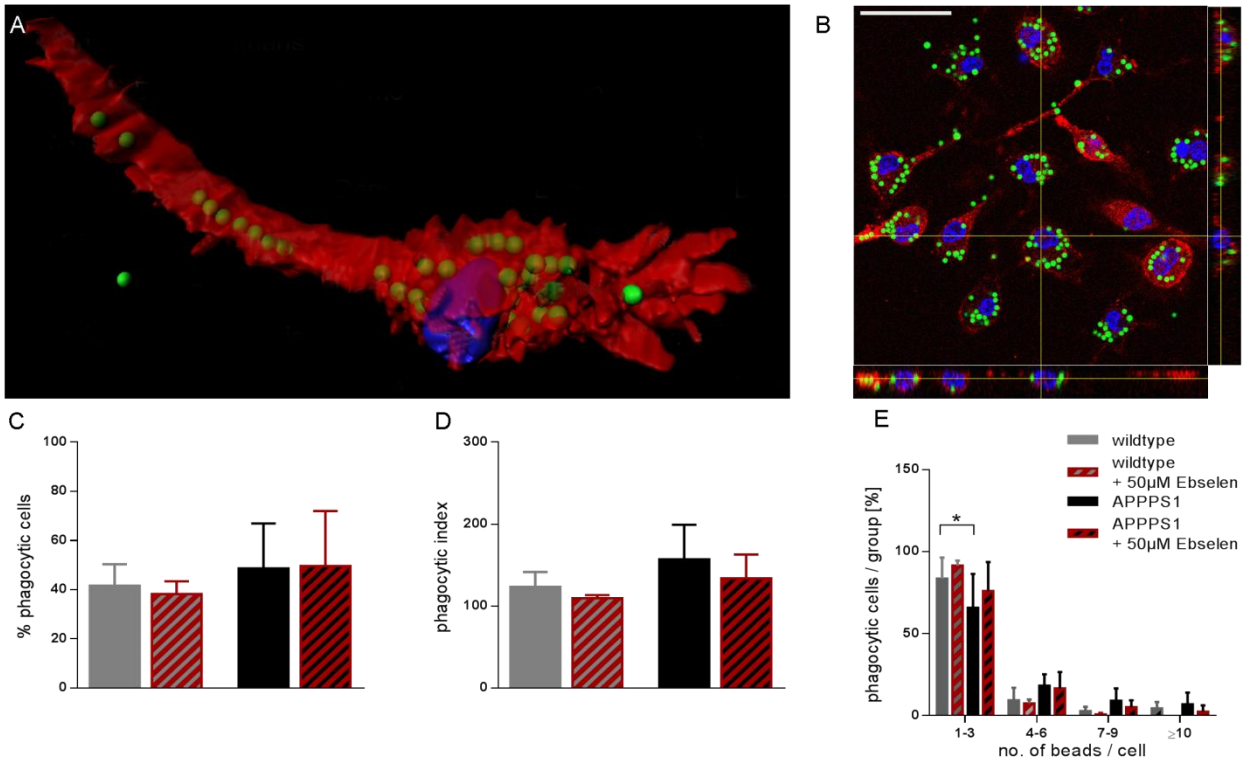

Figure 34: Phagocytosis of microglia is not altered upon Ebselen treatment *in vitro*. (A) Imaris software-based reconstruction of a representative wildtype microglial cell, stained with Iba1-Alexa568 engulfing green fluorescent FBS-coated beads. Cell nuclei are stained with DAPI. (B) Representative orthogonal views of cultured wildtype microglia from 120 day old mice, after fixation and Iba1 staining. (C) Quantification of the percentage of phagocytosing cells. (D) Phagocytic index, taking into account the amount of engulfed fluorescent beads per cell. (E) Percentage of phagocytic cells grouped by the number of incorporated beads per cell. N=5 animals per genotype; Statistics: 1-way ANOVA (C, D), 2-way-ANOVA (E); Scale: 50µm.

Quantifying the percentage of phagocytosing wildtype and APPPS1 microglia did not show any differences between the genotypes nor were there any changes by the addition of Ebselen (Figure 34C). To perform a more detailed analysis of phagocytosis, we grouped the phagocytosing cells according to the amount of incorporated beads and thus generated the phagocytic index as described previously [102], which again did not result in significant differences between the analyzed groups (Figure 34D). Only when visualizing wildtype and APPPS1 microglia incorporating a low number of beads (1-3 beads per cell), we found less APPPS1 microglia when compared to their wildtype counterparts (Figure 34E). Thus, at least *in vitro*, Ebselen is not influencing phagocytosis of microglial cells, indicating that it is less likely that phagocytosis of

microglia in Ebselen-treated animals *in vivo* is the reason for the observed reduction in amyloid burden.

Next, we analyzed the Aβ degrading enzymes NEP and IDE in SDS brain homogenate fractions of Ebselen-treated mice and controls by Western blotting (Figure 35A). NEP was slightly, but not significantly, reduced in Ebselen-treated and untreated APPPS1 mice in comparison to wildtype mice (Figure 35B). The same was true for IDE expression in untreated and vehicle-treated APPPS1 mice. As a reduction of IDE and NEP in AD has been described, this may be due to the young age of APPPS1 mice analyzed (95 days), as amyloid plaque pathology has just begun. Even if so, Ebselen-treated mice showed a significant increase in IDE levels compared to untreated APPPS1 mice.

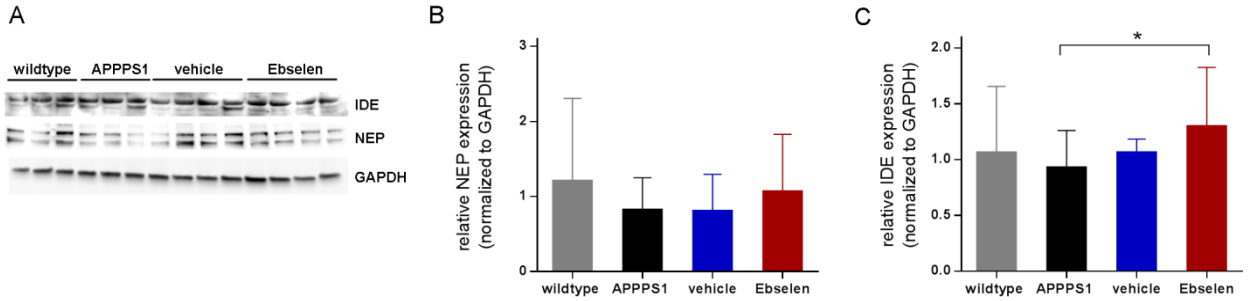

Figure 35: Amyloid degrading enzyme IDE, but not neprilysin, is elevated in Ebselen-treated mice. (A) Representative Western Blot for detection of insulin-degrading enzyme (IDE) and neprilysin (NEP) together with the housekeeping protein GAPDH. (B) Quantification of relative NEP expression to GAPDH. (C) Quantification of relative IDE expression to GAPDH. Blots from SDS brain extracted brains were repeated three times; Statistics: 2-way ANOVA.

In summary, the reduced amyloid burden in Ebselen-treated mice seems not to result from an alteration in APP processing. Furthermore, it is unlikely that an increased clearance by elevated microglial phagocytosis is the cause for the reduced plaque deposition. While we found an increase in one of the Aβ degrading enzymes, namely IDE, we are reluctant to conclude that this overall rather modest change in IDE entirely explains the rather substantial reduction in amyloid burden in Ebselen-treated APPPS1 mice.

5.4.7 Postsynaptic and vesicle markers are elevated in Ebselen-treated mice

Oligomers of Aβ are thought to be the toxic amyloid species and thus may lead to synapse loss, which subsequently drives neurodegeneration and cognitive decline [51]. To study the possible functional impact of reduced amyloid levels, we aimed at quantification of synaptic markers in the Ebselen-treated and control animals. We

therefore analyzed TX- and SDS-extracted brain homogenates for the amount of the presynaptic vesicle protein synaptophysin, the GABAergic presynaptic marker glutamic acid decarboxylase-65 (GAD65) as well as the post-synaptic density protein PSD95 by Western blotting.

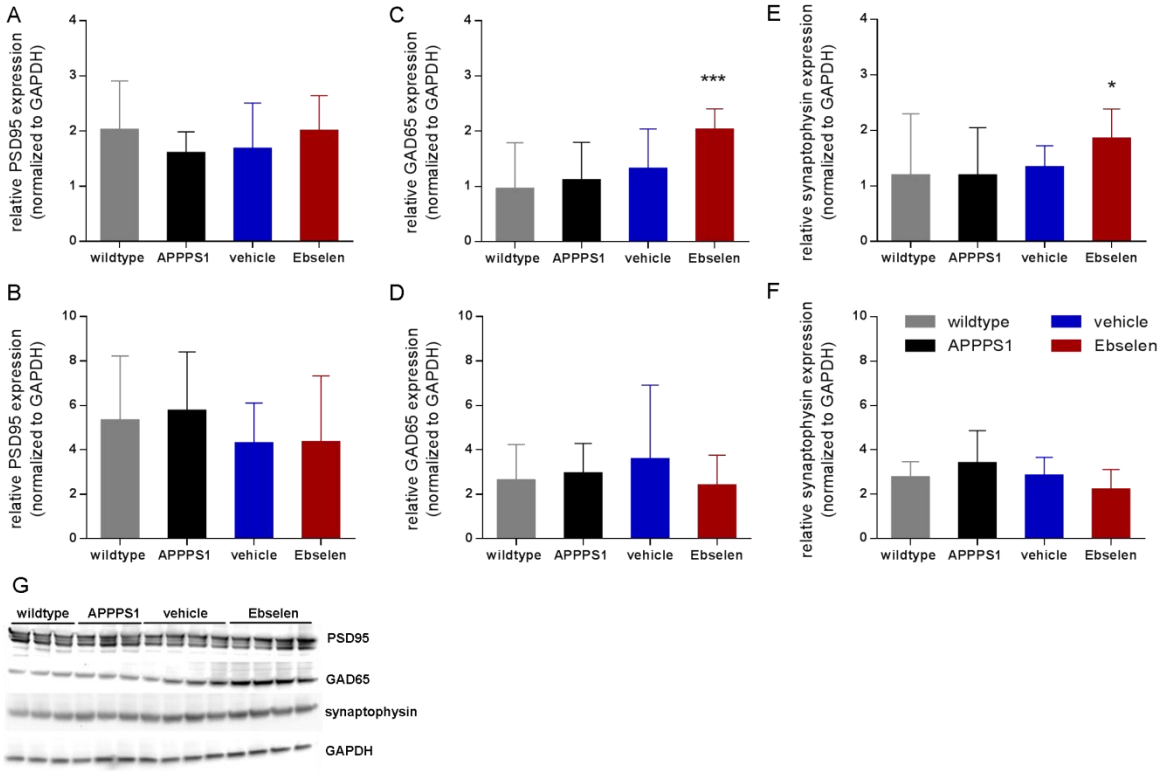

Figure 36: Presynaptic markers are elevated in Triton-X extracted brain fractions of Ebselen-treated mice. Quantification of Western blots for (A, B) post-synaptic marker PSD95 in TX (A) and SDS (B) extracted brain fractions; (C, D) pre-synaptic marker GAD65 in TX (C) and SDS (D) extracted brain fractions; (E, F) synaptophysin, a marker for pre-synaptic vesicles, in TX (E) and SDS (F) extracted brain fractions. (G) Representative Western Blot of TX-brain extracts from all treatment groups. Each blot was repeated three times with mentioned biological replicates in G; Statistics: 2-way ANOVA, asterisks over one group denote significant differences to all other conditions analyzed.

No changes for PSD95 protein levels could be detected in wildtype, untreated APPPS1 or vehicle- and Ebselen-treated animals in the TX (Figure 36A) as well as SDS (Figure 36B) brain fraction. On the other hand, more GABAergic pre-synapses were present in Ebselen-treated mice, as detected by GAD65 quantification of TX brain fractions (Figure 36C). In the SDS brain fraction, this difference was not present (Figure 36D). Likewise, Ebselen-treated animals exhibited more pre-synaptic vesicles when compared to wildtype and untreated as well as to vehicle-treated APPPS1 mice in the TX fraction (Figure 36E). Again, this difference was not present when quantifying synaptophysin in the SDS brain fraction (Figure 36F). A representative Western Blot of samples from a TX brain fraction is shown in Figure 36G.

Taken together, Ebselen treatment rescued the GABAergic and pre-synaptic vesicle densities in APPPS1 mice. If this rescue is translated into better cognitive outcome , i.e. results in a functional phenotype, had not been tested within the framework of this thesis and needs to be assessed in future experiments.
To further test whether NALP3 inflammasome inhibition may have a therapeutic effect, whilst avoiding the side-effects, such as local peritonitis as seen upon i.p. injection of Ebselen, we changed the treatment paradigm and applied Ebselen orally.

5.4.8 Ebselen applied in the drinking water does not show obvious side-effects

To reproduce the results from the i.p. treatment paradigm and to pathogenetically interfere at the initiation of amyloid deposition in APPPS1 mice, we started oral Ebselen treatment at an mouse age of 30 days. Again, Ebselen was dissolved first at a concentration of 0.5 mM in DMSO and thereafter in 25% β-cyclodextran, which served as vehicle. The weekly dose of Ebselen or vehicle was dissolved in the drinking water at a concentration that was similar to what had been used for the i.p. injections (30 mg/kg, weekly adjusted to the drinking volume and weight of each singly housed mouse). Before initiating the *in vivo* experiments, we ensured that Ebselen dissolved in water was stable at room temperature with light exposure for one week without a change in the pH-value (data not shown). For *in vivo* experimentation, the water was changed weekly and a special dripping-proof water dispensers were used to measure the exact amount of the drinking volume for each animal per week. APPPS1 mice were left untreated or received drinking water containing dissolved Ebselen or vehicle control starting at 30 days of age, until day 120. To check blood parameters and thus systemic tolerance of receiving Ebselen, blood was collected from the facial vein at the middle of the treatment period at day 75. At the end of the experiment, blood, serum and the brain were collected for further protein and gene analyses (Figure 37A).

All treatment groups gained weight normally (Figure 37B). In addition, APPPS1 mice receiving vehicle water drank comparable levels to mice receiving dissolved Ebselen in the drinking water (Figure 37C). A drinking volume of around 40 ml per week is regarded as normal [154]. All mice appeared to be healthy throughout the experiment, with no signs of adverse side-effects, also levels of the inflammatory marker CRP were unaltered in all mice analyzed (Figure 37D). Likewise, blood parameters measured at

day 75 and at termination of the experiment were unchanged in all experimental groups (Figure 37E, F).

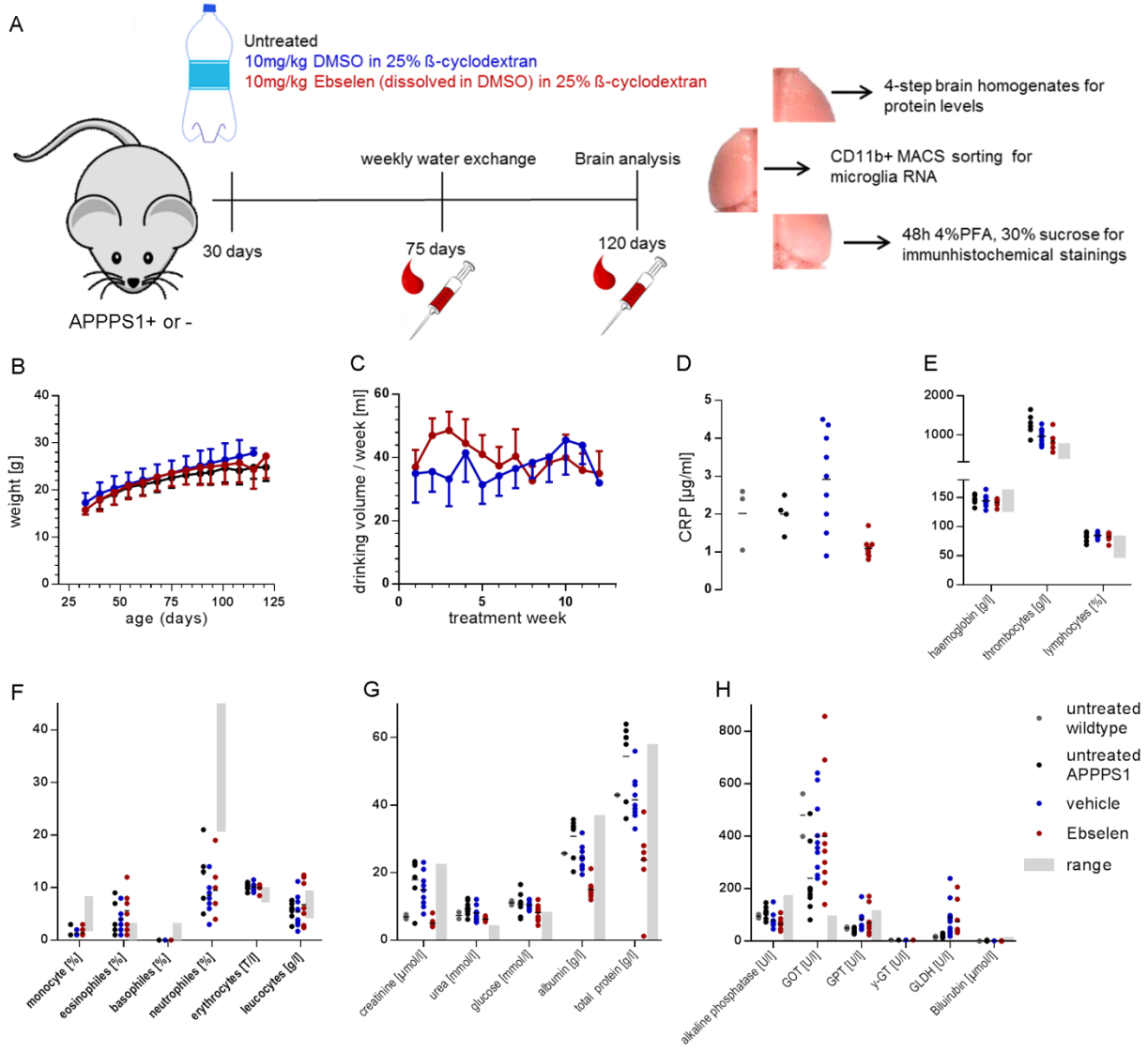

Figure 37: Oral application of Ebselen in Alzheimer-diseased mice does not induce adverse side-effects. (A) Experimental setup: APPPS1 or wildtype mice at an age of 30 days received normal drinking water *ad libitum* or special dripping-proof water dispensers with drinking water containing 30 mg/kg Ebselen (in 25% β-cyclodextran vehicle, adjusted weekly to the drinking volume and weight) or vehicle. Water was changed weekly for a treatment period of three months. After half of the treatment period, blood was collected from the facial vein. In addition, blood, serum and the brain were taken at the termination of the experiment. (B) Weekly weight gain of experimental animals. (C) Weekly drinking volume of experimental animals. (D) Serum C-reactive protein (CRP) levels at termination of the experiment. (E, F) Blood, (G) kidney and (H) liver parameters at experiment termination. Each dot is representing one analyzed animal; Statistics: 1-way ANOVA (B), Mann-Whitney test (C).

Also, there were no gross alterations of kidney and liver serum parameters (Figure 37G, H), while exclusively GOT liver levels were increased in all our experimental mice when compared to the range supplied by the company analyzing these parameters, namely

Synlab GmbH. As this phenomenon also included mice receiving normal drinking water, we can conclude that Ebselen was not the cause of increased GOT levels.

In summary, the oral application of Ebselen is well tolerated over a treatment period of 90 days at a dose of 30 mg/kg.

5.4.9 Microglial IL-1β mRNA levels as well as whole brain IL-1β and IL-18 protein levels remain unchanged upon oral Ebselen treatment

To assess whether oral application of Ebselen resulted in inhibition of the NALP3 inflammasome, we isolated CD11b+ microglia from the left hemisphere of the brain in order to analyze gene expression of NALP3 inflammasome-associated genes. Here, we could not detect any changes in gene expression (Figure 38A). Likewise, protein levels of IL-1β and IL-18 in the TBS-fraction of homogenized brains showed no differences between Ebselen- and vehicle-treated APPPS1 mice (Figure 38B, C).

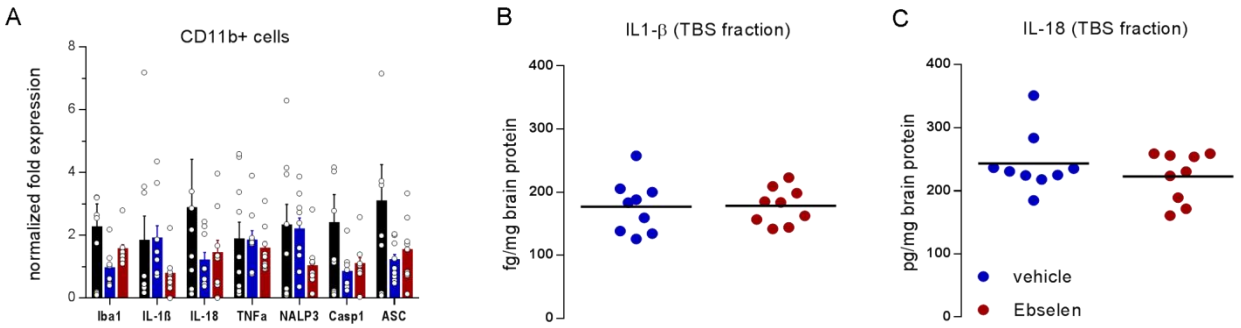

Figure 38: Microglial IL-1β mRNA levels and whole brain protein levels remain unchanged upon oral Ebselen treatment. (A) Gene expression analysis of CD11b-positive microglia. (B, C) Cytokine levels in TBS brain homogenate fractions for (B) IL-1β and (C) IL-18 normalized to whole brain protein levels. Each dot is representing one analyzed animal with (A) three or (B, C) two technical replicates; Statistics: 2-way ANOVA (A), 1-way ANOVA (B, C).

Thus, 90 days of oral treatment with Ebselen did not seem to inhibit the inflammasome, at least when assessing IL-1β and IL-18 cytokine levels as well as gene expression of inflammasome components. Nevertheless, as a very subtle reduction of microglial IL-1β mRNA expression in the i.p. treatment paradigm was linked to a strong reduction of amyloid burden (see 0 and 5.4.5), we decided to quantify the plaque deposition in brains of animals treated orally with Ebselen.

5.4.10 Congophilic and 4G8-labeled amyloid burden remains unchanged upon oral Ebselen treatment

The lower right hemisphere was cut into 30 µm thick free floating sections and stained with (i) 4G8 antibody (ii) pFTAA and (iii) Congo red as already explained previously (see chapter 5.4.5). As visible in Figure 39A, D and G, all stainings revealed a lack in change of amyloid burden. This was confirmed by stereological analysis of plaque number per mm^3 for each of the mentioned amyloid dyes (Figure 39B, E, H) as well as by the percentage of the area covered by amyloid (Figure 39C, F, I).

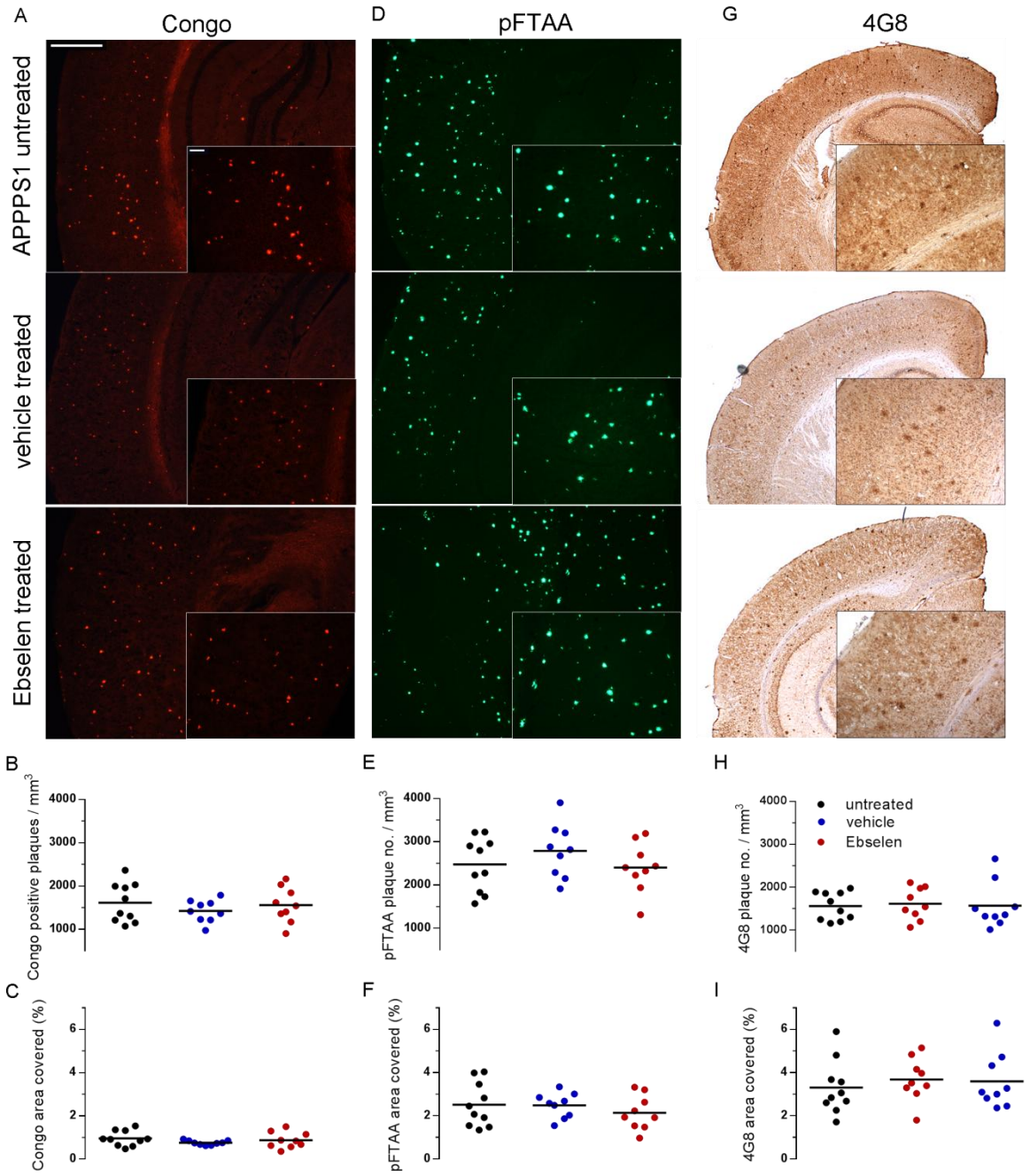

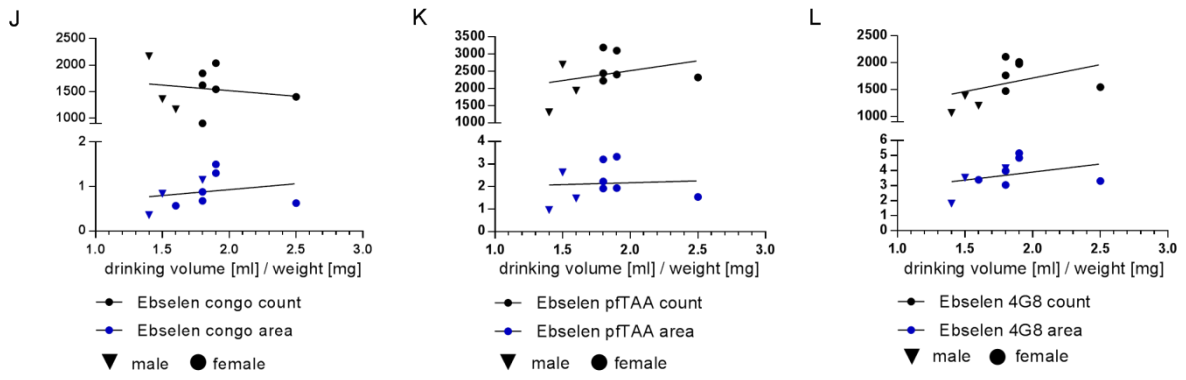

Figure 39: Amyloid plaque burden is not altered in APPPS1 mice treated orally with Ebselen. (A) Congo red staining of the cortex. (B, C) Stereological analysis of Congo red-positive plaque number per mm^3 cortex (B) as well as covered area by amyloid (C). (D) PFTAA staining of amyloid plaques. (E, F) Stereological analysis of pFTAA-positive plaque number (E) and covered area (F). (G) Immunohistochemistry of amyloid plaques in the cortex using 4G8 antibody. (H, I) Stereological analysis of 4G8-positive plaque number (H) and the cortical area covered (I). (J, K, L) Correlation of Ebselen taken up (measured by drinking volume normalized to body weight) to plaque numbers or the area covered by amyloid. Each dot is representing one analyzed animal; Statistics: 1-way ANOVA; Scale insert 100µm, outlet 5 mm.

Next, in order to ensure not to overlook subtle Ebselen-mediated effects, we individually correlated plaque number and plaque area to the amount of water (and thus Ebselen) taken up per gram mouse. Here, we also discriminated between the gender of all experimental mice. Even though female mice drank more, when normalized to their body weight, there was no correlation of the amount of Ebselen taken up and the plaque number or to the area covered by amyloid deposits (Figure 39D, G, J).

Next, we checked if Ebselen treatment may have influenced soluble Aβ species. All fractions from 4-step extracted brain homogenates were measured with an ultrasensitive electro-chemiluminescent immunoassay (MULTI-SPOT® Human (6E10) Triplex Assay) for $A\beta_{40}$ and $A\beta_{42}$ levels. All measured values were normalized to the amount of whole brain protein, as derived from a BCA assay. Results from the TBS and TX fraction were summed up representing soluble amyloid species. On the other hand, Aβ levels from SDS and FA homogenized brain fractions were summed up to indicate levels of insoluble Aβ species, while total amyloid burden is represented by the addition of the results of all brain fractions. As visible in Figure 40A, soluble $A\beta_{40}$ levels were increased in Ebselen-treated mice (129.0 ± 39.7 pg/mg brain protein) compared to vehicle-treated (119.2 ± 14.3 pg/mg protein) and untreated controls (77.4 ± 24.5 pg/mg protein). For $A\beta_{42}$ levels an increase of soluble species in Ebselen-treated animals (139.4 ± 52.2 pg/mg protein) versus untreated APPPS1 mice (83.0 ± 26.8 pg/mg protein), but not vehicle-treated mice (108.7 ± 14.1 pg/mg protein), could be detected

(Figure 40D). As expected from amyloid plaque stainings, no differences in insoluble $A\beta_{40}$ and $A\beta_{42}$ levels were found (Figure 40B, E). In addition, the total amount of $A\beta_{40}$ and $A\beta_{42}$ also remained unchanged in all groups analyzed (Figure 40C, F).

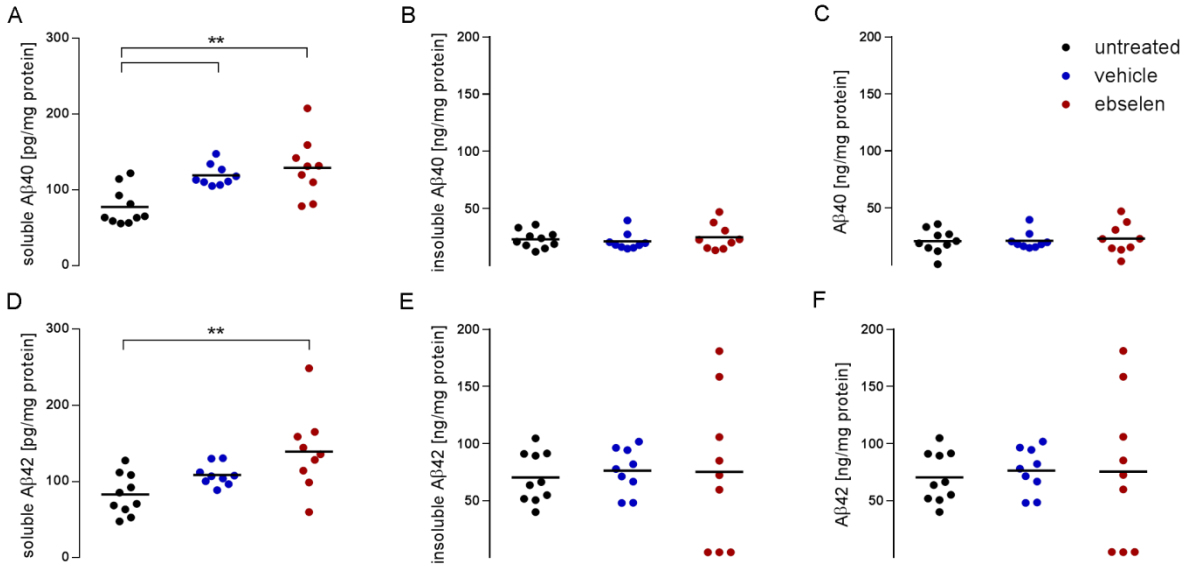

Figure 40: Cerebral amyloid levels do not differ substantially in all experimental mice. (A) Soluble $A\beta_{40}$ levels, measured in TBS and TX extracted brain fractions. (B) Insoluble species of $A\beta_{40}$ from SDS and FA extracted brain homogenates. (C) Total $A\beta_{40}$ amount. (D) Soluble $A\beta_{42}$ level from TBS and TX extracted brain homogenates. (E) Insoluble levels of $A\beta_{42}$ from SDS and FA extracted brain homogenates. (F) Total $A\beta_{42}$ amount. Each dot represents one analyzed animal with two technical replicates; Statistics: 1-way ANOVA.

In summary, oral application of Ebselen through drinking water does not induce any side-effects and appears to be well tolerated. Nevertheless, this treatment paradigm does not inhibit the inflammasome, as measured by inflammasome-related gene expression and cytokine protein secretion. No changes in amyloid plaque deposition were detectable using immunohistochemical staining or more detailed biochemical analyses, while only a slight increase of soluble $A\beta_{40}$ and $A\beta_{42}$ could be detected in Ebselen-treated mice. Therefore, oral application of Ebselen via the drinking water appears to have no substantial therapeutic effect in APPPS1 mice, at least at the doses used by us.

6 Discussion

In this thesis myeloid cells in the healthy and diseased central nervous system were characterized. The main focus of this work laid on microglia, the intrinsic immune cell of the brain, which can be exchanged by peripherally-derived myeloid cells after depletion of resident microglia using CD11b-HSVTK mice [130, 155]. Histological stainings point to the fact that these newly recruited myeloid cells can mimic microglial morphology in the brain. Nevertheless, it was unclear, whether these invading cells are indeed able to replace microglia phenotypically and functionally *in vivo*, which was the main question in the first part of this thesis. The second part of this thesis focused on the role of microglia in AD. Microglia are able to phagocytose and clear Aβ, a main pathological hallmark of AD, at least *in vitro* [91, 134, 135]. On the other hand, *in vivo* studies point towards a disability of these cells to tackle Alzheimer's pathology [104]. To reduce amyloid burden and thus improve AD outcome by manipulating myeloid cells in the CNS, this thesis utilized two approaches: First to exchange malfunctional endogenous microglia for more functional cells from the periphery using the CD11b-HSVTK system. Second to manipulate endogenous microglia to reverse their impaired into a more functional phenotype by inhibiting the NALP3 inflammasome.

6.1 Technical establishment of long-term in vivo *imaging*

To study endogenous microglia and peripherally-derived myeloid cells, a long-term two-photon imaging setup had to be established to monitor both cell populations in the living brain. First, delivery of GCV for CD11b-HSVTK mediated microglial depletion and installation of a chronic cranial window to the cortex, to allow live imaging, was arranged. We first tested less invasive approaches for GCV application via manual or automated topical delivery to the cortex, which appeared to be a promising approach, since it led to robust microglial depletion. Furthermore, a chronic cranial window up to 5 mm in diameter was able to be installed using this experimental setup. Nevertheless, these approaches allowed for imaging over one month only, as an angular window had to be installed. The latter led to turbidity and skull regrowth. In conclusion, topical automated GCV administration via miniosmotic pumps and imaging through a large cranial window appears to be a suitable approach for short-term imaging of microglial depletion and repopulation. As we wanted to monitor these cells for up to 50 days in the brain, we established the implantation of a manually adjustable icv cannula to allow

GCV delivery using a smaller chronic cranial window at the left hemisphere. Even though this approach is more invasive, the microglial depletion is robust and allowed the required long-term imaging.

To relocate our imaging position for more than seven realtime brain imaging sessions within two months, we established a custom-made head fixation, similar as described before [139]. Even though many head fixations are described, these setups typically do not allow a precise geometrical relocation of the position and are not made and tested for long-term fixation on the mouse`s head [5, 148, 156, 157]. The use of our custom-made titanium ring with a frontal guide notch and circular guide groove permanently attached to the mouse's head with dental cement, ensured head fixation of the animal at identical angles over various imaging sessions. As envisaged, relocation of the imaging position up to 50 days after the first imaging was possible. Only rarely fine tuning of the region of interest using blood vessel landmarks or the amyloid plaque pattern was required. Likewise the cranial window and the titanium ring remained unchanged at the head of imaged mice; only infrequently the ring had to be remounted.

There are conflicting reports about a possible microglial activation after chronic cranial window installation, e.g. by Yan *et al.* observing higher microglial numbers seven days after surgery [150]. Similarly another group reported microglial activation two days after installation of a cranial window accompanied by an increase in microglial numbers ten days after surgery [149]. This is why alternative approaches to the chronic cranial window have been established, one of which is the non-invasive thinned skull technique. Here, the skull is not opened but its thickness is reduced to 20 µm, where it becomes transparent and thus applicable to microscopy. The caveat of thinned-skull windows is that the skull quickly grows and thickens, thus becoming opaque already after one day of preparation which requires fresh preparation immediately prior to each imaging session [148]. As this results in variations in terms of imaging quality and a limited amount of preparations not exceeding three times at the same position, this approach is not suitable for long-term imaging [148]. Thus, we operated mice with a chronic cranial window, leaving the Dura mater intact and being as non-invasive as possible, while following experimental procedures as described before [139]. In our experimental preparations we could not detect signs of microglial activation two or seven days after surgery, as reported by others [25, 140]. Thus, we concluded that microglial activation after implantation of a chronic cranial window mainly depends on

the individual procedure and personal skills. Consequently, we started to image mouse brains five days after the experimental procedure.

Lastly, we had to discriminate endogenous from peripherally-derived myeloid cells visually. Endogenous microglia in FracGFP$^{+/-}$ mice carry a green-fluorescent label. We decided to utilize this mouse strain, as there are other possible mouse strains with tagged microglia, such as Iba1-GFP+ mice. Nevertheless, FracGFP$^{+/-}$ mice turned out to be brighter and less prone to fluorescent bleaching than Iba1-GFP+ mice. Especially the latter is very important for long-term imaging. In addition, in FracGFP$^{+/-}$ mice all Iba1-positive cells of the brain, namely microglia, were visible and tagged by the GFP signal. Nevertheless, it has to be kept in mind that one group reported a fractalkine receptor gene dose-dependent reduction of thioflavine- and 6E10 antibody-stained amyloid deposits in these mice, which, however, was only substantial in animals harboring a homozygous GFP insertion into the fractalkine receptor locus [121].

Apart from resident microglia in the brain also peripheral monocytes express the fractalkine receptor and are thus likewise GFP-labeled in FracGFP$^{+/-}$ animals [137]. As lethal irradiation kills all peripheral immune cells but spares resident microglia in the brain (since microglia typically do not proliferate, which makes them escape irradiation related cell death), we used a bone marrow-chimeric approach, including lethal irradiation, resulting in the death of all FracGFP$^{+/-}$ cells in the periphery. After subsequent reconstitution of the immune system with tdRFP-bone marrow from the respective reporter mice, irradiated FracGFP$^{+/-}$ mice carried green endogenous microglia in the brain, while harboring red peripheral immune cells.

6.2 Project Aim 1: In vivo *characterization of myeloid cell dynamics in the healthy brain*

After technical establishment of the experimental procedures required to answer our scientific questions, we exchanged endogenous microglia with myeloid cells from the periphery using the CD11b-HSVTK system and imaged this procedure *in vivo* using two-photon microscopy. First, depletion of microglia was imaged on a daily basis for the first ten days starting one month after bone marrow reconstitution in order to pinpoint the earliest time points of entry of peripherally-derived myeloid cells into the brain. We saw that already at day six dpd endogenous microglia underwent massive GCV-mediated cell death in CD11b-HSVTK mice, while the first red fluorescent peripheral

cells were detectable in the brain at that time point. Ten days after starting GCV delivery, nearly all green fluorescent microglia were gone and the brain was fully repopulated by peripherally-derived myeloid cells. In the first part of the thesis we imaged the late microglia depletion/early peripheral myeloid cell repopulation time points. We found that upon depletion of resident microglia the brain is repopulated by peripherally-derived myeloid cells, while in our model system proliferation of remaining green fluorescent endogenous microglia played no substantial role. Furthermore, these peripherally-derived cells distributed evenly throughout the entire CNS in a very short period of time and exceed the previous amount of resident microglia by 26%, as described before [155]. It is known, that the CNS can be colonized by inflammatory monocytes under disease conditions [158]. However, in our model tdRFP- and Iba1-positive cells remained in the CNS in contrast to inflammatory monocytes that do not stay in the CNS over a prolonged period of time [159].

Interestingly, a recent study by Elmore *et al.* reported that the microglial-depleted brain is rapidly filled up by proliferation of nestin-positive cells in the CNS, serving as microglial precursor cells, rather than recruitment of peripherally-derived myeloid cells. This study used a small-molecule inhibitor of the CSF1-receptor to deplete microglia [160]. One explanation for this discrepancy could be the leakiness of the blood-brain barrier in our system that possibly serves as recruiting stimulus, leading to rapid invasion of cells likely overruling proliferation. Irradiation was described to induce leakiness of the BBB and serves as precondition, that, together with injection of bone marrow, facilitates the infiltration of peripheral immune cells into the CNS [24, 27, 28, 159]. In addition, our icv cannula is locally disrupting the brain tissue and possibly leads to BBB leakiness next to its entry point. Indeed, stereological quantification of experimental animals depicted not only peripherally-derived myeloid cells in microglia depleted animals, but also up to 24% in irradiated, but not-microglia depleted TK- animals. Thus, in our experimental setup the BBB is likely to be leaky following irradiation and due to tissue disruption upon icv brain cannula implantation. Importantly however, the depletion of microglia in CD11b-HSVTK mice also leads to a rapid repopulation of the brain with peripherally-derived myeloid cells in absence of irradiation, as shown in a isochronic parabiosis experiment, in which TK mice were paired with actin-GFP reporter mice (Prokop, Miller, Drost, Heppner *et al.*, J Exp Med, in press). Even under these irradiation-free experimental conditions our group could show

that the microglia depleted brain is repopulated by Ly6Chi ‘inflammatory monocytes’ that give rise to Ly6Clow CD11c+ CX_3CR1+ MHCII+ ‘microglia- like’ cells by 60 days after entry into the brain (Miller, Prokop, Drost, Heppner *et al.*, unpublished observations).

Thus, depletion of resident microglia in CD11b-HSVTK mice results in the generation of a special niche for peripherally-derived myeloid cells which are recruited rapidly and robustly after microglial removal from the CNS. This is of great experimental importance, as this model allows the recruitment of defined myeloid subpopulations carrying neuroprotective or restorative molecules to the CNS, aiming at ameliorating e.g. various neurodegenerative diseases [74, 98].

To use these peripherally-derived myeloid cells, we morphologically and functionally characterized them in detail. Endogenous microglia were shown to have somata that, in contrast to microglial processes, occupy a specific position in the brain parenchyma and do not move substantially under homeostatic conditions [5, 25]. When quantifying the speed of somata of endogenous microglia in control conditions, we detected speeds of around 10 nm/s recorded over 30 minutes, which equals 36 µm/h. Nimmerjahn *et al.* reported, that only 5% of microglial cell somata move at 1 - 2 µm per hour [5]. Nevertheless, the speeds analyzed by Nimmerjahn *et al*. were directed movements including great track displacements of the cell bodies. Soma movement in our setting rather resembled a Brownian motion, i.e. the random motion of particles suspended in fluid. This random motion is characterized by uncontrolled and non-directed movements, where the particles ‘vibrate’ around their assigned tissue position with nearly no detectable track displacements. Indeed, somata tracks analyzed in this thesis showed a non-directed, random, circular shape (Figure 9D). This was also true for peripherally-derived cells that adopted microglial-like morphology in microglia depleted animals. On the other hand, peripherally-derived myeloid cells infiltrating TK- controls, possibly through a leaky BBB, moved faster than in TK+ mice and showed a more directed movement in the tissue.

When characterizing endogenous microglial cells and peripherally-derived myeloid cells with respect to their soma sphericity, indicating the roundness of the soma, we found no differences between these two cell types.

Peripherally-derived myeloid cell somata were smaller than endogenous microglia and did not evolve their morphology over 24 days in the tissue. In the literature, there is a

great range of microglial soma volumes, ranging from 60 to 1700 µm^3 [25, 161, 162]. This may certainly also depend on the fluorescent label of microglia and the detection method. One recent study also using Imaris (Bitplane) software for reconstructing and calculating somata of microglia, described the soma area of endogenous microglia in the cortex to be ~130 µm^2 [163]. This equals a volume of ~1100 µm^3 and is very similar to our findings, describing a microglial soma size of 963 µm^3, while peripherally-derived myeloid cell bodies had a volume of ~793 µm^3. In contrast, an earlier study stated that peripherally-derived myeloid cells mimicking endogenous microglia appear to have enlarged cell bodies [155]. However, the latter study did not quantify the size of cell bodies.

We also characterized somata of endogenous TK+ cells that are prone to GCV-mediated cell death. These cells showed an elevated soma size at day six and seven dpd, while no significant changes in soma speed and soma sphericity were detectable. This increase is well explained by the strong activation of these TK+ cells by GCV prior to cell death.

In summary, peripherally-derived myeloid cell bodies resembled those of microglial cells morphologically and did not drastically change when residing in the brain tissue over 24 days.

Next, we quantified microglial process morphology. As described in the literature, microglia are highly ramified cells that extend and retract their processes continuously to scan and thus surveil the brain environment for tissue damage and pathogens [5]. Surprisingly, peripherally-derived myeloid cells repopulating the brain, which normally do not harbour processes, adopted an arborized morphology as soon as they entered the CNS tissue. No time-dependent changes in the number of branch points per cell, the total length of all processes or the number of processes originating from the soma (primary filaments) were detectable over 24 days spent in the CNS tissue. When quantifying these parameters for both groups over all recorded time points, we saw that peripherally-derived myeloid cells were less branched, exhibiting shorter processes compared to their endogenous counterparts. These differences did not result from the first order of the processes, as the quantity of primary filaments was comparable between both cell populations. This rapid adoption of peripherally-derived myeloid cell morphology has been described before [23, 155]. Additionally, the values for process

parameters of cortical endogenous microglia fit well to the parameters of a recently published study [163].

As peripherally-derived myeloid cells can mimic microglial process morphology well, we tested if these processes are functional. We saw that the newly invading cells were able to extend and retract their processes as well as endogenous microglia. No significant changes in the speed of these movements were detectable. Furthermore, process movements of around 1 - 1.09 µm/min were by and large comparable to the motility of 1.5 µm/min described by Nimmerjahn *et al.* [5]. Thus, peripherally-derived myeloid cells not only adapted microglial process morphology, but seem also able to continuously scan and surveil the brain parenchyma by extending and retracting their processes. Moreover, we tested the reaction of both cell populations towards a tissue lesion. Endogenous microglia "seal" a laser-induced CNS lesion using their processes by site-directed motility at ~1 µm/min [4, 25], while we found a comparable movement speed of 0.6 ± 0.2 µm/min in a comparable experimental setup. Surprisingly, peripherally-derived myeloid cells reacted significantly faster towards a laser-induced lesion with a speed of 0.7 µm/min. Thus, peripherally-derived myeloid cells not only mimic microglial morphology, but can also functionally substitute their resident counterparts. This had been proposed by earlier reports, as no change in body weight, a normal cortical architecture and unaltered neuronal numbers could be detected in GCV-treated TK+ animals [18, 155]. Furthermore, a study by Varvel *et al.* was also able to show that peripherally-derived monocytes recruited to the brain respond to severe insult, such as kainic acid-induced neural degeneration, similarly to microglia [155].

A recent study by Ding *et al.* reported that GCV is a potent inhibitor of endogenous microglia proliferation, possibly indicating – if put in the wrong context – that the CD11b-HSVTK system may yield artificial or even wrong data [164]. However, this study used substantially higher concentrations of GCV than those used in our study. Ding *et al.* used daily i.p. injections of 25 - 100 mg/kg GCV, equalling ~3 mg per mouse, for up to 20 days [164]. As our miniosmotic pumps deliver a total volume of 200 µl, we only applied 500 µg per mouse. Furthermore, the above-mentioned quantification of microglia cell process movements towards a laser-induced lesion as well as baseline process extensions and retractions were measured for the majority of time points in presence of icv GCV application that do not differ from values described for "homeostatic tissue" in the literature [4, 25]. In addition, soma speed of endogenous

microglia at 24 dpd, where GCV delivery was terminated, does not differ from values gained during imaging where GCV application occurred (6, 7 and 10 dpd; data not shown). Thus, we are certain to exclude any influence of the herein used dose of 2.5 mg/ml GCV on microglial and peripherally-derived myeloid cell dynamics measured.

Lastly, it is reported in the literature, that microglial processes cover the whole brain parenchyma, where ~6500 cells occupy one mm^3 of brain tissue [5]. Thus, we quantified the cell distances of endogenous and of peripherally-derived myeloid cells. Here, similarly to reports in the literature, ~5500 microglia covered one mm^3 of brain tissue. We could detect that more peripherally-derived cells are in closer vicinity to each other compared to endogenous microglia, thus these cells are arranged as denser network in the tissue. Resident microglia had a territorial organization with the majority of cells having cell-to-cell distances above 50 µm and up to 120 µm, very similar to the cell-to-cell distances of 50 µm to 60 µm described by Nimmerjahn *et al.* [5]. As peripherally-derived myeloid cells harboured shorter processes and were more numerous, we expected that these cells arrange in closer proximity to each other. Indeed, this closer proximity and thus elevated cell number is required to cover the whole brain parenchyma while harbouring shorter processes. This was also reflected by the fact that >11000 peripherally-derived cells are present in one mm^3 of CNS parenchyma.

Altogether, peripherally-derived myeloid cells are capable to morphologically and functionally replace microglial cells *in vivo*. These cells robustly repopulate the whole brain parenchyma very rapidly, adopting a microglial-like morphology as soon as they enter the CNS. Their morphology is very similar to resident microglia and does not evolve over 24 days in the CNS. These peripherally-derived myeloid cells seem to be able to scan and surveil the entire brain parenchyma despite their shorter processes, which seems to be compensated by their close vicinity due to reduced cell-to-cell distances. Additionally, their process extension and retraction speeds are comparable to those of endogenous microglia. Finally, peripherally-derived myeloid cells seem to be more reactive towards a laser-induced tissue lesion than the intrinsic immune cells of the brain. Thus, peripherally-derived myeloid cells are in principle good candidates to replace impaired endogenous microglia in Alzheimer's disease and were tested in the Alzheimer disease context in the second part of this thesis.

6.3 Project Aim 2: Replacement of resident microglia by peripherally-derived myeloid cells in Alzheimer's disease

Many studies point to a beneficial role of peripheral myeloid cells in AD. To study this assumption experimentally, we replaced resident microglia with peripherally-derived myeloid cells in APPPS1 mice crossed to CD11b-HSVTK mice. Here, in contrast to the first part of this thesis, GCV was delivered for 38 days into the brain. Adjusted to the starting point of peripherally-derived myeloid cell entry into the CNS, as shown in the first part of this thesis, we imaged these newly recruited cells up to 38 days in the CNS in APPPS1-negative wildtype mice. APPPS1-positive animals were imaged weekly starting at day six dpd up to 48 days in the tissue.

Also in this AD setting, we were able to show that upon depletion of resident microglia the brain is filled up by peripherally recruited myeloid cells, and not by proliferation of remaining microglia. Peripheral myeloid cells distributed evenly throughout the entire CNS very rapidly and these Iba1-positive cells were around 34% more numerous in FracGFP$^{+/-}$;APP+ or –;TK+ mice in contrast to non-depleted controls, as described before [155]. Besides the already mentioned possible reasons for the recruitment of peripheral cells, the AD brain often has been described to go along with a leaky BBB (reviewed in [165]). Thus, stereological quantification of experimental animals resulted not only in the detection of peripherally-derived myeloid cells in microglia depleted animals, but also in irradiated, but non-microglia-depleted FracGFP$^{+/-}$;APP+;TK- and FracGFP$^{+/-}$;APP-;TK- animals. Nevertheless, as quantified up to 27 days dpd in the AD-like brain, the infiltrating cells in TK- mice did not increase over time and remained stable at low numbers.

The inhibition of microglia by Ding *et al.* [164] could also be refuted here as animals treated with GCV for 38 days showed no influence upon microglial cells when imaged in the brain for up to 24 days, where GCV treatment was ceased in the first study aim.

When assessing peripherally-derived myeloid cells upon microglia depletion in otherwise healthy brains, we could not detect any time-dependent changes of peripherally-derived myeloid cells in the first study aim. Now, monitoring these cells in the healthy CNS for 12 additional days revealed a decrease of soma speed, while soma size was increased. Thus, these cells seem to evolve their microglial-like somata morphology after 38 days in the non-AD tissue. On the other hand, we could not detect such time-dependent somata changes in APP+ animals after up to 48 days spent in the

tissue. An explanation could be that amyloid deposits present in these brains paralyze the invading cells, thereby precluding their evolution. A study by Krabbe *et al.* also points towards a paralysis of microglia in the AD context. This study showed that the intrinsic immune cells of the brain have an impaired directed process motility and reduced phagocytic activity in APP+ animals [102]. Therefore, we also analyzed somata of peripherally-derived myeloid cells in long-term GCV treated animals in AD and non-AD conditions more thoroughly.

First, soma movement speeds of cells were quantified time-independently. Here, as well as in all other investigated parameters we distinguished between cells touching an amyloid plaque from cells being further away from Aβ deposits in APP+ mice. As already mentioned, soma speeds of non-AD (wildtype) peripherally-derived myeloid cells were significantly elevated in comparison to those of endogenous microglia. Likewise, peripherally-derived myeloid cell bodies being distant to plaques were faster than their endogenous counterparts, while cell bodies in plaque proximity remained unchanged. Surprisingly, we also detected that peripheral-derived myeloid cells being distant to amyloid plaques as well as in non-AD animals were significantly faster than those cells being in close vicinity to amyloid plaques. Again, these data indicated that the AD-like microenvironment consisting of amyloid deposits, similarly as shown for endogenous microglia in an AD mouse model in a previous study [102], rapidly impairs these newly recruited peripheral myeloid cells. Interestingly, this impairment only affected process movements, while cell body speeds of endogenous microglia close to Aβ plaques were not affected. As previously discussed, soma speeds of endogenous microglia and peripherally-derived myeloid cells were found to be faster than what has been reported by Nimmerjahn *et al.* [5]. Again, the motion measured in this thesis rather represents an uncontrolled, non-directed movement around an assigned tissue position with subtle track displacements but a more circular shape (Figure 9D). Hypothetically, it cannot be excluded that only the faster peripherally-derived myeloid cell bodies were prone to paralysis, while the slower endogenous cell bodies cannot be further decreased. Additionally, cell bodies in APP+ animals were tracked over a time period of 48 days. Here, we could not detect significant changes between endogenous microglia and peripherally-derived cell body speeds. The movements of ~3 µm per week are comparable to the values published by Hefendehl *et al.* and Nimmerjahn *et al.* [5, 25].

When analysing time-dependent changes of soma sphericity, we could not detect any changes of peripherally-derived cell bodies in neither AD nor non-AD animals. Yet peripheral myeloid cells resembled well the sphericity of endogenous microglia in non-AD brains and of endogenous microglia being further away from amyloid plaques in APP+ brains, as we could not detect any significant changes there. Only peripherally-derived myeloid cell bodies residing next to amyloid plaques were more spherical than endogenous microglia in plaque proximity, which in turn were less spherical than endogenous cells being distant from amyloid deposits or in non-AD brains. It is known that endogenous microglia cluster around amyloid plaques and thus are polarized towards the deposits, which can explain their reduced sphericity. On the other hand, peripherally-derived myeloid cell arranged not as close to amyloid plaques when compared to endogenous microglia. The peripheral cells seemed not to cluster and polarize towards amyloid deposits, which could explain the unchanged soma sphericity in comparison to repopulating cells that were not in contact with Aβ. The fact that peripherally-derived myeloid cells are clustering around amyloid deposits only to a minor extent upon recruitment to the amyloid-carrying CNS, was already described in a previous study by Stalder *et al*. Here, the authors concluded that not all amyloid plaques are a target for invading cells or, alternatively, all amyloid plaques attract invading cells but only for a limited time early at plaque deposition [30].

Finally, we quantified soma sizes time-independently. Peripherally-derived myeloid cell bodies were overall smaller than those of endogenous cells in the non-AD and AD context. As it is described that microglia appear to have an altered state in the vicinity of Aβ plaques, described by an increased cell body size and decreased ramification [98, 161], we unexpectedly could not detect changes in sizes of somata in the vicinity of amyloid deposits.

Thus, we thoroughly analyzed the bifurcations of endogenous and peripherally-derived cells in the non-AD and AD context morphologically. For this purpose, we looked at process branch points per cell, the sum of all process lengths and the amount of first order processes originating from the soma (primary filaments). Looking at the time-dependent evolvement of these measurements, we could not detect significant changes in non-AD animals after up to 38 days in the CNS. In APP+ animals, we saw a slight increase of branching points and process lengths over time, which was likewise not significant. Analyzing cells over all time points, endogenous microglia and peripherally-

derived myeloid cells showed the same amount of primary processes and thus further differences in the process tree appeared not to be due to the bifurcation origin. As described already for the healthy brain using the experimental setup from the first part of this thesis, we, in the second part, likewise detected less ramified and shorter processes in peripherally-derived myeloid cells compared to endogenous microglia in non-AD and AD-like animals. The process tree of peripherally-derived myeloid cells does not change morphologically in plaque proximity. On the other hand, endogenous microglia are less ramified next to amyloid deposits compared to resident cells further away. Likewise, microglia more distant to plaques and in non-AD brains had significantly longer processes than endogenous cells touching Aβ plaques. Thus, morphological changes of endogenous microglia around Aβ deposits were reflected in a less ramified cell with shorter processes. This activation could not be detected in peripherally-derived myeloid cells, which harbored a less developed process tree.

Furthermore, testing the functionality of process movements in the healthy and diseased brain, we analyzed process extensions and retractions of microglia and peripherally-derived myeloid cells. These parameters did not show major time-dependent changes in the CNS tissue. Overall, the process extensions of the newly invading peripherally-derived myeloid cells were faster in the healthy brain compared to endogenous microglia. In addition, we could detect a paralyzing effect of the AD-microenvironment on process extensions and retractions of endogenous microglia. Likewise, the site-directed motility of microglia cells towards a laser-induced tissue lesion was slowed in the amyloid loaded brain, as described before [129]. Peripherally-derived myeloid cells were also prone to this impact on cell function and showed slowed process reactivity in the vicinity of Aβ deposits when analyzing process extensions, retractions as well as the site-directed motility towards a laser lesion.

Stereological quantification of FracGFP$^{+/-}$;APP+ or -;TK+ animals treated long-term with GCV showed elevated amounts of peripherally-derived myeloid cells. We quantified cell-to-cell distances as well as cell numbers per imaged ROI for endogenous microglia and peripherally-derived myeloid cells. As before, peripheral cells rapidly infiltrated the brain upon microglial depletion, but the total amount of peripheral-derived myeloid cells in the brain stabilized after 38 days in the healthy as well as AD-like brain tissue. Again, peripherally-derived myeloid cells arranged denser in the CNS, i.e. more cells were located in cell-to-cell radii of up to 40 µm when compared to endogenous microglia.

Thus, as in the first aim of this thesis, peripherally-derived myeloid cells compensated their shorter bifurcations by arranging themselves in closer vicinity to each other. This was underpinned by the fact that in non-AD and AD-like brains >11000 peripherally-derived myeloid cells were present in one mm^3, in contrast to ~6000 endogenous microglia. All in all, the measured microglial cell numbers per mm^3 tissue were again similar to the ~6500 cells per mm^3 described by Nimmerjahn *et al.* [5].

Altogether, peripherally-derived myeloid cells are capable to morphologically and functionally replace microglial cells *in vivo* in health and disease. These cells robustly repopulate the whole brain parenchyma rapidly, adopting a microglial-like phenotype as soon as they enter the tissue. Their morphology is very similar to that of resident microglia and evolves over 38 days in the healthy CNS, with no time-dependent changes being detectable in the amyloid-loaded brain. Finally, peripherally-derived myeloid cells seem to be more functional than the intrinsic immune cell of the brain in the healthy brain only. Process motilities of peripherally-derived myeloid cells are markedly slowed in the AD-like brain to a similar extent as the already described paralysis of microglia in AD. As the soma sphericity and process tree of peripherally-derived cells remains unchanged in the vicinity of amyloid plaques and as these cells are in greater distance to deposits, we speculate, that peripherally-derived cells are not actively recruited to plaques.

Amyloid deposits and long-term GCV treatment do not seem to be sufficient stimuli for peripherally-derived myeloid cells. Nevertheless, we still believe that these cells are good candidates for effectively clearing amyloid, if an additional stimulus is added in order to guide active recruitment and priming of these cells towards plaques thus increasing their functionality in the amyloid microenvironment.

6.4 Project Aim 3: Phenotypic modulation of endogenous microglia by NALP3 inflammasome inhibition as therapeutic strategy for Alzheimer's disease

Recent studies (3.3.1) described a novel role of the NALP3 inflammasome in the pathogenesis of AD. This sensor of innate immunity, present in myeloid cells, such as monocytes and microglia, appears to be a promising target for therapeutic manipulation in AD. A genetic NALP3 knock-out, for example, reduced amyloid burden in an AD-like mouse model, which also resulted in an improved microglial phagocytosis [123]. As until

recently, no specific inhibitor of this multicomplex protein was described, Prof. Veit Hornung (University of Bonn) very recently discovered that Ebselen, a well-known organoselenium compound, is specifically inhibiting NALP3 (personal communication). Ebselen is listed as a safe and approved molecule in the U.S. National Institutes of Health Clinical Collection. We therefore tested whether Ebselen is able to combat AD pathology in an AD-like mouse model *in vivo*.

To evaluate the potential of Ebselen to inhibit NALP3, we used peritoneal macrophages that were stimulated to induce NALP3 inflammasome activation *in vitro*. Activation of the NALP3 inflammasome requires two stimuli to induce downstream signaling: the first stimulus acts over Toll-like receptors and results in an elevation of pro-IL-1β, pro-IL-18 as well as NALP3 mRNA. Further stimuli, like urine crystals, ATP or Aβ, lead to oligomerization of NALP3, recruitment of the adaptor protein ASC and of Caspase1, which is subsequently cleaved and activated. This active protease is then able to cleave the cytokines IL-1β and IL-18, which are released into the cytosol. [128] Stimulation of peritoneal macrophages with LPS and ATP in the presence of 50 µM and 100 µM Ebselen resulted in a suppression of inflammasome activation, as evidenced by IL-1β secretion, while other immune markers that do not rely on NALP3 activation, such as TNFα, remained unaffected. Furthermore, a viability assay showed that Ebselen up to 100 µM was tolerated well *in vitro*.

For *in vivo* experimentation, we then assessed the onset of NALP3 inflammasome activation in our AD transgenic mouse model. Recent reports identified inflammasome activation in AD patients and reported that Aβ species are regarded as activator of the NALP3 complex [127, 129], while more detailed insights in the dynamics of NALP3 activation in APPPS1 mice were still lacking. Therefore, we analyzed inflammasome-related gene expression and the secreted protein levels of IL-1β and IL-18 in APPPS1 mice of different ages. 30 day old APPPS1 mice harbored no amyloid pathology and subsequently do not show changes in gene expression of inflammasome components or of cytokine mRNA levels. At 120 days, where robust plaque pathology can be found in the cortex of APPPS1 mice, IL-1β cytokine gene expression was significantly elevated, which translated into increased IL-1β protein levels in APPPS1 mice at 250 days of age, when the amyloid pathology is very severe.

For *in vivo* use of Ebselen, we aimed at interfering with the initiation of plaque pathology in APPPS1 mice at 30 days of age. The dosage of Ebselen was based on a recent

study showing that 10 mg/kg of peripherally applied Ebselen crosses the BBB in mice [151]. To our surprise, 50% of all mice treated this way with Ebselen for 45 days died, while no adverse side-effects in blood parameters were detectable at the time of death. When terminating this experiment and assessing all remaining mice at the age of 95 days, where a substantial amount of amyloid plaque pathology is present in APPPS1 mice [136], we found no changes in serum parameters that would point to a systemic side-effect of the drug. Likewise, C-reactive protein, as robust marker for systemic inflammation, was not elevated in Ebselen-treated mice [166]. However, we observed a swollen abdomen and signs of Ebselen precipitation in the peritoneum of those mice that received Ebselen. In addition, histological examination of the peritoneum and the liver revealed signs of a local peritonitis as cause of death in these animals. As vehicle-treated mice did not show an elevated increase in sudden deaths, we can exclude a toxic effect of the vehicle. However, there are reports indicating cellular toxicity caused by Ebselen [167, 168]. As these adverse side-effects seemed to be restricted to the peritoneum, while sparing systemic alterations, we assumed that an influence on the CNS seemed to be rather unlikely and we analyzed Ebselen-treated mice with respect to cerebral amyloid pathology.

Stereological quantification of amyloid burden, using three different markers of amyloid, showed a robust reduction in plaque numbers per mm^3 cortex and in the area covered by amyloid exclusively in Ebselen-treated mice. The reduction of ~30% amyloid burden was similar to what has been published for AD-like mice being deficient in NALP3 [127]. Gene expression in the brain of Ebselen-treated APPPS1 mice showed that IL-1β expression was reduced in microglia. Surprisingly, we also detected an elevation of NALP3 mRNA, which might represent a compensatory upregulation of microglia to overcome the inhibition of this multi-protein complex.

However, despite these changes on the genetic level, Ebselen-treated animals did not show a significant reduction of the protein cytokine levels of IL-1β and IL-18 in Ebselen-treated APPPS1 mice compared to the respective controls. Surprisingly, an elevation of IL-1β and IL-18 protein in the brains of untreated APPPS1 mice aged 95 days could be detected in comparison to age-matched wildtype mice. This was unexpected, as we found no changes in IL-1β and IL-18 protein levels before the age of 250 days in APPPS1 mice in our previous assessments, which may be explainable by the fact that in our previous measurements protein levels were analyzed in RIPA-extracted whole

brain homogenates, while now these 4-step extracted brain homogenates are known to harbor cytokines and soluble proteins at a higher concentration, where differences naturally occurring thus may be detectable more easily. As the increase in IL-1β and IL-18 was rather subtle in 95 day old APPPS1 mice, we assume that a reduction, e.g. conferred by Ebselen-treatment, is difficult to be detected in AD-like mice at this early time point and may only be measurable at later time points, where IL-1β and IL-18 levels in the course of AD are substantially higher and thus are a better detectable "target" for Ebselen actions.

Surprisingly, the stereological quantification of amyloid burden exhibited a decrease of 4G8 labeled plaques in vehicle-treated mice compared to untreated controls. Since it was reported that injections of unspecific antibodies can lead to proinflammatory changes of the immune system resulting in reduced amyloid burden [169], it is possible that similar effects also took place in our vehicle-treated mice.

When addressing the possible cause of reduced amyloid load upon Ebselen-induced NALP3 inflammasome inhibition, we assumed that either a reduced Aβ production and/or an elevated amyloid clearance may take place. We could, however, not detect less APP protein and APP-C-terminal fragment processing upon Ebselen treatment, similarly as shown for AD-like mice lacking genetic NALP3 [127]. The latter study, however, showed that microglial phagocytosis was increased and that the levels of the amyloid degrading enzyme IDE were upregulated [127]. When assessing these amyloid clearance mechanisms, we found no effect of Ebselen on microglial phagocytosis, at least *in vitro.* Although the *in vivo* setting of microglial Aβ phagocytosis in the living brain presents a different situation, we assume it as rather unlikely that microglial phagocytosis can explain the *in vivo* effects seen upon Ebselen treatment. In contrast, we found increased IDE levels in Triton-X extracted brain homogenates of Ebselen-treated mice, while the amyloid degrading enzyme neprilysin was unaffected. Since the increase of IDE was subtle and not significantly different to vehicle-treated APPPS1 mice we also concluded that IDE changes are probably not sufficient to explain the rather robust amyloid decrease in Ebselen-treated mice.

Besides inhibiting the NALP3 inflammasome, Ebselen is known to be a multifunctional modulator of metallo-proteins, enzymatic cofactors, gene expression, epigenetics, antioxidant defenses and immune systems [72]. Thus, other non-NALP3-dependent related effects may have conferred to the observed reduction in amyloid burden in

APPPS1 mice treated with Ebselen. For example, chronic inflammation, especially at late stages of AD, is known to induce toxic reactive oxygen species (ROS) production, which may aggravate disease pathology – and thus ameliorate disease when inhibited. Some non-steroidal anti-inflammatory drugs (NSAIDs) are able to reduce ROS and its chronic use has been associated with a reduced incidence of AD [170]. Likewise, the application of certain NSAIDs or different flavonoids to AD mouse models reduced ROS as well as AD pathology [171-173]. Besides, Ebselen has also been shown to be a strong immune modulator by altering the level of various cytokines. For example, Ebselen has been shown to change the immune milieu in AD mice by inhibiting pro-inflammatory IL-6 production from glial cells and thereby leading to increased amyloid clearance [72, 98]. Moreover, Ebselen has been described to inhibit the DNA-binding capacity of various transcription factors, including specific protein 1 (Sp1) and NFκB [174]. Sp1 was recently shown to be elevated in AD patients on mRNA and protein level as well as in the cortex and hippocampus of AD transgenic mice [175]. This transcription factor can regulate the expression of several AD-related proteins, including APP and tau, and interference with its binding capacity could, in principle, ameliorate disease pathogenesis [175]. Likewise, NFκB was shown to have binding sites in the promoter regions of APP and BACE. In this way, reduction of the binding capacity of this transcription factor can lead to decreased APP expression and reduced amyloidogenic APP processing resulting in alleviated Aβ pathology [176]. Nevertheless, substantial Sp1 and NFκB inhibition through Ebselen is unlikely, as we did not see a change in the expression or in the processing of APP in Ebselen-treated APPPS1 mice.

Finally, we wanted to test if the decrease in amyloid burden may have a functional impact, namely reducing neurodegeneration ultimately impacting cognitive performance in AD. We therefore quantified synaptic markers in APPPS1 mice treated with Ebselen or with vehicle, as synapses are particularly vulnerable already early in AD, ultimately resulting in neurodegeneration [56]. We found the levels of the pre-synaptic vesicle marker synaptophysin and of the GABAergic pre-synapse marker GAD65 elevated in Triton-X extracted brain homogenates of Ebselen-treated APPPS1 mice, while the amount of the post-synaptic density protein PSD95 remained unchanged. Since it is known that the analyzed markers are reduced in AD, especially around amyloid deposits [177, 178], it is possible that the increase of presynaptic markers in Ebselen-

treated mice is merely a consequence of a decrease in amyloid deposits. However, we could not detect a reduction in synaptic markers in untreated or vehicle-treated APPPS1 mice when compared to wildtype mice. Thus, plaque burden in 95 day old APPPS1 mice apparently does not go along with significantly reduced levels of synapses - possibly indicating that Ebselen is not only rescuing the amyloid-driven reduction in synaptic density, but also elevates the amount of pre-synapses, even beyond the level of wildtype mice. To formally test whether the elevation in presynaptic markers has an impact on cognition, behavioral testing of Ebselen-treated mice is required. Since the herein used APPPS1 mouse model exhibits detectable behavioral deficits only at 250 days of age [136] an entirely new experimental plan needs to be set up in future experiments.

To test Ebselen treatment in APPPS1 mice without adverse side-effects, we applied Ebselen orally as shown in rodents [179-181]. All published studies used gavage two times per day, which apparently did not result in severe side-effects. Likewise, Ebselen is used in recent clinical trials in humans orally and is considered non-toxic [182, 183]. Thus, the mortality upon i.p. Ebselen treatment, as observed by us, seems to be a drug formulation issue. Based on our findings, we consider that Ebselen precipitated in the peritoneum upon i.p. injections and induced local cellular toxicity. We therefore repeated Ebselen treatment using an oral application regimen by the drinking water. Weekly measurements of body weight and drinking volume of singly housed mice were used to monitor and to adjust the individual doses of Ebselen and vehicle per time. Oral Ebselen application to APPPS1 mice at the age of 30 days until day 120 was tolerated well, without evidence for side-effects, as visible from various clinical blood and serum values. However, this oral Ebselen administration, while being tolerated well, did not result in alterations of NALP3 inflammasome-related gene expression nor alterations in IL-1β and IL-18 protein levels in Ebselen-treated APPPS1 mice. As inflammasome-related changes in the Ebselen i.p. trial were admittedly rather mild, but resulted in robust amelioration of amyloid plaque pathology, we continued our studies and analyzed the brains of these orally Ebselen-treated APPPS1 mice for the amount of amyloid burden. However, in this instance we did not detect any changes in plaque burden by stereological quantification, even when using various amyloid dyes known to detect different amyloid species. Furthermore, we could not detect a correlation between the amount of Ebselen taken up and the plaque burden of individual mice.

Biochemical levels of total and insoluble $A\beta_{40}$ as well as $A\beta_{42}$ species were also unchanged in Ebselen-treated compared to untreated and vehicle-treated animals, while soluble $A\beta_{40}$ and $A\beta_{42}$ levels were elevated in Ebselen-treated mice. As soluble amyloid species are reported to be the more toxic amyloid species, which have been shown to selectively disrupt learning and memory *in vivo* [184], oral application of Ebselen may even go along with a rather unwanted effect. While we have no functional data to follow this concern, it also needs to be said that soluble oligomeric Aβ species are present at high concentrations in the vicinity of amyloid plaques [185]. Since soluble amyloid species are in equilibrium with Aβ deposits and thus can associate and dissociate from existing sediments [186, 187], the initiation of a (therapeutically induced) disorganization of core amyloid plaques, e.g. by Ebselen treatment, may explain this increase in soluble Aβ levels.

However, the most obvious explanation for the lack of a positive outcome upon oral Ebselen administration is the failure of Ebselen to reach the CNS at a sufficient dose. This may be due to a low bioavailability of the doses used by us. Even if comparable concentrations were used by published oral gavage applications in mice, the formulation for delivering Ebselen via the drinking water may cause a problem [179-181]. Many of the published studies applying Ebselen orally used 5%-CM cellulose instead of 25% β-cyclodextran as vehicle. Furthermore, Ebselen may have been degraded in the upper gastrointestinal tract, a fact that is circumvented by gavage dosage. Lastly, it has to be considered that the amyloid reduction by i.p. Ebselen treatment could be due to reasons not related to Ebselen, as already mentioned.

6.5 Conclusion and Outlook

CD11b-HSVTK mice are a useful tool to replace endogenous microglia with peripherally-derived myeloid cells. The recruited myeloid cells robustly and rapidly repopulate the whole brain parenchyma, adopting a microglia-like morphology as soon as they enter the CNS tissue and are – at least in part - capable to functionally replace microglial cells *in vivo*. After entering the brain, their soma and process tree morphology becomes alike that of resident microglia, and does further develop over 38 days in the CNS tissue in the healthy brain, while no such morphological changes and adaptation occurs up to 48 days in the brain of AD-like mice. In AD and non-AD brains the more numerous repopulated myeloid cells seem to be able to scan and surveil the entire brain parenchyma despite their shorter processes, which are compensated by their shorter cell-to-cell distances. Furthermore, these newly recruited cells are able to retract and extend their processes similar to that of resident microglia and they are more reactive towards a laser-induced tissue lesion in the healthy CNS. In the vicinity of Aβ plaques, the baseline process movements of these peripherally-derived myeloid cells as well as their reactivity towards a tissue lesion gets quickly impaired. Despite the per se – based on the parameters investigated by us - increased functional potential of peripherally-derived myeloid cells in the healthy brain, these newly recruited CNS-residents – alike resident microglia – apparently get dysfunctional as soon as they enter an Aβ-containing microenvironment. Consequently, they also lack the capability to reduce amyloid deposits, possibly because these peripherally-derived myeloid cells do not get recruited to amyloid deposits.

Yet, peripherally-derived myeloid cells appear to be good candidates to ameliorate AD pathology, as recently shown by Hohsfield *et al.* [111]. Future work, identifying an additional stimulus for recruitment and/or priming of peripherally-derived myeloid cells to amyloid deposits, may turn these cells into effective amyloid burden fighters.

Additionally, the paradigm of the recruitment of new cells to combat Aβ pathology may be tested in two other mouse models, allowing to deplete microglia [160, 188]. However, in contrast to CD11b-HSVTK mice, repopulation in these other microglia-depletion paradigms occurs not through peripherally-derived myeloid cells, but through proliferating (CNS-intrinsic) microglial precursor cells ([160], [188, 189]).

Apart from cell exchange strategies, the stimulation of malfunctional endogenous microglia in AD was tested. While the inhibition of the NALP3 inflammasome by Ebselen

results in substantially reduced amyloid pathology when applied intraperitoneally to APPPS1 mice, the formulation of Ebselen for peripheral administration needs to be improved, as i.p. application induces toxic side-effects and oral application through the drinking water conferres no positive effect on amyloid burden. Upon optimization of the formulation of Ebselen, administration of this drug prior to the onset of plaque pathology as well as in plaque-carrying conditions in AD-like mice are required to pinpoint the therapeutic potential of NALP3 inflammasome inhibition. Additionally, the analysis of potential cognitive improvement as major goal for the treatment of dementias has to be added by performing behavioral and cognitive assays in Ebselen-treated AD-like mice. Alternatively, other NALP3 inhibitors that were published only very recently, and were shown to be bioavailable for the CNS after peripheral administration [190, 191], may be tested in similar preclinical settings.

7 Appendix

7.1 Abbreviations

°C	grad Celsius
Aβ	amyloid-beta
aCSF	artificial cerebrospinal fluid
AD	Alzheimer`s disease
ADAM	a disintegrin and metallo-proteinase
AICD	APP intracellular domain
ANOVA	analysis of variance
APP	amyloid precursor protein
APLP1/2	amyloid precursor like protein 1/2
APPPS1	Amyloid Precursor Protein Presenilin 1 mutation
APS	ammonium persulfate
ASC	apoptosis-associated speck-like protein containing a CARD
ATP	adenosine triphosphate
BACE	β-Site APP cleaving enzyme
BBB	blood-brain barrier
BCA	bicinchoninc acid
BM	bone marrow
bp	base pairs
CA1	Cornu Ammonis Region 1
CARD	Caspase activation and recruitment domain
Casp1	Caspase 1
CD	cluster of differentiation
CNS	central nervous system
CO_2	carbon dioxide
CRP	C-reactive protein
CT	cycle threshold
CSF	cerebrospinal fluid
CSF-1	colony-stimulating factor 1
CX3CL1	fractalkine ligand
CX3CR1	fractalkine receptor
d	day
DAB	diaminobenzidine
DAPI	4',6-Diamidin-2-phenylindol
ddH_2O	distilled deionized water
DMEM	Dulbecco's modified eagle medium
DMSO	dimethylsulfoxid
DNA	desoxyribonucleic acid
dNTP	desoxynucleoside triphosphates
dpd	days post depletion
ECL	electrochemiluminescence
EGFP	enhanced green fluorescent protein
Elisa	enzyme-linked immunosorbent assay
FA	70 % formic acid in ddH_2O
FBS	fetal bovine serum
FracGFP	fractalkine receptor GFP knock-in mice
G	gauge
GAD	glutamate decarboxylase
GCV	ganciclovir
GFP	green fluorescent protein
h	hour
H_2O	water
H_2O_2	hydrogen peroxide
HBSS	Hanks balanced salt solution
HCl	hydrochloric acid
HSV	herpes simplex virus
Hz	herz
Iba1	ionized calcium binding protein 1
icv	intracerebroventricular
IDE	insulin-degrading enzyme
IL	Interleukin
i.p.	intraperitoneal
i.v.	intravenous
LPS	Lipopolysaccharide

M	Molar
MACS	magnetic associated cell sorting
MCI	mild cognitive impairment
M-CSF	macrophage colony stimulating factor
min	minute
mRNA	messenger RNA
MSD	Mesoscale Discovery
NA	not applicable
NaCl	sodium chloride
NALP3	NACHT, LRR and PYD domains-containing protein 3
NaOH	sodium hydroxide
NEP	neprilysin
NF-κB	nuclear factor-κB
NFTs	neurofibrillary tangles
NGS	normal goat serum
n.s.	not significant
NOS	nitric oxygen species
NSAID	Nonsteroidal anti-inflammatory drug
PBS	Phosphate buffered saline
PBS-T	PBS with Tween20
PBS-TX	PBS with Triton-X100
PCR	Polymerase chain reaction
PenStrep	Penicillin Streptavidin
PFA	Paraformaldehyde
pFTAA	pentameric formyl thiophene acetic acid
PS	Presenilin
PSD	postsynaptic density
RIPA	radioimmunoprecipitation assay buffer
RNA	ribonucleic acid
ROI	region of interest
ROS	reactive oxygen species
qRT-PCR	quantitative real time PCR
rpm	rotations per minute
RPMI	Roswell Park Memorial Institute
RT	room temperature
RT-PCR	reverse transcription PCR
RXR	retinoid X receptor
s	second
SDS	sodium dodecyl sulfate
s.d.	standard deviation
Sp1	specific protein 1
TAE	Tris-acetat-EDTA-electrophoresis buffer
TBS	Tris buffered saline
tdRFP	tandem red fluorescent protein
TEMED	tetramethylethylene diamine
TK	thymidine kinase
TLR	Toll-like receptor
Tnfα	Tumor necrosis factor α
Tris	Tris-(Hydroxymethyl)-aminomethane
TX	TBS buffer containing 1 % Triton X-100
US	United States
wt	wildtype
w/v	weight per volume

7.2 Figures and Tables

8 References

1. Eglitis, M.A. and E. Mezey, *Hematopoietic cells differentiate into both microglia and macroglia in the brains of adult mice.* Proc Natl Acad Sci U S A, 1997. **94**(8): p. 4080-5.

2. van Rossum, D. and U.K. Hanisch, *Microglia.* Metab Brain Dis, 2004. **19**(3-4): p. 393-411.

3. Kreutzberg, G.W., *Microglia: a sensor for pathological events in the CNS.* Trends Neurosci, 1996. **19**(8): p. 312-8.

4. Davalos, D., et al., *ATP mediates rapid microglial response to local brain injury in vivo.* Nat Neurosci, 2005. **8**(6): p. 752-8.

5. Nimmerjahn, A., F. Kirchhoff, and F. Helmchen, *Resting microglial cells are highly dynamic surveillants of brain parenchyma in vivo.* Science, 2005. **308**(5726): p. 1314-8.

6. Tremblay, M.E., R.L. Lowery, and A.K. Majewska, *Microglial interactions with synapses are modulated by visual experience.* PLoS Biol, 2010. **8**(11): p. e1000527.

7. Wake, H., et al., *Resting microglia directly monitor the functional state of synapses in vivo and determine the fate of ischemic terminals.* J Neurosci, 2009. **29**(13): p. 3974-80.

8. Marin-Teva, J.L., et al., *Microglia and neuronal cell death.* Neuron Glia Biol, 2011. **7**(1): p. 25-40.

9. Marin-Teva, J.L., et al., *Microglia promote the death of developing Purkinje cells.* Neuron, 2004. **41**(4): p. 535-47.

10. Frade, J.M. and Y.A. Barde, *Microglia-derived nerve growth factor causes cell death in the developing retina.* Neuron, 1998. **20**(1): p. 35-41.

11. Sedel, F., et al., *Macrophage-derived tumor necrosis factor alpha, an early developmental signal for motoneuron death.* J Neurosci, 2004. **24**(9): p. 2236-46.

12. Wakselman, S., et al., *Developmental neuronal death in hippocampus requires the microglial CD11b integrin and DAP12 immunoreceptor.* J Neurosci, 2008. **28**(32): p. 8138-43.

13. Bessis, A., et al., *Microglial control of neuronal death and synaptic properties.* Glia, 2007. **55**(3): p. 233-8.

14. Salter, M.W. and S. Beggs, *Sublime microglia: expanding roles for the guardians of the CNS.* Cell, 2014. **158**(1): p. 15-24.

15. Hanisch, U.K. and H. Kettenmann, *Microglia: active sensor and versatile effector cells in the normal and pathologic brain.* Nat Neurosci, 2007. **10**(11): p. 1387-94.

16. Graeber, M.B. and W.J. Streit, *Microglia: biology and pathology.* Acta Neuropathol, 2010. **119**(1): p. 89-105.

17. McKercher, S.R., et al., *Targeted disruption of the PU.1 gene results in multiple hematopoietic abnormalities.* EMBO J, 1996. **15**(20): p. 5647-58.

18. Beers, D.R., et al., *Wild-type microglia extend survival in PU.1 knockout mice with familial amyotrophic lateral sclerosis.* Proc Natl Acad Sci U S A, 2006. **103**(43): p. 16021-6.

19. Akiyama, H. and P.L. McGeer, *Brain microglia constitutively express beta-2 integrins.* J Neuroimmunol, 1990. **30**(1): p. 81-93.

20. Ginhoux, F., et al., *Fate mapping analysis reveals that adult microglia derive from primitive macrophages.* Science, 2010. **330**(6005): p. 841-5.

21. Schulz, C., et al., *A lineage of myeloid cells independent of Myb and hematopoietic stem cells.* Science, 2012. **336**(6077): p. 86-90.

22. Dalton, M.M., O.R. Hommes, and C.P. Leblond, *Correlation of glial proliferation with age in the mouse brain.* J Comp Neurol, 1968. **134**(4): p. 397-400.

23. Lawson, L.J., V.H. Perry, and S. Gordon, *Turnover of resident microglia in the normal adult mouse brain.* Neuroscience, 1992. **48**(2): p. 405-15.

24. Ajami, B., et al., *Local self-renewal can sustain CNS microglia maintenance and function throughout adult life.* Nat Neurosci, 2007. **10**(12): p. 1538-43.

25. Hefendehl, J.K., et al., *Homeostatic and injury-induced microglia behavior in the aging brain.* Aging Cell, 2014. **13**(1): p. 60-9.

26. Miller, K.R. and W.J. Streit, *The effects of aging, injury and disease on microglial function: a case for cellular senescence.* Neuron Glia Biol, 2007. **3**(3): p. 245-53.

27. Mildner, A., et al., *Distinct and non-redundant roles of microglia and myeloid subsets in mouse models of Alzheimer's disease.* J Neurosci, 2011. **31**(31): p. 11159-71.

28. Mildner, A., et al., *Microglia in the adult brain arise from Ly-6ChiCCR2+ monocytes only under defined host conditions.* Nat Neurosci, 2007. **10**(12): p. 1544-53.

29. Saederup, N., et al., *Selective chemokine receptor usage by central nervous system myeloid cells in CCR2-red fluorescent protein knock-in mice.* PLoS One, 2010. **5**(10): p. e13693.

30. Stalder, A.K., et al., *Invasion of hematopoietic cells into the brain of amyloid precursor protein transgenic mice.* J Neurosci, 2005. **25**(48): p. 11125-32.

31. Querfurth, H.W. and F.M. LaFerla, *Alzheimer's disease.* N Engl J Med. **362**(4): p. 329-44.

32. Alzheimer, A., et al., *An English translation of Alzheimer's 1907 paper, "Uber eine eigenartige Erkankung der Hirnrinde".* Clin Anat, 1995. **8**(6): p. 429-31.

33. Kraepelin, E., *Ein Lehrbuch fuer Studierende und Aerzte*. Psychatrie. Vol. II Band. 1910, Leipzig: Barth Verlag

34. Braak, H., et al., *Neuropathological hallmarks of Alzheimer's and Parkinson's diseases.* Prog Brain Res, 1998. **117**: p. 267-85.

35. DeKosky, S.T. and S.W. Scheff, *Synapse loss in frontal cortex biopsies in Alzheimer's disease: correlation with cognitive severity.* Ann Neurol, 1990. **27**(5): p. 457-64.

36. Scheff, S.W., S.T. DeKosky, and D.A. Price, *Quantitative assessment of cortical synaptic density in Alzheimer's disease.* Neurobiol Aging, 1990. **11**(1): p. 29-37.

37. Iqbal, K., et al., *Tau pathology in Alzheimer disease and other tauopathies.* Biochim Biophys Acta, 2005. **1739**(2-3): p. 198-210.

38. Haass, C., et al., *Amyloid beta-peptide is produced by cultured cells during normal metabolism.* Nature, 1992. **359**(6393): p. 322-5.

39. Seubert, P., et al., *Isolation and quantification of soluble Alzheimer's beta-peptide from biological fluids.* Nature, 1992. **359**(6393): p. 325-7.

40. Shoji, M., et al., *Production of the Alzheimer amyloid beta protein by normal proteolytic processing.* Science, 1992. **258**(5079): p. 126-9.

41. Glenner, G.G. and C.W. Wong, *Alzheimer's disease: initial report of the purification and characterization of a novel cerebrovascular amyloid protein.* Biochem Biophys Res Commun, 1984. **120**(3): p. 885-90.

42. Glenner, G.G. and C.W. Wong, *Alzheimer's disease and Down's syndrome: sharing of a unique cerebrovascular amyloid fibril protein.* Biochem Biophys Res Commun, 1984. **122**(3): p. 1131-5.

43. Iwatsubo, T., et al., *Visualization of A beta 42(43) and A beta 40 in senile plaques with end-specific A beta monoclonals: evidence that an initially deposited species is A beta 42(43).* Neuron, 1994. **13**(1): p. 45-53.

44. Zou, K., et al., *Amyloid beta-protein (Abeta)1-40 protects neurons from damage induced by Abeta1-42 in culture and in rat brain.* J Neurochem, 2003. **87**(3): p. 609-19.

45. Hardy, J. and D.J. Selkoe, *The amyloid hypothesis of Alzheimer's disease: progress and problems on the road to therapeutics.* Science, 2002. **297**(5580): p. 353-6.

46. Hardy, J. and D. Allsop, *Amyloid deposition as the central event in the aetiology of Alzheimer's disease.* Trends Pharmacol Sci, 1991. **12**(10): p. 383-8.

47. Jarrett, J.T., E.P. Berger, and P.T. Lansbury, Jr., *The carboxy terminus of the beta amyloid protein is critical for the seeding of amyloid formation: implications for the pathogenesis of Alzheimer's disease.* Biochemistry, 1993. **32**(18): p. 4693-7.

48. Pike, C.J., et al., *In vitro aging of beta-amyloid protein causes peptide aggregation and neurotoxicity.* Brain Res, 1991. **563**(1-2): p. 311-4.

49. Kayed, R., et al., *Common structure of soluble amyloid oligomers implies common mechanism of pathogenesis.* Science, 2003. **300**(5618): p. 486-9.

50. Castano, E.M., et al., *In vitro formation of amyloid fibrils from two synthetic peptides of different lengths homologous to Alzheimer's disease beta-protein.* Biochem Biophys Res Commun, 1986. **141**(2): p. 782-9.

51. Walsh, D.M. and D.J. Selkoe, *A beta oligomers - a decade of discovery.* J Neurochem, 2007. **101**(5): p. 1172-84.

52. Cai, H., et al., *BACE1 is the major beta-secretase for generation of Abeta peptides by neurons.* Nat Neurosci, 2001. **4**(3): p. 233-4.

53. Vassar, R., et al., *Beta-secretase cleavage of Alzheimer's amyloid precursor protein by the transmembrane aspartic protease BACE.* Science, 1999. **286**(5440): p. 735-41.

54. Schroeter, E.H., et al., *A presenilin dimer at the core of the gamma-secretase enzyme: insights from parallel analysis of Notch 1 and APP proteolysis.* Proc Natl Acad Sci U S A, 2003. **100**(22): p. 13075-80.

55. Thinakaran, G. and E.H. Koo, *Amyloid precursor protein trafficking, processing, and function.* J Biol Chem, 2008. **283**(44): p. 29615-9.

56. Ball, M.J., *Neuronal loss, neurofibrillary tangles and granulovacuolar degeneration in the hippocampus with ageing and dementia. A quantitative study.* Acta Neuropathol, 1977. **37**(2): p. 111-8.

57. Alzheimer's, A., *2014 Alzheimer's disease facts and figures.* Alzheimers Dement, 2014. **10**(2): p. e47-92.

58. Henderson, A.S., et al., *Environmental risk factors for Alzheimer's disease: their relationship to age of onset and to familial or sporadic types.* Psychol Med, 1992. **22**(2): p. 429-36.

59. Corder, E.H., et al., *Gene dose of apolipoprotein E type 4 allele and the risk of Alzheimer's disease in late onset families.* Science, 1993. **261**(5123): p. 921-3.

60. Blennow, K., M.J. de Leon, and H. Zetterberg, *Alzheimer's disease.* Lancet, 2006. **368**(9533): p. 387-403.

61. Masters, C.L., et al., *Amyloid plaque core protein in Alzheimer disease and Down syndrome.* Proc Natl Acad Sci U S A, 1985. **82**(12): p. 4245-9.

62. Goate, A., *Segregation of a missense mutation in the amyloid beta-protein precursor gene with familial Alzheimer's disease.* J Alzheimers Dis, 2006. **9**(3 Suppl): p. 341-7.

63. Sherrington, R., et al., *Cloning of a gene bearing missense mutations in early-onset familial Alzheimer's disease.* Nature, 1995. **375**(6534): p. 754-60.

64. Levy-Lahad, E., et al., *A familial Alzheimer's disease locus on chromosome 1.* Science, 1995. **269**(5226): p. 970-3.

65. Ashe, K.H. and K.R. Zahs, *Probing the biology of Alzheimer's disease in mice.* Neuron, 2010. **66**(5): p. 631-45.

66. Oddo, S., et al., *Triple-transgenic model of Alzheimer's disease with plaques and tangles: intracellular Abeta and synaptic dysfunction.* Neuron, 2003. **39**(3): p. 409-21.

67. McKhann, G., et al., *Clinical diagnosis of Alzheimer's disease: report of the NINCDS-ADRDA Work Group under the auspices of Department of Health and Human Services Task Force on Alzheimer's Disease.* Neurology, 1984. **34**(7): p. 939-44.

68. Tarawneh, R. and D.M. Holtzman, *The clinical problem of symptomatic Alzheimer disease and mild cognitive impairment.* Cold Spring Harb Perspect Med, 2012. **2**(5): p. a006148.

69. Folstein, M.F., S.E. Folstein, and P.R. McHugh, *"Mini-mental state". A practical method for grading the cognitive state of patients for the clinician.* J Psychiatr Res, 1975. **12**(3): p. 189-98.

70. Brodaty, H. and C.M. Moore, *The Clock Drawing Test for dementia of the Alzheimer's type: A comparison of three scoring methods in a memory disorders clinic.* Int J Geriatr Psychiatry, 1997. **12**(6): p. 619-27.

71. Jack, C.R., Jr., et al., *Introduction to the recommendations from the National Institute on Aging-Alzheimer's Association workgroups on diagnostic guidelines for Alzheimer's disease.* Alzheimers Dement, 2011. **7**(3): p. 257-62.

72. Kumar, A., A. Singh, and Ekavali, *A review on Alzheimer's disease pathophysiology and its management: an update.* Pharmacol Rep, 2015. **67**(2): p. 195-203.

73. Jack, C.R., Jr., et al., *Tracking pathophysiological processes in Alzheimer's disease: an updated hypothetical model of dynamic biomarkers.* Lancet Neurol, 2013. **12**(2): p. 207-16.

74. Heneka, M.T., et al., *Neuroinflammation in Alzheimer's disease.* Lancet Neurol, 2015. **14**(4): p. 388-405.

75. Frank, S., et al., *TREM2 is upregulated in amyloid plaque-associated microglia in aged APP23 transgenic mice.* Glia, 2008. **56**(13): p. 1438-47.

76. Guerreiro, R., et al., *TREM2 variants in Alzheimer's disease.* N Engl J Med, 2013. **368**(2): p. 117-27.

77. Hsieh, C.L., et al., *A role for TREM2 ligands in the phagocytosis of apoptotic neuronal cells by microglia.* J Neurochem, 2009. **109**(4): p. 1144-56.

78. Hickman, S.E., et al., *The microglial sensome revealed by direct RNA sequencing.* Nat Neurosci, 2013. **16**(12): p. 1896-905.

79. Bradshaw, E.M., et al., *CD33 Alzheimer's disease locus: altered monocyte function and amyloid biology.* Nat Neurosci, 2013. **16**(7): p. 848-50.

80. Griciuc, A., et al., *Alzheimer's disease risk gene CD33 inhibits microglial uptake of amyloid beta.* Neuron, 2013. **78**(4): p. 631-43.

81. Itagaki, S., et al., *Relationship of microglia and astrocytes to amyloid deposits of Alzheimer disease.* J Neuroimmunol, 1989. **24**(3): p. 173-82.

82. Terry, R.D., N.K. Gonatas, and M. Weiss, *Ultrastructural Studies in Alzheimer's Presenile Dementia.* Am J Pathol, 1964. **44**: p. 269-97.

83. Wisniewski, H.M., et al., *Ultrastructural studies of the cells forming amyloid fibers in classical plaques.* Can J Neurol Sci, 1989. **16**(4 Suppl): p. 535-42.

84. Fiala, M. and R. Veerhuis, *Biomarkers of inflammation and amyloid-beta phagocytosis in patients at risk of Alzheimer disease.* Exp Gerontol, 2010. **45**(1): p. 57-63.

85. Griffin, W.S., et al., *Brain interleukin 1 and S-100 immunoreactivity are elevated in Down syndrome and Alzheimer disease.* Proc Natl Acad Sci U S A, 1989. **86**(19): p. 7611-5.

86. McGeer, P.L., et al., *Activation of the classical complement pathway in brain tissue of Alzheimer patients.* Neurosci Lett, 1989. **107**(1-3): p. 341-6.

87. Vom Berg, J., et al., *Inhibition of IL-12/IL-23 signaling reduces Alzheimer's disease-like pathology and cognitive decline.* Nat Med, 2012. **18**(12): p. 1812-9.

88. Fillit, H., et al., *Elevated circulating tumor necrosis factor levels in Alzheimer's disease.* Neurosci Lett, 1991. **129**(2): p. 318-20.

89. Patel, N.S., et al., *Inflammatory cytokine levels correlate with amyloid load in transgenic mouse models of Alzheimer's disease.* J Neuroinflammation, 2005. **2**(1): p. 9.

90. Bamberger, M.E., et al., *A cell surface receptor complex for fibrillar beta-amyloid mediates microglial activation.* J Neurosci, 2003. **23**(7): p. 2665-74.

91. Paresce, D.M., R.N. Ghosh, and F.R. Maxfield, *Microglial cells internalize aggregates of the Alzheimer's disease amyloid beta-protein via a scavenger receptor.* Neuron, 1996. **17**(3): p. 553-65.

92. Stewart, C.R., et al., *CD36 ligands promote sterile inflammation through assembly of a Toll-like receptor 4 and 6 heterodimer.* Nat Immunol, 2010. **11**(2): p. 155-61.

93. Liu, Y., et al., *LPS receptor (CD14): a receptor for phagocytosis of Alzheimer's amyloid peptide.* Brain, 2005. **128**(Pt 8): p. 1778-89.

94. Hyman, B.T., K. Marzloff, and P.V. Arriagada, *The lack of accumulation of senile plaques or amyloid burden in Alzheimer's disease suggests a dynamic balance between amyloid deposition and resolution.* J Neuropathol Exp Neurol, 1993. **52**(6): p. 594-600.

95. McGeer, P.L. and E.G. McGeer, *Mechanisms of cell death in Alzheimer disease--immunopathology.* J Neural Transm Suppl, 1998. **54**: p. 159-66.

96. Rogers, J., et al., *Inflammation and Alzheimer's disease pathogenesis.* Neurobiol Aging, 1996. **17**(5): p. 681-6.

97. Akiyama, H., et al., *Inflammation and Alzheimer's disease.* Neurobiol Aging, 2000. **21**(3): p. 383-421.

98. Prokop, S., K.R. Miller, and F.L. Heppner, *Microglia actions in Alzheimer's disease.* Acta Neuropathol, 2013.

99. Heppner, F.L., R.M. Ransohoff, and B. Becher, *Immune attack: the role of inflammation in Alzheimer disease.* Nat Rev Neurosci, 2015. **16**(6): p. 358-72.

100. Njie, E.G., et al., *Ex vivo cultures of microglia from young and aged rodent brain reveal age-related changes in microglial function.* Neurobiol Aging, 2012. **33**(1): p. 195 e1-12.

101. Damani, M.R., et al., *Age-related alterations in the dynamic behavior of microglia.* Aging Cell, 2011. **10**(2): p. 263-76.

102. Krabbe, G., et al., *Functional impairment of microglia coincides with Beta-amyloid deposition in mice with Alzheimer-like pathology.* PLoS One, 2013. **8**(4): p. e60921.

103. Streit, W.J., et al., *Dystrophic microglia in the aging human brain.* Glia, 2004. **45**(2): p. 208-12.

104. Grathwohl, S.A., et al., *Formation and maintenance of Alzheimer's disease beta-amyloid plaques in the absence of microglia.* Nat Neurosci, 2009. **12**(11): p. 1361-3.

105. Kim, J.Y., et al., *Soluble intracellular adhesion molecule-1 secreted by human umbilical cord blood-derived mesenchymal stem cell reduces amyloid-beta plaques.* Cell Death Differ, 2012. **19**(4): p. 680-91.

106. Nikolic, W.V., et al., *Peripherally administered human umbilical cord blood cells reduce parenchymal and vascular beta-amyloid deposits in Alzheimer mice.* Stem Cells Dev, 2008. **17**(3): p. 423-39.

107. Lee, J.K., et al., *Intracerebral transplantation of bone marrow-derived mesenchymal stem cells reduces amyloid-beta deposition and rescues memory deficits in Alzheimer's disease mice by modulation of immune responses.* Stem Cells, 2010. **28**(2): p. 329-43.

108. Ma, T., et al., *Intracerebral transplantation of adipose-derived mesenchymal stem cells alternatively activates microglia and ameliorates neuropathological deficits in Alzheimer's disease mice.* Cell Transplant, 2013. **22 Suppl 1**: p. S113-26.

109. Simard, A.R., et al., *Bone marrow-derived microglia play a critical role in restricting senile plaque formation in Alzheimer's disease.* Neuron, 2006. **49**(4): p. 489-502.

110. Avagyan, S., et al., *A quantitative trait locus on chromosome 4 affects cycling of hematopoietic stem and progenitor cells through regulation of TGF-beta 2 responsiveness.* J Immunol, 2008. **181**(9): p. 5904-11.

111. Hohsfield, L.A. and C. Humpel, *Intravenous infusion of monocytes isolated from 2-week-old mice enhances clearance of Beta-amyloid plaques in an Alzheimer mouse model.* PLoS One, 2015. **10**(4): p. e0121930.

112. El Khoury, J., et al., *Ccr2 deficiency impairs microglial accumulation and accelerates progression of Alzheimer-like disease.* Nat Med, 2007. **13**(4): p. 432-8.

113. Naert, G. and S. Rivest, *CC chemokine receptor 2 deficiency aggravates cognitive impairments and amyloid pathology in a transgenic mouse model of Alzheimer's disease.* J Neurosci, 2011. **31**(16): p. 6208-20.

114. DiCarlo, G., et al., *Intrahippocampal LPS injections reduce Abeta load in APP+PS1 transgenic mice.* Neurobiol Aging, 2001. **22**(6): p. 1007-12.

115. Michaud, J.P., et al., *Toll-like receptor 4 stimulation with the detoxified ligand monophosphoryl lipid A improves Alzheimer's disease-related pathology.* Proc Natl Acad Sci U S A, 2013. **110**(5): p. 1941-6.

116. Boissonneault, V., et al., *Powerful beneficial effects of macrophage colony-stimulating factor on beta-amyloid deposition and cognitive impairment in Alzheimer's disease.* Brain, 2009. **132**(Pt 4): p. 1078-92.

117. Mitrasinovic, O.M. and G.M. Murphy, Jr., *Microglial overexpression of the M-CSF receptor augments phagocytosis of opsonized Abeta.* Neurobiol Aging, 2003. **24**(6): p. 807-15.

118. Lucin, K.M., et al., *Microglial beclin 1 regulates retromer trafficking and phagocytosis and is impaired in Alzheimer's disease.* Neuron, 2013. **79**(5): p. 873-86.

119. Fuhrmann, M., et al., *Microglial Cx3cr1 knockout prevents neuron loss in a mouse model of Alzheimer's disease.* Nat Neurosci, 2010. **13**(4): p. 411-3.

120. Nash, K.R., et al., *Fractalkine overexpression suppresses tau pathology in a mouse model of tauopathy.* Neurobiol Aging, 2013. **34**(6): p. 1540-8.

121. Lee, S., et al., *CX3CR1 deficiency alters microglial activation and reduces beta-amyloid deposition in two Alzheimer's disease mouse models.* Am J Pathol, 2010. **177**(5): p. 2549-62.

122. Cramer, P.E., et al., *ApoE-directed therapeutics rapidly clear beta-amyloid and reverse deficits in AD mouse models.* Science, 2012. **335**(6075): p. 1503-6.

123. Yamanaka, M., et al., *PPARgamma/RXRalpha-induced and CD36-mediated microglial amyloid-beta phagocytosis results in cognitive improvement in amyloid precursor protein/presenilin 1 mice.* J Neurosci, 2012. **32**(48): p. 17321-31.

124. Jin, P., et al., *Anti-inflammatory and anti-amyloidogenic effects of a small molecule, 2,4-bis(p-hydroxyphenyl)-2-butenal in Tg2576 Alzheimer's disease mice model.* J Neuroinflammation, 2013. **10**: p. 2.

125. Chakrabarty, P., et al., *IL-10 alters immunoproteostasis in APP mice, increasing plaque burden and worsening cognitive behavior.* Neuron, 2015. **85**(3): p. 519-33.

126. Guillot-Sestier, M.V., et al., *Il10 deficiency rebalances innate immunity to mitigate Alzheimer-like pathology.* Neuron, 2015. **85**(3): p. 534-48.

127. Heneka, M.T., et al., *NLRP3 is activated in Alzheimer's disease and contributes to pathology in APP/PS1 mice.* Nature, 2013. **493**(7434): p. 674-8.

128. Walsh, J.G., D.A. Muruve, and C. Power, *Inflammasomes in the CNS.* Nat Rev Neurosci, 2014. **15**(2): p. 84-97.

129. Halle, A., et al., *The NALP3 inflammasome is involved in the innate immune response to amyloid-beta.* Nat Immunol, 2008. **9**(8): p. 857-65.

130. Heppner, F.L., et al., *Experimental autoimmune encephalomyelitis repressed by microglial paralysis.* Nat Med, 2005. **11**(2): p. 146-52.

131. Oliver, S., G. Bubley, and C. Crumpacker, *Inhibition of HSV-transformed murine cells by nucleoside analogs, 2'-NDG and 2'-nor-cGMP: mechanisms of inhibition and reversal by exogenous nucleosides.* Virology, 1985. **145**(1): p. 84-93.

132. Dziennis, S., et al., *The CD11b promoter directs high-level expression of reporter genes in macrophages in transgenic mice.* Blood, 1995. **85**(2): p. 319-29.

133. Geissmann, F., et al., *Blood monocytes: distinct subsets, how they relate to dendritic cells, and their possible roles in the regulation of T-cell responses.* Immunol Cell Biol, 2008. **86**(5): p. 398-408.

134. Ard, M.D., et al., *Scavenging of Alzheimer's amyloid beta-protein by microglia in culture.* J Neurosci Res, 1996. **43**(2): p. 190-202.

135. Bard, F., et al., *Peripherally administered antibodies against amyloid beta-peptide enter the central nervous system and reduce pathology in a mouse model of Alzheimer disease.* Nat Med, 2000. **6**(8): p. 916-9.

136. Radde, R., et al., *Abeta42-driven cerebral amyloidosis in transgenic mice reveals early and robust pathology.* EMBO Rep, 2006. **7**(9): p. 940-6.

137. Jung, S., et al., *Analysis of fractalkine receptor CX(3)CR1 function by targeted deletion and green fluorescent protein reporter gene insertion.* Mol Cell Biol, 2000. **20**(11): p. 4106-14.

138. Luche, H., et al., *Faithful activation of an extra-bright red fluorescent protein in "knock-in" Cre-reporter mice ideally suited for lineage tracing studies.* Eur J Immunol, 2007. **37**(1): p. 43-53.

139. Hefendehl, J.K., et al., *Repeatable target localization for long-term in vivo imaging of mice with 2-photon microscopy.* J Neurosci Methods, 2012. **205**(2): p. 357-63.

140. Hefendehl, J.K., et al., *Long-term in vivo imaging of beta-amyloid plaque appearance and growth in a mouse model of cerebral beta-amyloidosis.* J Neurosci, 2011. **31**(2): p. 624-9.

141. Klunk, W.E., et al., *Imaging Abeta plaques in living transgenic mice with multiphoton microscopy and methoxy-X04, a systemically administered Congo red derivative.* J Neuropathol Exp Neurol, 2002. **61**(9): p. 797-805.

142. Parslow, A., A. Cardona, and R.J. Bryson-Richardson, *Sample drift correction following 4D confocal time-lapse imaging.* J Vis Exp, 2014(86).

143. Berg, I., et al., *Efficient imaging of amyloid deposits in Drosophila models of human amyloidoses.* Nat Protoc, 2010. **5**(5): p. 935-44.

144. Long, J.M., et al., *Stereological estimation of total microglia number in mouse hippocampus.* J Neurosci Methods, 1998. **84**(1-2): p. 101-8.

145. Schefe, J.H., et al., *Quantitative real-time RT-PCR data analysis: current concepts and the novel "gene expression's CT difference" formula.* J Mol Med (Berl), 2006. **84**(11): p. 901-10.

146. Kawarabayashi, T., et al., *Age-dependent changes in brain, CSF, and plasma amyloid (beta) protein in the Tg2576 transgenic mouse model of Alzheimer's disease.* J Neurosci, 2001. **21**(2): p. 372-81.

147. Mariathasan, S., et al., *Cryopyrin activates the inflammasome in response to toxins and ATP.* Nature, 2006. **440**(7081): p. 228-32.

148. Holtmaat, A., et al., *Long-term, high-resolution imaging in the mouse neocortex through a chronic cranial window.* Nat Protoc, 2009. **4**(8): p. 1128-44.

149. Xu, H.T., et al., *Choice of cranial window type for in vivo imaging affects dendritic spine turnover in the cortex.* Nat Neurosci, 2007. **10**(5): p. 549-51.

150. Yan, P., et al., *Characterizing the appearance and growth of amyloid plaques in APP/PS1 mice.* J Neurosci, 2009. **29**(34): p. 10706-14.

151. Singh, N., et al., *A safe lithium mimetic for bipolar disorder.* Nat Commun, 2013. **4**: p. 1332.

152. Galvao, J., et al., *Unexpected low-dose toxicity of the universal solvent DMSO.* FASEB J, 2014. **28**(3): p. 1317-30.

153. Gould, S. and R.C. Scott, *2-Hydroxypropyl-beta-cyclodextrin (HP-beta-CD): a toxicology review.* Food Chem Toxicol, 2005. **43**(10): p. 1451-9.

154. Bachmanov, A.A., et al., *Food intake, water intake, and drinking spout side preference of 28 mouse strains.* Behav Genet, 2002. **32**(6): p. 435-43.

155. Varvel, N.H., et al., *Microglial repopulation model reveals a robust homeostatic process for replacing CNS myeloid cells.* Proc Natl Acad Sci U S A, 2012. **109**(44): p. 18150-5.

156. Bolmont, T., et al., *Dynamics of the microglial/amyloid interaction indicate a role in plaque maintenance.* J Neurosci, 2008. **28**(16): p. 4283-92.

157. Meyer-Luehmann, M., et al., *Rapid appearance and local toxicity of amyloid-beta plaques in a mouse model of Alzheimer's disease.* Nature, 2008. **451**(7179): p. 720-4.

158. Vallieres, L. and P.E. Sawchenko, *Bone marrow-derived cells that populate the adult mouse brain preserve their hematopoietic identity.* J Neurosci, 2003. **23**(12): p. 5197-207.

159. Ajami, B., et al., *Infiltrating monocytes trigger EAE progression, but do not contribute to the resident microglia pool.* Nat Neurosci, 2011. **14**(9): p. 1142-9.

160. Elmore, M.R., et al., *Colony-stimulating factor 1 receptor signaling is necessary for microglia viability, unmasking a microglia progenitor cell in the adult brain.* Neuron, 2014. **82**(2): p. 380-97.

161. Kozlowski, C. and R.M. Weimer, *An automated method to quantify microglia morphology and application to monitor activation state longitudinally in vivo.* PLoS One, 2012. **7**(2): p. e31814.

162. Glenn, J.A., et al., *Characterisation of ramified microglial cells: detailed morphology, morphological plasticity and proliferative capability.* J Anat, 1992. **180 (Pt 1)**: p. 109-18.

163. Elmore, M.R., et al., *Characterizing newly repopulated microglia in the adult mouse: impacts on animal behavior, cell morphology, and neuroinflammation.* PLoS One, 2015. **10**(4): p. e0122912.

164. Ding, Z., et al., *Antiviral drug ganciclovir is a potent inhibitor of microglial proliferation and neuroinflammation.* J Exp Med, 2014. **211**(2): p. 189-98.

165. van de Haar, H.J., et al., *Blood-brain barrier impairment in dementia: current and future in vivo assessments.* Neurosci Biobehav Rev, 2015. **49**: p. 71-81.

166. Ruggieri, P.A., *C-reactive blood protein in inflammatory disease; its value as an index of rheumatic activity.* J Med Soc N J, 1955. **52**(10): p. 500-4.

167. Guerin, P.J. and E.R. Gauthier, *Induction of cellular necrosis by the glutathione peroxidase mimetic ebselen.* J Cell Biochem, 2003. **89**(1): p. 203-11.

168. Yang, C.F., H.M. Shen, and C.N. Ong, *Ebselen induces apoptosis in HepG(2) cells through rapid depletion of intracellular thiols.* Arch Biochem Biophys, 2000. **374**(2): p. 142-52.

169. Sudduth, T.L., A. Greenstein, and D.M. Wilcock, *Intracranial injection of Gammagard, a human IVIg, modulates the inflammatory response of the brain and lowers Abeta in APP/PS1 mice along a different time course than anti-Abeta antibodies.* J Neurosci, 2013. **33**(23): p. 9684-92.

170. McGeer, P.L., M. Schulzer, and E.G. McGeer, *Arthritis and anti-inflammatory agents as possible protective factors for Alzheimer's disease: a review of 17 epidemiologic studies.* Neurology, 1996. **47**(2): p. 425-32.

171. Dragicevic, N., et al., *Green tea epigallocatechin-3-gallate (EGCG) and other flavonoids reduce Alzheimer's amyloid-induced mitochondrial dysfunction.* J Alzheimers Dis, 2011. **26**(3): p. 507-21.

172. Lim, G.P., et al., *Ibuprofen suppresses plaque pathology and inflammation in a mouse model for Alzheimer's disease.* J Neurosci, 2000. **20**(15): p. 5709-14.

173. Yan, Q., et al., *Anti-inflammatory drug therapy alters beta-amyloid processing and deposition in an animal model of Alzheimer's disease.* J Neurosci, 2003. **23**(20): p. 7504-9.

174. Larabee, J.L., J.R. Hocker, and J.S. Hanas, *Mechanisms of inhibition of zinc-finger transcription factors by selenium compounds ebselen and selenite.* J Inorg Biochem, 2009. **103**(3): p. 419-26.

175. Citron, B.A., et al., *Transcription factor Sp1 dysregulation in Alzheimer's disease.* J Neurosci Res, 2008. **86**(11): p. 2499-504.

176. Granic, I., et al., *Inflammation and NF-kappaB in Alzheimer's disease and diabetes.* J Alzheimers Dis, 2009. **16**(4): p. 809-21.

177. Spires, T.L., et al., *Dendritic spine abnormalities in amyloid precursor protein transgenic mice demonstrated by gene transfer and intravital multiphoton microscopy.* J Neurosci, 2005. **25**(31): p. 7278-87.

178. Schwab, C., et al., *GAD65, GAD67, and GABAT immunostaining in human brain and apparent GAD65 loss in Alzheimer's disease.* J Alzheimers Dis, 2013. **33**(4): p. 1073-88.

179. Chew, P., et al., *Site-specific antiatherogenic effect of the antioxidant ebselen in the diabetic apolipoprotein E-deficient mouse.* Arterioscler Thromb Vasc Biol, 2009. **29**(6): p. 823-30.

180. Gealekman, O., et al., *Endothelial dysfunction as a modifier of angiogenic response in Zucker diabetic fat rat: amelioration with Ebselen.* Kidney Int, 2004. **66**(6): p. 2337-47.

181. Tan, S.M., et al., *The modified selenenyl amide, M-hydroxy ebselen, attenuates diabetic nephropathy and diabetes-associated atherosclerosis in ApoE/GPx1 double knockout mice.* PLoS One, 2013. **8**(7): p. e69193.

182. Yamaguchi, T., et al., *Ebselen in acute ischemic stroke: a placebo-controlled, double-blind clinical trial. Ebselen Study Group.* Stroke, 1998. **29**(1): p. 12-7.

183. Saito, I., et al., *Neuroprotective effect of an antioxidant, ebselen, in patients with delayed neurological deficits after aneurysmal subarachnoid hemorrhage.* Neurosurgery, 1998. **42**(2): p. 269-77; discussion 277-8.

184. Zerbinatti, C.V., et al., *Increased soluble amyloid-beta peptide and memory deficits in amyloid model mice overexpressing the low-density lipoprotein receptor-related protein.* Proc Natl Acad Sci U S A, 2004. **101**(4): p. 1075-80.

185. Koffie, R.M., et al., *Oligomeric amyloid beta associates with postsynaptic densities and correlates with excitatory synapse loss near senile plaques.* Proc Natl Acad Sci U S A, 2009. **106**(10): p. 4012-7.

186. Tseng, B.P., et al., *Deposition of monomeric, not oligomeric, Abeta mediates growth of Alzheimer's disease amyloid plaques in human brain preparations.* Biochemistry, 1999. **38**(32): p. 10424-31.

187. Esler, W.P., et al., *Deposition of soluble amyloid-beta onto amyloid templates: with application for the identification of amyloid fibril extension inhibitors.* Methods Enzymol, 1999. **309**: p. 350-74.

188. Parkhurst, C.N., et al., *Microglia promote learning-dependent synapse formation through brain-derived neurotrophic factor.* Cell, 2013. **155**(7): p. 1596-609.

189. Bruttger, J., et al., *Genetic Cell Ablation Reveals Clusters of Local Self-Renewing Microglia in the Mammalian Central Nervous System.* Immunity, 2015.

190. Coll, R.C., et al., *A small-molecule inhibitor of the NLRP3 inflammasome for the treatment of inflammatory diseases.* Nat Med, 2015. **21**(3): p. 248-55.

191. Youm, Y.H., et al., *Elimination of the NLRP3-ASC inflammasome protects against chronic obesity-induced pancreatic damage.* Endocrinology, 2011. **152**(11): p. 4039-45.

9 Eidesstattliche Versicherung

„Ich, Natalia Drost, versichere an Eides statt durch meine eigenhändige Unterschrift, dass ich die vorgelegte Dissertation mit dem Thema: „Characterization and manipulation of myeloid cells in the healthy and diseased Central Nervous System“ selbstständig und ohne nicht offengelegte Hilfe Dritter verfasst und keine anderen als die angegebenen Quellen und Hilfsmittel genutzt habe.
Alle Stellen, die wörtlich oder dem Sinne nach auf Publikationen oder Vorträgen anderer Autoren beruhen, sind als solche in korrekter Zitierung (siehe „Uniform Requirements for Manuscripts (URM)“ des ICMJE -*www.**icmje**.org*) kenntlich gemacht. Die Abschnitte zu Methodik (insbesondere praktische Arbeiten, Laborbestimmungen, statistische Aufarbeitung) und Resultaten (insbesondere Abbildungen, Graphiken und Tabellen) entsprechen den URM (s.o) und werden von mir verantwortet.
Meine Anteile an etwaigen Publikationen zu dieser Dissertation entsprechen denen, die in der untenstehenden gemeinsamen Erklärung mit dem/der Betreuer/in, angegeben sind. Sämtliche Publikationen, die aus dieser Dissertation hervorgegangen sind und bei denen ich Autor bin, entsprechen den URM (s.o) und werden von mir verantwortet.

Die Bedeutung dieser eidesstattlichen Versicherung und die strafrechtlichen Folgen einer unwahren eidesstattlichen Versicherung (§156,161 des Strafgesetzbuches) sind mir bekannt und bewusst.“

Datum Unterschrift

10 Anteilserklärung an etwaigen erfolgten Publikationen

Natalia Drost hatte folgenden Anteil an den folgenden Publikationen:

S Prokop*, KR Miller*, **N Drost**, V Mathur , J Luo , A Wegner , T Wyss-Coray, FL Heppner: *Impact of peripheral myeloid cells on β-amyloid pathology in Alzheimer's disease-like mice*. *These authors contributed equally to this work. J Exp Med, in press.
Beitrag im Einzelnen (bitte kurz ausführen): Natalia Drost hat stereologische Analysen von Gewebeschnitten durchgeführt.

KR Miller*, S Prokop*, **N Drost**, V Mathur, J Luo, M Greter, F Mair, JSH von Bueren, S Kraft, RE Kälin, B Becher, T Wyss-Coray and FL Heppner: *Molecular signature and fate of bone marrow-derived myeloid cells repopulating the adult CNS upon ablation of resident microglia*. *These authors contributed equally to this work. Manuscript in preparation.
Beitrag im Einzelnen (bitte kurz ausführen): Natalia Drost hat einen Teil der veröffentlichten Experiment Daten ausgeführt und ausgewertet.

N Drost, S Prokop, KR Miller, Z Cseresnyes, JL Rinnenthal, FL Heppner: *Morphology and dynamics of bone marrow-derived myeloid cells repopulating the Alzheimer diseased brain upon ablation of resident microglia – a long-term multiphoton in vivo comparison*. Manuscript in preparation.
Beitrag im Einzelnen (bitte kurz ausführen): Natalia Drost hat die Experimente geplant, ausgeführt, ausgewertet, sowie das Manuskript geschrieben.

11 Curriculum Vitae

"Mein Lebenslauf wird aus datenschutzrechtlichen Gründen in der elektronischen Version meiner Arbeit nicht veröffentlicht."

"Mein Lebenslauf wird aus datenschutzrechtlichen Gründen in der elektronischen Version meiner Arbeit nicht veröffentlicht."

"Mein Lebenslauf wird aus datenschutzrechtlichen Gründen in der elektronischen Version meiner Arbeit nicht veröffentlicht."

12 Publications

N Drost, S Prokop, KR Miller, Z Cseresnyes, JL Rinnenthal, FL Heppner: *Morphology and dynamics of bone marrow-derived myeloid cells repopulating the Alzheimer diseased brain upon ablation of resident microglia – a long-term multiphoton in vivo comparison*. Manuscript in preparation.

KR Miller*, S Prokop*, **N Drost**, V Mathur, JL, M Greter, F Mair, JSH von Bueren, S Kraft, RE Kälin, B Becher, T Wyss-Coray and FL Heppner: *Molecular signature and fate of bone marrow-derived myeloid cells repopulating the adult CNS upon ablation of resident microglia*. *These authors contributed equally to this work. Manuscript in preparation.

S Prokop*, KR Miller*, **N Drost**, V Mathur , J Luo , A Wegner , T Wyss-Coray, FL Heppner: *Impact of peripheral myeloid cells on β-amyloid pathology in Alzheimer's disease-like mice*. *These authors contributed equally to this work. J Exp Med, in press.

A Paliwala, AM Temkin, K Kerkel, A Yale, I Yotova, **N Drost**, S Lax, CL Nhan-Chang, C Powell, A Borchzuk, A Aviv, R Wapner, X Chen, P Nagy, N Schork, C Do, A Torkamani, B Tycko: *Comparative anatomy of chromosomal domains with imprinted and nonimprinted allele-specific DNA methylation.* PLoS Genet., 2013 Aug 29; 9(8): e1003622.

SW Weyer, M Klevanski, A Delekate, V Voikar, D Aydin, M Hick, M Filippov, **N Drost**, KL Schaller, M Saar, MA Vogt, P Gass, A Samanta, A Jäschke, M Korte, DP Wolfer, JH Caldwell, UC Müller: *APP and APLP2 are essential at PNS and CNS synapses for transmission, spatial learning and LTP.* EMBO J, EMBO J, 2011 Jun 1; 30(11):2266-80.

E Letellier, S Kumar, I Sancho-Martinez, S Krauth, A Funke-Kaiser, S Laudenklos, K Konecki, S Klussmann, NS Corsini, S Kleber, **N Drost**, A Neumann, M Le´vi-Strauss, B Brors, N Gretz, L Edler, C Fischer, O Hill, M Thiemann, B Biglari, S Karray, A Martin-Villalba: *CD95-Ligand on Peripheral Myeloid Cells Activates Syk Kinase to Trigger Their Recruitment to the Inflammatory Site*. Immunity, 2010 Feb 26; 32(2):240-52.

13 Danksagung

Zuerst möchte ich mich bei Prof. Dr. Frank Heppner bedanken, welche mir die Möglichkeit und Mittel zur Verfügung gestellt hat diese Doktorarbeit anzufertigen. Ich habe sehr gern an dem Thema und in Ihrer Gruppe gearbeitet. Und danke für die sehr ausführlichen Korrekturen!

Besonderer Dank geht auch an Stefan Prokop für die tolle Betreuung meiner Arbeit, den wissenschaftlichen Input und die Unterstützung. Vielen Dank auch für die Korrektur dieser Arbeit! Auch Kelly Miller möchte ich herzlich für Unterstützung und wissenschaftlichen Input danken.

Zudem möchte ich Raluca Niesner, Robert Kötter und Zoltan Cseresnyes für eine sehr angenehme Arbeits-Atmosphäre am 2P-Mikroskop-Standort danken. Ohne eure technische Unterstützung wäre vieles nicht möglich gewesen. Danke Zoltan für das Programmieren der Distanzanalyse.

Auch meiner Arbeitsgruppe möchte ich herzlich danken. Allen beteiligten technischen Assistenten und auch Post-Doc‘s für ihre Hilfe und offenes Ohr bei Fragen und Problemen. Und Juliane, Lisa, Caroline, Claudia, Maren, Pascale und Judith für spaßige Zeiten auch außerhalb der Arbeit, danke für die gute Zeit und jeglichen emotionalen Unterstützungen.

Herzlichen Dank auch an meinen Vinni der die schweren Phasen aufgeheitert hat und mein Leben einfach schöner macht. Danke, dass du mich daran erinnerst, dass Arbeit nicht alles ist!

Und der wichtigste Dank geht an meine Eltern Bozena und Gregor, sowie meine Stiefeltern Danuta und Torsten und meine Großeltern Helga und Marian – danke für Euer offenes Ohr, das ihr immer an mich glaubt und mich in jeglichen Lebenslagen unterstützt!